PH.D. THESIS

Stability of domain walls with biased initial conditions and their signatures in the CMB cosmic birefringence

---

偏った初期条件を持つドメインウォールの安定性とその宇宙複屈折における特徴

Author:
Diego GONZALEZ

Supervisor:
Dr. Fuminobu TAKAHASHI

Particle Theory and Cosmology Group
Department of Physics, Tohoku University

令和 5 年 (2023)

TOHOKU UNIVERSITY

Abstract

Graduate School of Science and Faculty of Science

Department of Physics

Doctor of Philosophy

Stability of domain walls with biased initial conditions and their signatures in the CMB cosmic birefringence

by Diego GONZALEZ

Topological defects are stable structures generated after a symmetry is spontaneously broken. Domain walls are surface-like defects with important cosmological consequences, namely they dominate the energy contents of the universe for a large sector of the parameter space. Their generation in our universe is well motivated by beyond the standard model theories such as axions or string theory. When the initial conditions generated during inflation are properly taken into account, the dynamics of the domain wall networks are different to what had been studied previously in the literature. Most notably, they are incredibly resilient to initial condition biases, which had been thought as one of the main ways to induce domain wall decay and thus avoid wall domination. A subdominant, stable domain wall network could induce an isotropic rotation of the CMB light—cosmic birefringence—in line with the currently observed value, and predicts anisotropic cosmic birefringence within the reach of next-generation CMB polarization probes.

Contents

Chapter 1

Introduction

Symmetries are at the core of our modern understanding of physics and cosmology. Spontaneous symmetry breaking (SSB) is the phenomenon in which a stable state of a system transforms nontrivially under some symmetries of the theory. That is, those symmetries are present on the equations of motion (how that state behaves) but not on the state itself. This concept originated from the study of condensed matter physics and was later introduced into particle physics and cosmology.

Topological defects are stable states with non-minimal energy which can occur in theories with spontaneously broken symmetries. Let us consider one of those spiral telephone cords that landline or home phones used to have. Those cords are coiled in just one direction (e.g. clockwise) but with continued use they tend to tangle, at one point switching from coiling clockwise to counterclockwise. That is a topological defect! The state has nonzero energy since the cord is overstretched, and it is stable since in order to remove it we have to manually fix how it coils along most of the cable length. This is different from just stretching the cord, which is a state with nonzero energy but which returns to the minimum energy state the moment whatever is holding the cord is removed. The existence and stability of defects are given by the topology of the vacuum itself. In our example, by the fact that the cord can coil either clockwise or counterclockwise. All physics students have heard at some point of magnetic monopoles, but there are other types as well. Topological defects are classified depending on their dimensionality in monopoles (0D), strings (1D), domain walls (2D) and textures (3D).

Let us consider a scalar field whose potential has multiple minima of the same energy. Then we can consider a state in which in some regions the field takes one minimum while in others, a different one. The field must interpolate between both, thus generating a region of nonzero energy called **domain wall**. In 3D space, domain walls are surface-like structures with a finite thickness to them. If we consider many of those patches with equal choices of potential minima, then we obtain a domain wall network.

Spontaneously broken symmetries tend to be restored at high energies. If that is the case, then as the universe expands and cools down, there will be a point in time at which the symmetry becomes spontaneously broken again. If a phase transition like this happens in our universe, it may lead to the generation of topological defects. That can be a problem, as we have not observed any topological defect in our universe yet. Domain walls are of particular interest—or worry—to cosmologists.

Unless their tension, which is related to the mass of the underlying scalar field, is incredibly small, domain wall networks quickly dominate the energy contents of the universe, making the universe expansion anisotropic. That would definitely be problem, as it is far from what we observe today. Axions are light pseudoscalar particles which could take many roles in particle physics and cosmology, such as constituting part or all of dark matter, solving naturalness problems, or driving inflation. Axion theories are beyond the standard model, but well motivated, and they lead to domain wall network formation at some point in the early universe.

The current cosmological paradigm is the standard big bang model. The current universe is then understood via the ΛCDM model, which combines a cosmological term with the structure formation by cold dark matter. This has been incredibly successful at explaining the present observations, but it has several initial condition problems. Isotropy and homogeneity are, at first, postulated via the cosmological principle. An almost scale invariant distribution of matter anisotropies must be present at the initial time in order for structures (galaxies and galaxy clusters) to form as we observe them today. The big bang model considers a thermalized universe, but during the early instants the universe expansion is so fast that thermalization cannot be reached in time. Inflation consists on a period of fast, accelerated expansion instants after the beginning of the universe, and became the ideal complementary theory to the big bang. It realizes homogeneity and isotropy dynamically, leaves fields thermalized and with the distribution of anisotropies just as needed for explaining the observations. As a bonus, if the phase transitions associated with spontaneous symmetry breakings happen before inflation, the resulting defect networks are stretched many times beyond the horizon, effectively rendering them undetectable.

If the phase transition happens after inflation, then defect networks can form and remain until the present time. For domain walls, that can be a problem, if their tension too large. In the past literature, an initial condition bias was considered and domain wall networks were seen to decay in a short amount of time, the most plausible mechanism for generating that bias being inflation. However, the scale invariant initial conditions had never been properly taken into account when studying their dynamics. In this thesis we present the first study of the post inflationary domain wall dynamics. What we found is exceptional—these post inflationary domain wall networks are very resilient to initial condition biases, and thus will not decay unless other mechanisms force them to. This finding greatly constrains theories which generate domain walls, unless other aspects of the theory are in place to avoid wall domination.

The cosmic microwave background (CMB) is the light scattered from the primordial plasma at recombination, when free electrons and protons combined to form neutral hydrogen. The CMB light is one of our best probes into the early universe and has been the gateway to precision cosmology, the era we currently live in which accurate measurements of cosmological parameters have been reached. The CMB light contains information not only about the universe at the time of recombination, but also of the media it has propagated along. For example, we have precisely modeled and measured the anisotropies induced in the CMB by the metric perturbations sourced by the galaxies and galaxy clusters around us. The isotropic rotation of the CMB polarization has been first measured in recent years, which is an indication of parity-violating interactions. This is called cosmic birefringence, as it is as if spacetime was filled with a medium of polarization-dependent refractive index. Axions couple to light through a parity-violating coupling, and thus are now in the limelight as the most plausible explanation for this rotation. By considering a stable domain wall network we can predict how much the CMB light is rotated. The value of the isotropic cosmic birefringence is in line with the current experimental hint, and the predicted anisotropic cosmic birefringence is well within the reach of next-generation CMB polarization probes.

Let us now introduce the contents of this thesis. In Ch. 2 we will review standard cosmology—the ΛCDM model, the thermal history of the universe, evidences for dark matter as well as its open problems. In Ch. 3 we will study topological defects in detail—which, when and whether they form. Axions are presented as the most plausible class of theories leading to the domain wall formation. Domain wall properties and dynamics are also explained up to what was known previous to our research. In Ch. 4 we present the dynamics of unbiased domain walls, as well as novel insights in regards to why an attractor solution is reached. In Ch. 5 we show their biased dynamics. Domain wall network stability is quantified, and we study how the network lifetime depends on the initial conditions and bias. In Ch. 6 we do a review of CMB physics at the same time that we show the multiple signatures which a domain wall network would leave—cosmic birefringence among them. The summary and conclusions are written in Ch. 7.

Chapter 2

Cosmology

Modern cosmology began with the development of the theory of general relativity by Einstein [7]. Thanks to the contributions of Hubble and Lemaitre, it was discovered that there were galaxies other than ours, and they were receding with larger velocities the more distant they were [8, 9]. This was the first evidence for an expanding universe.

In 1964, Penzias and Wilson discovered an apparently homogeneous microwave signal coming from the sky—the cosmic microwave background (CMB) [12]. Under the big bang model, after electrons and protons combine to form neutral hydrogen, photons decouple leaving a low energy background of light with fluctuations across the sky. Those fluctuations are correlated to the matter fluctuations that had served as seeds for the formation of structures like stars and galaxies. However, no fluctuations were to be seen. This smoothness was puzzling and even seemed to go against causality: how come regions very far apart on the sky all seemed to have very similar temperatures?

The first proposal for abundant quantities of non-luminous matter was made by Oort in 1932 after seeing that the motion of stars in the milky way could not be explained by luminous matter alone [10]. Just one year later, Zwicky observed that the velocities of the galaxies in the Coma cluster were much higher than expected from luminous matter estimations [11]. The measurement of galaxy rotation curves other than the Milky Way by Rubin and collaborators in 1970 became even further evidence for **dark matter** [13], and its existence around galaxies and clusters became widely accepted. Cold dark matter (CDM) could explain structure formation even starting from comparatively small initial fluctuations [17] and would explain why no anisotropies had been seen yet in the CMB.

In three independent papers, Starobinski, Guth and Sato proposed different models of periods of rapid expansion (**inflation**) which explained the homogeneity of the universe and also eliminated the need for fine tuning to explain the flatness of the universe [14, 15, 16].

The long awaited observation of the CMB anisotropies was published in 1992 by the COBE experiment [22]. Simultaneously, evidence started to pile up for accelerated expansion driven by some kind of dark energy. Redshift measurements of H_0, estimates of the age of the universe, constraints on cosmological parameters from gravitational lensing, the amount of gas in galaxy clusters... [18, 19]. In

1998, high redshift SNIa measurements sealed the deal [20, 21]. Two years later, the Boomerang and Maxima-1 experiments observed the first of the CMB power spectrum peaks [23]. This was the start of the current era of precision cosmology in which the values of cosmological parameters are being measured to precision of a few percents.

In this section we will do a review of the basics of cosmology and the ΛCDM model. The reader is referred to more in-depth books about cosmology for a comprehensive review [2, 5, 6].

2.1 The lambda CDM model

The ΛCDM is a model of the geometry and dynamics of the universe. There are three key assumptions: [4]

1. **The cosmological principle.** The universe is homogeneous and isotropic. Let us see what this means precisely.

    - Observable properties of the universe are isotropic. Everything around us appears to be highly anisotropic but it may be reasonable to assume that physical magnitudes, when averaged over sufficiently large volumes, appear to be direction independent for some observers. We know from deep sky surveys and simulations that structures in the universe are usually smaller than 260 Mpc in size [24] while the size of the observable universe is about 30 Gpc. Observers in an universal rest frame (called fundamental observers) can thus realize this averaging process meaningfully. We observe a nonzero CMB dipole moment (light coming from one hemisphere is red shifted while the other is blue shifted), which lets us know our movement with respect to the rest frame. In this way, isotropy is essentially testable.

    - We can observe a fair sample of the whole universe, thus our position is not preferred (homogeneity). This implies that if we moved somewhere else we would observe the same physical laws and parameters as we do now, which is essentially untestable.

    Notice that homogeneity and isotropy are introduced in the model axiomatically through the cosmological principle, but inflation can realize them dynamically. In this way, this first assumption can be either the cosmological principle or inflation.

2. **The only relevant interaction is gravity.** This is a fair assumption to make, since the strong force is confined and weak/electromagnetic forces can be neglected over cosmological distances.

3. **General relativity.** We can derive the form of the metric just from the high level of symmetry stated in the cosmological principle, but to obtain its dynamics we need a theory of gravity. So far, the most successful theory of gravity is general relativity.

2.1.1 Geometry

Let us have $g_{\mu\nu}$ the metric tensor of our space, $\mu, \nu = [0, 3]$. For fundamental observers we can identify the spatial part of this metric g_{ij} ($i, j = [1, 3]$) and its time component g_{00}. This defines a global time coordinate t which we call physical/cosmological time. The metric can be found as follows:

- Isotropy requires that all g_{0i} and g_{i0} components are zero, otherwise they would define a preferred direction.
- Homogeneity and isotropy implies that g_{ij} is invariant under SO(3), i.e. it has rotational symmetry.
- 3-space can homogeneously stretch or shrink as a function of time, called the scale factor $a(t)$. This is because we have supposed homogeneity in space but not in time.
- The time component g_{00} can take any constant value. We set $|g_{00}| = 1$ so that physical time is equal to the proper time of fundamental observers. This leaves two possible metric signatures, $(+, -, -, -)$ and $(-, +, +, +)$, for $g_{00} = +1$ and -1 respectively. We will use the former.

Coordinates where all of the time dependence is isolated in the scale factor are called comoving coordinates. Using the geodesic deviation equation it can be shown that the line element takes the following form [34]

$$\mathrm{d}s^2 = \mathrm{d}t^2 - a^2(t)\left[\frac{\mathrm{d}r^2}{1 - Kr^2} + r^2\mathrm{d}\Omega^2\right]. \tag{2.1}$$

where K is the curvature of the space. This is the FLRW metric, short for Friedmann–Lemaître–Robertson–Walker. The curvature $K > 0$ corresponds to a closed universe (spherical geometry). If $K = 0$ then the universe is flat (Euclidean geometry). If $K < 0$ then the universe is open (hyperbolic geometry). From observations we know that our universe is exceptionally flat.

If the scale factor $a(t)$ grows with time, that would imply an expanding universe and vice versa. Distances measured in comoving coordinates do not change with the universe expansion, but physical distances do,

$$d_{\text{physical}} = a(t)d_{\text{comoving}}. \tag{2.2}$$

There is a constant factor which we may set at our convenience. It can be used to make K dimensionless, normalizing it to either -1, 0 or $+1$, and thus making a have dimensions of [length]. We will let K be dimensionful, and instead make a dimensionless. For a reference time t_0, we define a so that $a(t_0) = 1$. The reference time t_0 is taken to be the present time, and the notation $\bigcirc_0$ is used for variables evaluated at the present. In this notation,

$$d = a(t)d_0. \tag{2.3}$$

Photons move along null trajectories $\mathrm{d}s^2 = 0$. Let us consider a photon moving radially towards an observer in the coordinate center. For that photon:

$$\mathrm{d}t^2 - a^2(t)\mathrm{d}r^2 = 0 \qquad \Longrightarrow \qquad \frac{\mathrm{d}r}{\mathrm{d}t} = \pm\frac{1}{a(t)}. \tag{2.4}$$

Since the photon moves towards the center we take the $-$ solution. If we denote its time of emission by t_i and its comoving radial coordinate at time of emission by r_i,

$$r_f - r_i = -\int_{t_i}^{t_f} \frac{\mathrm{d}t}{a(t)}. \tag{2.5}$$

The photon is detected at the coordinate center so $r_f = 0$. We can define conformal time as

$$\mathrm{d}\tau = \frac{\mathrm{d}t}{a(t)}, \tag{2.6}$$

so that $r_i = \tau_f - \tau_i$. In terms of τ the line element becomes

$$\mathrm{d}s^2 = a^2(t)\left[\mathrm{d}\tau^2 - \frac{\mathrm{d}r^2}{1 - Kr^2} - r^2\mathrm{d}\Omega^2\right]. \tag{2.7}$$

The factor a^2 is a conformal transformation, thus the name conformal time. Time derivatives are notated the following way:

$$\frac{\mathrm{d}\bigcirc}{\mathrm{d}t} \equiv \dot{\bigcirc}, \qquad \frac{\mathrm{d}\bigcirc}{\mathrm{d}\tau} \equiv \bigcirc'. \tag{2.8}$$

All distances stretch or shrink proportionally to the scale factor, so the same also applies to the wavelength of light $\lambda_i = a(t)\lambda_f$. We can define the redshift z as

$$1 + z \equiv \frac{\lambda_f}{\lambda_i} = \frac{1}{a(t)}. \tag{2.9}$$

The redshift quantifies the stretching of light: if the wavelength doubles since the time of emission, the redshift will be 1 and so on. Redshift is achromatic—it is the same for all wavelengths, thus we can use z as a time coordinate, just like t, τ or a.

Note that all of this analysis is only valid for a fundamental observer. It may be odd to think that there is a preferred frame of reference, but keep in mind that even if it is so for this particular realization (our universe), the theory as a whole is still Lorentz invariant.

2.1.2 Dynamics

We are now interested in the dynamics of this system, that is, on the particular form of $a(t)$ depending on the matter-energy contents of the universe. The field equations of general relativity are

$$G_{\mu\nu} + \Lambda g_{\mu\nu} = 8\pi G T_{\mu\nu}, \tag{2.10}$$

where $G_{\mu\nu}$ is the Einstein tensor, $g_{\mu\nu}$ is the metric tensor, $T_{\mu\nu}$ is the stress–energy tensor, Λ is the cosmological constant and G is the gravitational constant. It is assumed that all forms of energy in the Universe can be described as perfect fluids in adiabatic expansion with a total density $\rho = \sum_i \rho_i$ and pressure $P = \sum_i P_i$ as defined in their rest frame. We can convince ourselves that this is a good approximation since any heat transfer would define a preferred direction, which is not allowed by isotropy. The corresponding stress-energy tensor is

$$T^{\mu\nu} = P g^{\mu\nu} + (P + \rho) U^{\mu} U^{\nu}, \tag{2.11}$$

where U^{μ} is the 4-velocity relative to a comoving observer. If we introduce the FLRW metric and the perfect fluid stress-energy tensor into the field equations we obtain two independent equations, called the first and second Friedmann equations

$$\left(\frac{\dot{a}}{a}\right)^2 = \frac{8\pi G}{3}\rho - \frac{K}{a^2} + \frac{\Lambda}{3}, \tag{2.12}$$

$$\frac{\ddot{a}}{a} = -\frac{4\pi G}{3}(\rho + 3P) + \frac{\Lambda}{3}. \tag{2.13}$$

We can obtain the continuity equation by taking the covariant derivative of the stress-energy tensor

$$\dot{\rho}_i + 3\frac{\dot{a}}{a}(\rho_i + P_i) = 0. \tag{2.14}$$

Energy conservation in flat space relies on time translation symmetry. The continuity equation adapts that concept to an expanding universe, where energy density decreases as the universe expands and vice versa. Notice that this is not independent from the Friedmann equations. Picking any two of the three will suffice, so usually the first Friedmann equation and the continuity equation are chosen as they are of first order in derivatives and thus easier to work with.

To solve this system we need to fix the equation of state, that is, how P and ρ are related. The simplest would be something of the form

$$P = w\rho \qquad \xrightarrow[\text{continuity eq.}]{} \qquad \rho(t) = \rho_0 a^{-3(1+w)}, \tag{2.15}$$

where w is a dimensionless number. Conveniently, we can study the behaviour of all matter contents with this simple of the equation of state.

- Non relativistic matter is called dust in this context. This includes regular baryonic matter as well as dark matter. Their velocities are small, thus $P_m \ll \rho_m$ and consequently $\rho_m(t) = \rho_{m0} a^{-3}$. This is an intuitive result—if space expands but the amount of matter remains constant, the energy density will decrease proportionally to the volume (geometrical dilution).

- Relativistic matter is called radiation. To obtain its equation of state, we first note that the trace of the perfect fluid stress-energy tensor is $\mathrm{tr}\,(T_i^{\mu\nu}) = 3P_i - \rho_i$ and the electromagnetic stress-energy tensor is traceless, so $P_r = \rho_r/3$. Using statistical physics, the same result is obtained even for non electromagnetic radiation. We then have $w_r = 1/3$ and $\rho_r(t) = \rho_{r0} a^{-4}$. Intuitively, there is a factor a^{-3} due to geometrical dilution, and an extra a^{-1} factor because of the expansion of its wavelength (redshift).

- About the cosmological constant, Lorentz invariance requires that in local inertial coordinate systems, $T^{\mu\nu}$ of the vacuum must be proportional to the Minkowski metric $\eta^{\mu\nu}$. In a general coordinate system, $T_{\Lambda}^{\mu\nu} \propto g^{\mu\nu}$. Comparing this to the stress energy tensor of a perfect fluid, we see that $P_{\Lambda} = -\rho_{\Lambda}$ and thus $w_{\Lambda} = -1$ and $\rho_{\Lambda}(t) = \rho_{\Lambda 0}$. Regardless of the universe expanding or contracting its energy density stays the same.

An important parameter when talking about the expansion of the universe is the Hubble parameter, also called Hubble rate or function

$$H(t) \equiv \frac{\dot{a}(t)}{a(t)}. \tag{2.16}$$

Its present value is the Hubble constant $H_0 = H(t_0)$, which is what Hubble first measured in 1929 when he observed the linear relationship between receeding velocity and distance of galaxies $v = H_0 l$. The Hubble constant is parametrized in terms of a dimensionless number h ("small h")

$$H_0 = 100h \, \frac{\mathrm{km}}{\mathrm{s} \cdot \mathrm{Mpc}}. \tag{2.17}$$

Early measurements could only narrow it down to $h = 0.5 \sim 1$. Even though nowadays we know its value more precisely $(0.67 \sim 0.74)$, the $4 \sim 6\sigma$ tension in its value between different experiments has led cosmologists to keep using this parametrization. It became customary to use h^{-1}Mpc as the unit of length or $h^{-1}M_{\odot}$ as the unit of mass so that the uncertainty in its value drops off the calculations.

The Hubble parameter has dimensions of $[\mathrm{time}]^{-1}$, so we can obtain a characteristic time scale called the Hubble time t_H by inverting its value

$$t_H = \frac{1}{H(t)}. \tag{2.18}$$

The conformal Hubble parameter $\mathcal{H}$ is defined as,

$$\mathcal{H}(\tau) \equiv \frac{a'(\tau)}{a(\tau)}. \tag{2.19}$$

The "classical" and conformal Hubble parameters are related

$$H(t) = \frac{\dot{a}}{a} = \frac{a'}{a^2} = \frac{1}{a}\mathcal{H}(\tau). \tag{2.20}$$

Inverting them leads to physical H^{-1} and comoving $\mathcal{H}^{-1}$ length scales, which are called physical and comoving Hubble radius respectively. It is conventional in the literature to just denote those length scales by the Hubble parameter inverses, without the usage of other symbols.

In this thesis we are only interested in comoving wavenumbers. The comoving wavenumber corresponding to the Hubble horizon is

$$k_H = \frac{2\pi}{\mathcal{H}^{-1}} = 2\pi a H. \tag{2.21}$$

We can define an energy density for the cosmological constant as

$$\rho_\Lambda = \frac{\Lambda}{8\pi G}, \tag{2.22}$$

so that the first Friedmann equation becomes

$$\left(\frac{\dot{a}}{a}\right)^2 = \frac{8\pi G}{3}\rho - \frac{K}{a^2}, \qquad \rho = \sum_i \rho_i = \rho_r + \rho_m + \rho_\Lambda. \tag{2.23}$$

It is customary define the critical density ρ_{cr} as

$$\rho_{\text{cr}}(t) \equiv \frac{3H^2(t)}{8\pi G}. \tag{2.24}$$

If $\rho > \rho_{\text{cr}}$, then the universe will be closed ($K > 0$) and vice versa. This is an important scale in cosmology, so it is used to convert the energy densities into dimensionless quantities called the density parameters $\Omega_i(t)$

$$\Omega_i(t) = \frac{\rho_i(t)}{\rho_{\text{cr}}(t)}. \tag{2.25}$$

Both are frequently used in their present values

$$\rho_{\text{cr}0} = \frac{3{H_0}^2}{8\pi G}, \qquad \Omega_{i0} = \frac{\rho_i(t_0)}{\rho_{\text{cr}0}}. \tag{2.26}$$

We can substitute these in the first Friedmann equation to obtain

$$H^2(a) = {H_0}^2\left[\Omega_{r0}a^{-4} + \Omega_{m0}a^{-3} + \Omega_{K0}a^{-2} + \Omega_{\Lambda 0}\right], \tag{2.27}$$

where we have defined the density parameter of curvature as

$$\Omega_{K0} \equiv -\frac{K}{{a_0}^2{H_0}^2}. \tag{2.28}$$

Notice how, since we already used the continuity equation for Eq. (2.15), just one equation suffices. If we set $a = 1$ we see that the sum of all density parameters must be one

$$\Omega_{r0} + \Omega_{m0} + \Omega_{K0} + \Omega_{\Lambda 0} = 1. \tag{2.29}$$

The values obtained for the cosmological parameters from CMB fluctuations by the Planck collaboration are [26]

$$\begin{aligned} H_0 &= 67.66 \pm 0.42 \text{ km/s/Mpc}, \\ \Omega_{m0} &= 0.3111 \pm 0.0056, \\ \Omega_{c0} h^2 &= 0.11933 \pm 0.00091, \\ \Omega_{b0} h^2 &= 0.02242 \pm 0.00014, \\ \Omega_{\Lambda 0} &= 0.6889 \pm 0.0056, \\ \Omega_{K0} &= 0.0007 \pm 0.0037, \\ \Omega_{r0} h^2 &= 2.47 \cdot 10^{-5}, \end{aligned} \tag{2.30}$$

where Ω_{c0} represents cold DM and Ω_{b0} baryonic matter. Right now the universe is dominated by the cosmological constant, but it was not always this way. It is evident from Eq. (2.27) that as we go back in time there will be a period where Ω_m was the largest, and before that a period where Ω_r dominated. From observatios we know that the matter radiation equality (when $\Omega_r = \Omega_m$) happened at $z \sim 3400$. Since $z \sim 0.3$ the cosmological constant started to dominate. During the radiation dominated era, we can integrate Eq. (2.27) and dismiss the non-Ω_r terms to find

$$\text{(Radiation dominated era)} \quad a \propto t^{1/2}, \quad H = \frac{1}{2t}. \tag{2.31}$$

Similarly, for the matter dominated era,

$$\text{(Matter dominated era)} \quad a \propto t^{2/3}, \quad H = \frac{2}{3t}. \tag{2.32}$$

If the cosmological constant dominates, then

$$\text{(Cosmological constant)} \quad a \propto e^{H_0 t}, \quad H = H_0. \tag{2.33}$$

2.2 Thermal history of the universe

We now shift our focus to the history of the universe. First, why is it called "thermal history"? The universe is expanding, therefore it was denser and hotter in the past. Particles collided frequently so we can assume that the universe was in a state of thermal equilibrium, with an associated temperature T. What this means is that there was enough energy in this plasma to generate through collisions any particles of mass $m < T$. We are then free to use temperature T as a time coordinate, just like t, τ, a or z. If we set the Boltzmann's constant to unity $k_B = 1$ then we can measure temperature in units of energy. Processes in the early universe (decouplings, symmetry breakings) occur at particular energies, which makes T an extremely useful time coordinate.

For much of the early history of the universe the equation of state of a relativistic ideal gas applies,

$$\rho(T) = \frac{\pi^2}{30} \mathcal{N}(T) T^4, \tag{2.34}$$

where $\mathcal{N}(T) = \mathcal{N}_b(T) + \frac{7}{8}\mathcal{N}_f(T)$. $\mathcal{N}_b(T)$ and $\mathcal{N}_f(T)$ are the effective number of degrees of freedom of bosons and fermions with masses $m \leq T$. Particles heavier than the equilibrium temperature $m \gg T$ decay and collisions are not energetic enough to generate them, so their equilibrium density is exponentially suppressed.

Particles decouple from thermal equilibrium once their interaction rate Γ falls below the Hubble expansion rate H. The decoupling temperature T_d is defined as when $\Gamma(T_d) \approx H(T_d)$. Heavy particles, those for which $m \gg T_d$, decouple at negligible densities since they have already decayed almost completely. Massless particles and those for which $m \ll T_d$ will decouple with significant relic densities.

Several phase transitions occur in the early universe. This is nothing else that the spontaneous symmetry breaking (SSB) of the theories that describe particles and forces in our universe. From a field theoretical point of view, as the universe cools down the effective Lagrangian changes. There is a transition energy after which the symmetries of the vacuum states are not those of the full theory. We will study SSB more in detail in Sec. 3.1.

Let us see the main events in the history of the universe:

- During the very first moments of the universe, we do not know what happened. The Planck energy $E_{\mathrm{P}} = \sqrt{\hbar c^5/G} = 1.2 \cdot 10^{19}$ GeV sets the scale at which general relativity breaks down and quantum gravity effects start to dominate (Planck epoch). If all forces of nature unify at high energies, the gravity phase transition will had happened during this epoch.

- Grand unified theories (GUT) are well motivated theoretically and propose that electroweak and strong forces unify at $T_{\mathrm{GUT}} \sim 10^{16}$ GeV. If that is the case, there will be a GUT phase transition at that energy scale. GUT transitions are known to leave behind exotic relics like monopoles, exotic particles and in some cases, small black holes, none of which we see nowadays. **Inflation** is thought to happen either during or after the GUT transition, rapidly expanding the universe and diluting the number density of relics into undetectable levels. After inflation, the universe is very flat and homogeneous. The potential energy of the inflaton field becomes standard model particles through a process called **reheating**. During inflation, the inflaton field develops small fluctuations, which then become the matter density fluctuations.

- At some point which we are unsure of, some process led to **dark matter production**. Depending on the nature of dark matter, this process changes. In the case of WIMPs they would just decouple from the plasma, leaving a cosmic dark matter background. In the case of axions, the misalignment mechanism could explain their present abundance.

- If baryons and antibaryons were to be generated at the same rate, they would eventually completely annihilate into photons. Some unknown process in the early universe (baryogenesis) introduced a baryon-antibaryon asymmetry that led to the matter density and matter-to-photon ratio that we observe today.

- The mass of the Higgs boson is $M_H = 125$ GeV so we expect that at $T_{\mathrm{EW}} \approx 150$ GeV the electroweak phase transition will take place. W and Z bosons obtain mass through the Higgs mechanism and decouple shortly after. For temperatures above T_{EW} the electroweak force had long range, but after the decoupling of the force carriers the weak force becomes of short range.

- At $T_{\mathrm{QCD}} \approx 150$ MeV the QCD phase transition takes place. The quarks that have not decayed yet (up, down and strange) condense into hadrons—mostly protons, neutrons and pions.
- At 1 MeV, neutrinos decouple. Since their mass is much smaller than this decoupling temperature they do so with a high relic abundance. We call it the cosmic neutrino background. During this early period where Ω_r dominates, neutrinos carried about 40% of the total energy density of the universe. We have not directly measured it yet but its consequences are seen in the CMB and the clustering of galaxies.
- At 100 keV, the energy of the photons becomes low enough that deuterium does not get immediately photodissociated. This leads to a chain of reactions in which protons and neutrons combine to form deuterium, helium and lithium (**big bang nucleosynthesis**). Almost all neutrons end up in ^{4}He, due to the lack of stable nuclei with mass number 5 or 8 as well as the high Coulomb barrier of the required reactions. Electrons, protons, neutrons and photons were the last particles remaining in the equilibrium plasma.
- At 0.8 eV, the densities of matter and radiation became comparable (matter-radiation equality).
- At 0.3 eV ($z = 1100$) electrons and protons combined to form hydrogen atoms (**recombination**) and the amount of free charged particles decreased considerably. The universe used to be opaque for photons as they scattered off charged particles (Thomson scattering), but after recombination, photons decoupled. Those free-streaming photons are what we now see as the CMB.
- At 4 meV the gravitational collapse of H, He and Li gas led to the formation of the first structures (stars, quasars, etc). The energetic radiation from those objects ionized the neutral hydrogen gas around them (reionization).
- At 0.33 meV, the universe becomes dilute enough for the cosmological constant to dominate its expansion.

2.3 Observational evidence for dark matter

Although no direct detection has been made yet, there are several observations which can be explained by the existence of dark matter. The evidence is strong and it is one of the driving factors for motivating theories beyond the standard model.

Galaxy rotation curves

The arms of spiral galaxies rotate around the galactic center. Ignoring their peculiar velocities, stars at a distance R from the center will orbit with a speed

$$v(R) = \sqrt{\frac{GM(R)}{R}}, \tag{2.35}$$

where $M(R)$ is the total mass contained in a sphere of radius R. Most of the luminous matter is in the galactic center, so we would expect $v(R) \propto R^{-1/2}$. However, the observed velocity far from the center is approximately constant, implying that $M(R) = R{v_0}^2/G$ the mass continues increasing even if the visible disc fades. Dark matter seems to represent about $80 \sim 90\%$ of the total mass of galaxies.

Gravitational lensing

Galaxy clusters are some of the largest gravitationally bound structures in the universe. They consist of hundreds to thousands of galaxies, which we observe in the near-infrared and optical, and heated gas between the galaxies, which emit x-rays via thermal bremsstrahlung. The gravitational well of very massive objects such as galaxy clusters can bend the trajectory of light passing close to them (gravitational lensing). Luminous objects behind a galaxy cluster can appear duplicated or distorted forming an arc shape, whose radious of curvature is related to the mass within the cluster, which gives a way of probing their mass just through gravitational interaction. Telescope and lensing observations combined reveal that just 1% of the total mass is in the galaxies, 9% is in the intracluster gas while dark matter comprises the remaining 90% [39].

The lensing from small astrophysical objects is not enough to form measurable arcs but can cause measurable changes in the brightness of objects behind them (microlensing). Objects like brown dwarfs, neutron stars, black holes and rogue planets (MACHOs) are non-luminous and in theory could be candidates for dark matter. Several collaborations have searched for these objects in the Milky Way halo through gravitational microlensing and concluded that their number density is too low to be the dominant dark matter component [35].

Bullet cluster

The Bullet cluster is interesting since it reveals the aftermath of a galaxy cluster collision. Distances between galaxies are large, so after the collision they were gravitationally slowed but otherwise unaltered. The intracluster gases were compressed and shock heated, increasing its x-ray emissions. Its baryonic center of mass (from x-ray observations) and its total center of mass (from gravitational lensing) are

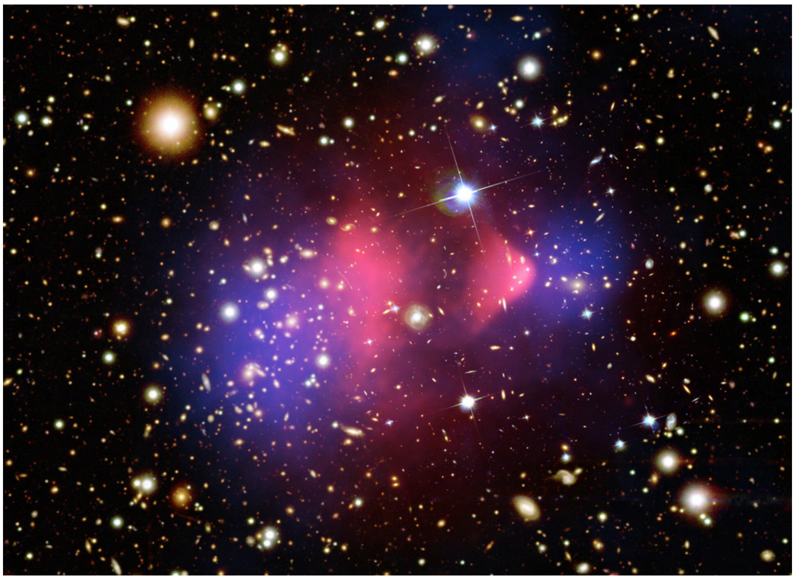

Figure 2.1: Composite image of the bullet cluster. In red, zones of high X-ray emission. In blue, the mass distribution deduced from gravitational lensing. Credit: NASA/D. Clowe et al. [38].

different with a certainty of 8σ [38]. In Fig. 2.1 we see how dark matter passed right through after the collision. This result can not be explained with theories of modified gravity (e.g. MOND) which assume that dark matter does not exist[33].

Large scale structure

Two effects dominate structure formation: gravitational interaction attracts matter in the centres of masses, and the expansion of the universe drives structures away from eachother. Simulations like the Millenium simulation revealed that, with the currently known cosmological parameters, filaments of matter are formed on which the number of structures is much larger, which is in agreement with the observations of galaxy surveys [37]. The observed and simulated matter density power spectrums are also in agreement for the measured cosmological parameters.

CMB and light element abundances

During the big bang nucleosynthesis protons and neutrons form deuterium, helium and trace amounts of lithium and other light elements. This is the main generating process of deuterium in the universe, as any deuterium produced or found in stars immediately fuses into ^{4}He. Studying the ratio of deuterium to hydrogen D/H in areas of low stelar activity gives an upper bound for primordial deuterium levels. It turns out that D/H is heavily dependent on the baryon density. From deuterium observations it is seen that $\Omega_b h^2 = 0.022$, in agreement with CMB observations.

2.4 Open problems

The ΛCDM model and inflation comprise the current paradigm of cosmology and can successfully explain many cosmological observations. However, we know that it is far from a fundamental theory—its three basic components (inflation, cold dark matter and cosmological constant) are based just on cosmological observations with no link to the standard model of particle physics. Despite extensive experimental efforts, no direct detection of any dark matter particle candidates has been done yet, which is puzzling as we do not know what mechanism is driving its couplings to be so small. The value of Λ is tens of orders of magnitude smaller than the contributions from the vacuum energy densities of the particle fields (cosmological constant problem), which poses a serious fine tuning problem. Moreover, the particulars of the processes that happened during baryogenesis and the Planck epoch are unknown.

Some present observations are of particular interest since, if no systematic error is present, they go directly against the predictions of ΛCDM . The most notable is the Hubble tension, a $4 \sim 6\sigma$ tension between the model-independent direct local measurements (Cepheids, SNIa, ...) and the ΛCDM dependent high redshift indirect probes (CMB) [27].

$$\begin{aligned} H_{0,\text{CMB}} &= 67.27 \pm 0.66, \\ H_{0,\text{SNIa}} &= 73.2 \pm 1.3. \end{aligned} \tag{2.36}$$

Another tension between the Planck CMB data and redshift surveys has been reported, about the values of Ω_m and the rate of growth of structure σ_8 with a statistical significance of 2σ [25].

Many observations are pointing out that the universe may violate the cosmological principle [31]. The homogeneity scale (the argument that averaging over 260 Mpc gives a homogeneous universe) may not be true as structures of up to 3 Gpc in size have been found. Additionally, anisotropy at large scales is theoretically motivated [32] and several observations support this idea [31]. The anomaly of most statistical significance is the dipole anomaly. The CMB dipole is subtracted on the assumption that it is simply due to our relative motion and fixes the CMB as the Universe's rest frame. However, recent low redshift measurements from quasars, radio sources and supernova Ia reveal that, although the direction is the same, the dipole amplitude is larger, disagreeing with the Planck CMB measurements at 4.9 σ [28, 29, 30].

The present evidence for new physics motivates the study for theories beyond the standard models of both particle physics and cosmology, with the objective of explaining these open problems. Some of those theories, as we will see later, can lead to the production of domain walls, which can have significant impact in cosmology. The recent surge in hints of violations of the cosmological principle could be related to the presence of large scale inhomogeneities like domain walls, which further motivates the study of their properties and dynamics.

Chapter 3

Cosmological domain walls

Spontaneous symmetry breaking is at the core of our modern understanding of physics and cosmology. Topological defects are stable structures generated after spontaneous symmetry breaking and have important cosmological consequences. Although ubiquitous in condensed matter physics, none have been yet observed in a cosmological context, which has been key in imposing constraints in our models such as when the symmetry breaking occurs (e.g. before inflation so that defects are diluted away) or the parameters of axion models (e.g. to avoid the domain wall problem).

In Sec. 3.1 we review spontaneous symmetry breaking and Nambu-Goldstone bosons. In Sec. 3.2 we study what are topological defects, as well as why, when and which are formed. In Sec. 3.3 we review the basics of axion models, which are well motivated theories leading to domain wall network generation in the universe. In Sec. 3.4 we delve into the dynamics and cosmological impact of domain walls networks.

3.1 Symmetry breaking

Symmetries are transformations of the fields that leave the equations of motion unchanged. As they map solutions of the equations of motion to other equivalent solutions, they simplify the study of a system by letting us focus on just one representative solution. Symmetries are classified in different categories depending on how they act on the field. A symmetry is global if it acts in the same way at every point, and local if it acts differently at different places in space. Symmetries can be continuous, like time and spatial translations, or discrete, like time reversal and parity.

Transformations describing symmetries form a **group**: a mathematical structure that lets us operate with them just as we would with number systems. I will not do a full review of group theory, but let us review the minimum that the reader should know in order to understand this thesis. A group is formed by a set and an operation (in this case, symmetry composition) that takes two items from the set and gives another element from the same set. The operation is associative, there is an identity element and every element has an inverse. Group elements do not need to be commutative.

Discrete groups are formed by a discrete set of elements. In physics the most notable example is the cyclic group, usually notated as Z_n since it is isomorphic to the additive group of integers modulo n. The smallest non-trivial cyclic group is Z_2, which we can visualize as left-right symmetry. Continuous groups, also called Lie groups, are formed by an infinite set of elements. In physics, the orthogonal and unitary groups are of particular importance.

- The orthogonal group $\mathrm{O}(n)$ is the group of $n \times n$ orthogonal matrices. We can think of $\mathrm{O}(n)$ as the group of distance-preserving transformations in Euclidean space of dimension n that also preserve a fixed point. The determinant of an orthogonal matrix is ± 1, each corresponding to a connected component of $\mathrm{O}(n)$. $\mathrm{SO}(n)$ is the group of $n \times n$ orthogonal matrices of determinant $+1$. We can visualize it as rotations in Euclidean space. The component of orthogonal matrices with determinant -1 does not form a group and corresponds to the reflections in Euclidean space.
- The unitary group $\mathrm{U}(n)$ is the group of $n \times n$ unitary matrices. $\mathrm{U}(1)$ corresponds to the circle group, e.g. the complex unit circle under multiplication. For $n > 1$ it becomes non-commutative, and is isomorphic to the multiplicative group of complex numbers $\mathbb{C}^n$. $\mathrm{SU}(n)$ is the group of $n \times n$ unitary matrices with determinant $+1$. $\mathrm{SU}(2)$ is a double covering of $\mathrm{SO}(3)$ (rotations in Euclidean 3D space).

The symmetries of the standard model are $\mathrm{SU}(3)\times\mathrm{SU}(2)\times\mathrm{U}(1)$, where $\mathrm{SU}(3)$ corresponds to the QCD color symmetry and $\mathrm{SU}(2)\times\mathrm{U}(1)$ to the electroweak symmetry. Grand unified theories are built first by finding a bigger group so that $\mathrm{SU}(3)\times\mathrm{SU}(2)\times\mathrm{U}(1)$ becomes a subgroup. Two notable examples are $\mathrm{SU}(5)$ and $\mathrm{SO}(10)$.

In the context of dynamics, it is conventional to define symmetries as the transformations which leave the Lagrangian unchanged

$$\phi \to \phi', \qquad\qquad \mathcal{L}(\phi', \partial\phi') = \mathcal{L}(\phi, \partial\phi). \tag{3.1}$$

Transformations which leave the Lagrangian unchanged also leave the equations of motion unchanged, although the converse is not true [3]. For example, for a massless scalar field, the transformation $\phi(x) \to e^{\beta}\phi(x)$ is a symmetry but rescales the Lagrangian. We typically use the freedom to redefine the fields to bring the Lagrangian in some canonical form. In this way, we can study the symmetries of the system by studying the Lagrangian.

A necessary condition is that a symmetry should not change the results of an experiment, i.e. the expected values of observables should not change

$$\langle\phi|\, \hat{O}\, |\phi\rangle = \langle\phi'|\, \hat{O}'\, |\phi'\rangle\,. \tag{3.2}$$

It may happen that a system is mostly invariant under a symmetry, but not exactly. There may be some small terms in the Lagrangian/Hamiltonian which do not follow the same symmetries as the rest of the terms. Then we say that the symmetry is **explicitly broken**. These terms may arise because of quantum effects, because of non renormalizable effects... In this case, the equations of motion are no longer invariant.

Spontaneous symmetry breaking (SSB) is the phenomenon in which a stable state of a system (for example the ground state) transforms nontrivially under some symmetries of the theory. These symmetries are then said to be spontaneously broken and the state is called the broken state. Phenomenologically we know that those symmetries exist since they can be seen in the equations of motion, but the stable states are not invariant under it. This is an idea that originated in condensed matter physics, with Heisenberg's theory of ferromagnets [40] and was then adopted into quantum field theory by Baker and Glasgow [43, 44].

The broken state is characterized by a non zero expectation value of the field

$$\langle 0|\,\hat{\phi}\,|0\rangle \neq \langle 0'|\,\hat{\phi}\,|0'\rangle\,. \tag{3.3}$$

If $|0\rangle$ is a broken state, then under the broken symmetry it transforms into $|0'\rangle$ which by definition is different, has the same energy (since the Hamiltonian commutes with the symmetry transformation) and is also a broken state. By repeatedly applying the transformation we can find the set of broken states, all with the same energy.

The existence of a symmetry transformation implies a conservation law. In particular, for symmetries parametrized by continuous variables, the symmetry is associated with a current $j^\mu(x,t)$ which obeys a local continuity equation $\partial_\mu j^\mu = 0$ (Noether's theorem). This holds for a state regardless of it respecting the symmetry of the system! In a broken state, this local conservation law impacts the excitations at non-zero wave number and guarantees the appearance of massless modes known in quantum field theory as **Nambu-Goldstone bosons** [41, 42]. If the symmetry is explicitly broken the bosons will acquire a mass proportional to the size of the explicit breaking term.

In order to understand it in more concrete terms, let us look at an example. The Lagrangian of a complex scalar field Φ is

$$\mathcal{L} = \frac{1}{2}(\partial_\mu \Phi^\dagger)(\partial^\mu \Phi) - V(\Phi,\Phi^\dagger). \tag{3.4}$$

Let us consider V as the so-called mexican hat potential

$$V(\Phi,\Phi^\dagger) = \frac{\lambda}{4}\left(\Phi^\dagger\Phi - \eta^2\right)^2, \tag{3.5}$$

with $\lambda, \eta > 0$. This Lagrangian has U(1) symmetry, that is, rotational symmetry around $\Phi = 0$. We can see how the Lagrangian is invariant under a phase transformation such as

$$\Phi(x) \to e^{i\alpha}\Phi(x). \tag{3.6}$$

The field has a local maximum at $\Phi = 0$ and minima on the circle $|\Phi| = \eta$. Regardless of whether Φ is a classical or quantum field, we can calculate its vacuum expectation value classically. This is because the contribution of any quantum term $\langle 0|\,\Phi\,|0\rangle_{\text{quantum}} = 0$ will be zero due to the stability of the vacuum (tadpole condition). The classical field VEV is found on the potential minima

$$\langle 0|\,\phi\,|0\rangle = \eta e^{i\theta}, \tag{3.7}$$

where a phase θ has appeared, parametrizing the minima. We can see how, when transforming the fields under Eq. (3.6), we go from one vacua to another one $\theta \to \theta + \alpha$. That implies that the vacuum is not U(1) invariant and thus the symmetry is spontaneously broken.

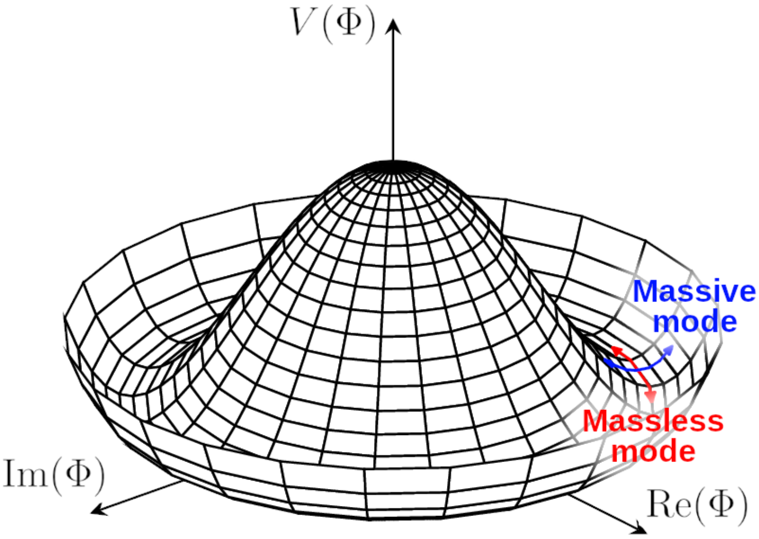

FIGURE 3.1: The potential of Eq. (3.5) with its massless (Nambu-Goldstone) and massive modes highlighted.

Let us keep analyzing what this means. This potential just depends on the modulus squared of the field $V(\Phi, \Phi^\dagger) = V(|\Phi|^2)$ so the potential only varies in the radial direction. We can write the field in the following way,

$$\Phi = (\eta + s)\exp\left(\frac{i\phi}{\sqrt{2}\eta}\right), \tag{3.8}$$

so that s parametrizes movement in the radial direction and ϕ in the angular direction in field space. Its derivative is

$$\partial_\mu \Phi = \left[\partial_\mu s + i\,(\eta + s)\left(\frac{\partial_\mu \phi}{\sqrt{2}\eta}\right)\right]\exp\left(\frac{i\phi}{\sqrt{2}\eta}\right), \tag{3.9}$$

and thus the Lagrangian becomes

$$\begin{aligned} \mathcal{L} &= \frac{1}{2}\left(\partial_\mu s\right)^2 + (\eta + s)^2\,\frac{1}{2\eta^2}\left(\partial_\mu \phi\right)^2 - \frac{\lambda}{4}\left(2\eta s + s^2\right)^2 \\ &= \underbrace{\frac{1}{2}\left(\partial_\mu s\right)^2 - \lambda\eta^2 s^2 + \mathcal{L}_{\text{anh.}}(s^3, s^4) +}_{\text{Massive mode}} \underbrace{\frac{1}{2}(\partial_\mu\phi)^2}_{\text{Massless mode}} + \mathcal{L}_{\text{int.}}(\partial_\mu\phi, s). \end{aligned} \tag{3.10}$$

We see how s behaves as a massive scalar while ϕ is massless, with some interaction terms between s and ϕ. Notice that, despite the interaction terms, ϕ is always massless since it only appears in the lagrangian as $\partial_\mu \phi$, which has shift symmetry. A mass term would have the form $m\phi^2/2$. Both modes and the potential can be seen in Fig. 3.1.

Let us see what happens if this symmetry is explicitly broken by, for example, a non renormalizable term of the form

$$\mathcal{L}_{\mathrm{NR}} = \frac{\Phi^N}{M^{N-4}} + \mathrm{h.c.}, \tag{3.11}$$

where M is the UV cutoff of our effective field theory. If we substitute Eq. (3.8) into it we find that

$$\mathcal{L}_{\mathrm{NR}} = \frac{1}{M^{N-4}} \left(\eta + \frac{s}{\sqrt{2}}\right)^N \cos\left(\frac{N\phi}{\sqrt{2}\eta}\right). \tag{3.12}$$

We see that this term induces a sinusoidal potential for the angular mode, which makes it massive.

3.2 Topological defects

In order to see some analytic topological defect solutions, let us consider the following quartic potential for the real scalar field.

$$V(\phi) = \frac{\lambda}{4}(\phi^2 - \eta^2)^2. \tag{3.13}$$

It is known as the double well potential. It has reflection symmetry across the origin, that is, it is invariant under Z_2. There are two broken states, $\phi = \pm\eta$.

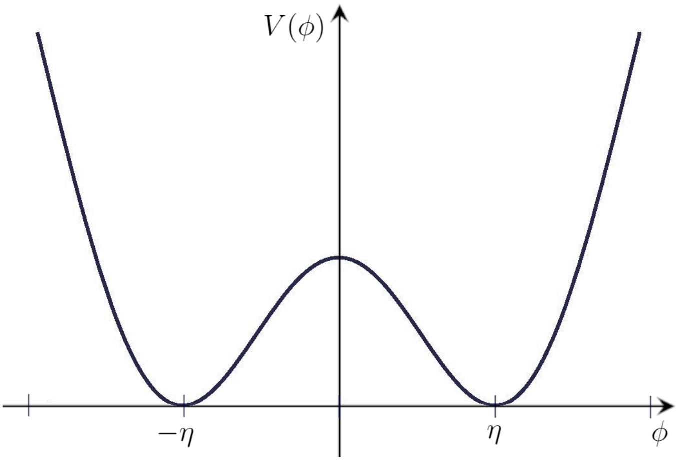

FIGURE 3.2: The double well potential Eq. (3.13).

We can find the following static solution to its equations of motion [1]

$$\phi(x) = \eta \tanh\left(\sqrt{\frac{\lambda}{2}}\eta x\right). \tag{3.14}$$

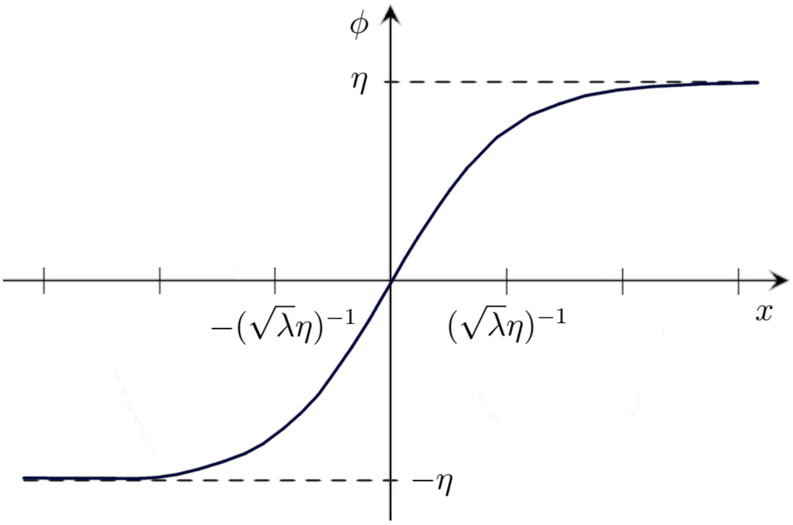

FIGURE 3.3: The domain wall solution of Eq. (3.14).

This is a domain wall, one kind of topological defect. We can see how it interpolates between the two minima of the potential: at $x \to -\infty$ the field is in the negative minima $\phi = -\eta$ and at $x \to +\infty$, $\phi = +\eta$. It has nonzero energy due to ϕ going over the local potential maximum at $\phi = 0$. Moreover, this solution is time-independent and non-dissipative. Due to the Lorentz invariance of the theory, it can also be boosted up to velocities up to the speed of light.

Its stability comes from the non-trivial topology of the vacuum manifold. To eliminate the defect one would have to lift the field over the potential barrier so that all field values are on the same minimum, but this would require a nonzero amount of energy. In this case in particular, infinite energy, since the domain wall has infinite spatial extension.

It is useful to introduce the concept of topological charge. The homogeneous solutions $\phi(x) = \pm\eta$ have topological charge 0, Eq. (3.14) has charge +1 and the defect with opposite sign, charge −1. If two defects with opposite topological charge meet, they annihilate.

3.2.1 Classification

As we have introduced earlier, the existence of topological defect solutions is determined by the topology of the vacuum manifold. Before seeing how this is formalized, I think that it is pedagogical to gain some intuition of how defects look like and in which situations they can appear.

Domain walls are two-dimensional objects which can form when a discrete symmetry is spontaneously broken. For example, the double well potential Eq. (3.13) has broken Z_2 symmetry and thus there are domain wall solutions. More generally, these defects can appear when the vacuum manifold is disconnected. For example, the mexican hat potential with an explicit symmetry breaking term like Eq. (3.11) has N disconnected degenerate vacua, and thus it exhibits N distinct domain wall solutions. The effect of crossing a domain wall will be a shift of the field values, from its value in one vacua to another.

Cosmic strings are one-dimensional objects which can form when a symmetry with some rotational invarince along a plane in field space is spontaneously broken. For example, the complex scalar field with a mexican hat potential showed broken U(1) symmetry, and that system has cosmic string solutions. For a complex scalar field, going around a string in position space will cause a shift in the phase of the field $\theta \to \theta + 2\pi n$. If there is an explicit symmetry breaking term like Eq. (3.11) as well, then we will have defects known as domain walls bounded by strings.

Monopoles are zero dimensional objects that can form when, for example, SO(3) symmetry for a triplet of scalar fields is spontaneously broken. The usual intuition for a monopole comes from electromagnetism, as something with nonzero magnetic charge (i.e. nonzero magnetic flux if wrapped by a sphere). However, this is just for local monopoles. For global monopoles, wrapping around them with a plane in position space would lead to a phase shift of some of its field components, which is similar to the string case but much harder to visualize.

Textures are objects that can form when a non-commutative Lie group (e.g, SU(n) for $n \geq 2$), is spontaneously broken. They consist of localized, twisted configurations of fields which collapse and unwind on progressively larger scales [47].

The relationship between the topology of the vacuum manifold and topological defect solutions was first shown by Kibble [76]. In algebraic topology, a way in which topological spaces are classified is through homotopy theory. This is the formal way to quantify whether a space is connected, has holes or voids. The n^{th} homotopy group $\pi_n(\mathcal{M})$ classifies qualitatively distinct mappings from the n-dimensional sphere S^n into the manifold $\mathcal{M}$. A non-trivial homotopy group signals that topological defects can be formed. The correspondence between defects and homotopy group elements is one to one in most of the simple cases [1]. During this thesis, Table. 3.1 will remain valid but I want to note that the general case is more complicated, particularly when textures are involved [52].

Topological defect	Dimension	Vacuum has...	Homotopy group
Domain walls	2	disconnected components	$\pi_0(\mathcal{M})$
Strings	1	unshrinkable loops	$\pi_1(\mathcal{M})$
Monopoles	0	unshrinkable surfaces	$\pi_2(\mathcal{M})$
Textures	–	unshrinkable hyper-surfaces	$\pi_3(\mathcal{M})$

Table 3.1: Correspondence between topological defects and homotopy groups.

Let us see how these concepts are defined. For a point x in a manifold $\mathcal{M}$ we consider all closed paths passing through that point $f : [0,1] \to \mathcal{M}, \quad f(0) = f(1) = x$. For two paths f_1, f_2, we can build a third one f_3 by path concatenation, that is, first by traveling through f_1 and then f_2. This operation $f_1 \circ f_2 \to f_3$ defines a product within this set. Two paths are said to be homotopic at x if we can continuously deform one into the other without losing contact with x. Any path homotopic to a representative f is placed into its homotopy class $[f]$. These homotopy classes form a group, called the fundamental group $\pi_1(\mathcal{M}, x)$ of the manifold at x. The group product is path concatenation under class multiplication $[f_1][f_2] = [f \circ g]$. The identity is the homotopy class of all loops contractible to x (constant map) and the inverse is obtained by reverting the direction in which the loop is traversed $[f]^{-1} = [f^{-1}]$.

The concept of a fundamental group can then be generalized into homotopy groups. That is, maps $f : [0,1]^n \to \mathcal{M}$ such that their boundary is $f(\delta[0,1]^n) = x$ can be classified into homotopy classes $\pi_n(\mathcal{M}, x)$, which under map concatenation form a group $\pi_n(\mathcal{M}, x)$. The case $n = 0$ is a bit peculiar since it is not a group, but a pointed set. Let us consider maps from a single point into $\mathcal{M}$. If the mappings $f_1(\cdot)$ and $f_2(\cdot)$ belong to the same connected component, they are homotopic $f_1 \sim f_2$. Thus, $\pi_0(\mathcal{M})$ is just the set of path connected components. In the case that $\pi_0(\mathcal{M})$ is non-trivial, it means that the vacuum manifold is not path connected and there will be domain wall solutions.

Let us apply these definitions to the previous example of the mexican hat potential and prove the existence of defect solutions. Its vacuum manifold is the circle S^1. Elements of $\pi_1(S^1)$ are determined by their winding number: how many times the class elements loop around the circle. The winding number is an integer, which is positive if looping clockwise and vice versa. We can use the winding number n to identify each homotopy class $[n]$. The product of $[n]$ with $[m]$ is the class of paths that first loop n times, and then m times. Thus, the product of homotopy classes is equivalent to adding their winding numbers $[n][m] = [n+m]$. This implies that

$$\pi_1(S^1) = \mathbb{Z}, \tag{3.15}$$

which is non-trivial. This means that it has string defect solutions.

The analysis when an explicit symmetry breaking term like Eq. (3.11) is present becomes a bit more complicated. The vacuum manifold becomes the cyclic group Z_N which is disconnected, so there will be domain wall solutions. Only trivial paths can be defined and thus its fundamental group is also trivial, so there are no exact string solutions. However, since the symmetry breaking term is small, we can consider the vacuum manifold to be approximately S^1, which has a nontrivial fundamental group, and thus there will be approximate string solutions. In this case, there will be N_{DW} domain walls attached to each string, where N_{DW} is the number of degenerate vacua.

3.2.2 Production

The topology of the vacuum manifold will determine if defects can form, but that alone does not guarantee their existence. The first mechanism by which defect formation was shown to be causally unavoidable in cosmology is called the Kibble mechanism [76, 77].

There is a tendency for symmetries to be restored at high temperatures [45]. A scalar field whose VEV breaks the symmetry at low energy tends to acquire thermal mass when it is in equilibrium with other particles. It is thought that at the beginning of the universe, the field will be in a phase in which its effective potential is such that the symmetry is unbroken. As the universe expands and cools, the effective potential changes until a point in which the symmetry is spontaneously broken. In this way, SSBs in cosmology usually come together with associated phase transitions.

Kibble stated that, since the universe is expanding and the speed of light is finite, there is a limit to how far information could have travelled at the time of the phase transition. This sets an upper bound for the correlation length ξ of the field values, and thus implies that it is causally unavoidable for the field to choose different vacua at scales larger than this correlation length during the phase transition. This mechanism applies to all topological defects.

The Kibble mechanism was proposed before the introduction of inflationary theories, so this possibility was not considered. If the phase transition happens before inflation, then even if a defect network is formed, it will be later stretched into almost non-existence. On the other hand, if the phase transition happens after inflation, then the regular Kibble mechanism will not apply. Light scalar fields during inflation develop fluctuations at very large scales, which in the simplest case leads to a scale invariant spectrum of fluctuations.

The details of how topological defects form after inflation had been mostly neglected in the literature. Early papers in the context of structure formation talk about “field ordering through Kibble mechanism" and inflationary fluctuations as completely separate cases [48, 50]. Papers in the context of domain wall evolution, even if they try to consider their formation after inflation, fail to correctly take into account the initial condition power spectrum [88, 89, 93]. This is despite an earlier paper by Nagasawa and Yokoyama in which the initial fluctuation power spectrum is properly set up, although the subsequent defect formation and network evolution are not studied [86].

Thus, the study performed in this thesis of domain wall networks forming after inflation sheds much needed light into the field of domain wall dynamics. In Ch. 4 we will see numerical results showing that, indeed, domain wall networks form as well in the case with inflationary fluctuations. What we see from the simulations is that the subhorizon fluctuations lead the field to choose different vacua at different points in space, while the superhorizon fluctuations slightly inhibit defect formation, effectively reducing the amount of domain walls per horizon, among other effects.

Knowing that defect networks can form as long as the phase transition happens after inflation, it only remains to see which theories could lead to these symmetry restorations and phase transitions at the early universe. Grand unified theories predict the formation of monopoles, as the GUT group (for example, SU(5) or SO(10)) is broken leaving $\mathrm{U}(1)_{\mathrm{EM}}$ as an unbroken subgroup. Grand unified theories are formed by non-commutative Lie groups, which when spontaneously broken leads to the formation of textures [47]. In the case of Peccei-Quinn theory, if global $\mathrm{U}(1)_{\mathrm{PQ}}$ is spontaneously broken after inflation then cosmic strings will form. If non-perturbative QCD effects become relevant, then $\mathrm{U}(1)_{\mathrm{PQ}}$ is explicitly broken and domain walls appear between strings, which will collapse and annihilate if the vacuum is unique.

3.3 Axions

Axions are a class of hypothetical light pseudoscalar particles. It was first postulated as a pseudo-Nambu-Goldstone boson generated during the Peccei-Quinn mechanism, a mechanism designed to solve the strong CP problem [54, 55, 56]. We will refer to this particle as the QCD axion. More generally, they are pseudo-Nambu-Goldstone bosons associated with non-linearly realized approximate global U(1) symmetries. These appear, for example, due to the compactification of extra dimensions in string theories [67]. We will refer to these as axion-like particles, or ALPs for short.

The spontaneous symmetry breakings associated with axion models may have happened in our universe. In particular, if they happen after inflation, they could lead to the production of string-wall networks. Let us briefly review the basics of axion physics, as we will refer to some particular axion models and experimental results in the remainder of this thesis.

3.3.1 Theories leading to axions

When solving naturalness problems

The general QCD Lagrangian includes a CP-violating term [53]

$$\mathcal{L}_\Theta = -\Theta \frac{\alpha_s}{8\pi} G^{\mu\nu} \tilde{G}_{\mu\nu}, \tag{3.16}$$

where $-\pi \leq \Theta \leq +\pi$ is a parameter quantifying the amount of CP violation, α_s is the strong fine structure constant, $G^{\mu\nu}$ the color field strength tensor and $\tilde{G}^{\mu\nu}$ its dual. This term induces a neutron electric dipole moment $\propto \Theta$, and stringent experimental upper bounds on it imply that Θ, if nonzero, should be tiny $|\Theta| \leq 10^{-10}$. This is the strong CP problem—in principle we would expect $\Theta \sim \mathcal{O}(1)$, and although there is nothing fundamentally wrong with having a very small value of Θ, this poses a “naturalness” problem for the standard model.

The solution to naturalness problems usually come in the form of a dynamical mechanism protecting the smallness of some parameters of the model. In 1977, Peccei and Quinn postulated an elegant solution to the strong CP problem, which was later shown to lead to a new particle, the QCD axion, independently by Wilczek [56] and Weinberg [55]. A new scalar field, ϕ, is introduced, which has spontaneously broken global $\mathrm{U}(1)_{\mathrm{PQ}}$ symmetry. This modifies the previous Lagrangian term as

$$\mathcal{L} = \left(\frac{\phi}{f_a} - \Theta \right) \frac{\alpha_s}{8\pi} G^{\mu\nu} \tilde{G}_{\mu\nu}, \tag{3.17}$$

where f_a is called the axion decay constant and is the scale of the spontaneous symmetry breaking. The induced potential for ϕ has a minimum at Θf_a, effectively relaxing the QCD CP-violation to zero.

The way in how the field ϕ is introduced into the theory is model dependent, and so are most properties of the associated QCD axion, e.g. its couplings to matter. There are two archetypical models. The KSVZ model introduces additional quarks into the standard model [57, 58], while the DFSZ model is realized without introducing additional fermions by assuming two Higgs doublets [59, 60]. Both are part of the *invisible axion* models, since their couplings to matter are suppressed by $1/f_a$ and thus driven below the current experimental limits. One important property of the QCD axion is that the decay constant and the axion mass are related as $m_{\mathrm{QCD}} \propto 1/f_a$. For a general axion-like particle, this need not be the case.

Axion-like particles could also solve other naturalness problems. For example, a pseudo-Nambu-Goldstone boson with a potential of the form $V(\phi) = \Lambda^4[1 \pm \cos(\phi/f_a)]$ can naturally give rise to an epoch of inflation in the early universe, given sufficiently large f_a and Λ [65]. The relaxion is an ALP with a linear potential $V(\phi) \propto \Lambda^3\phi$, which has been proposed as a solution to the weak scale hierarchy problem [68].

In theories with extra dimensions

String theories are some of the most well developed quantum theories of gravity. They are formulated in more than four dimensions, with all extra dimensions compactified to less than the Planck length, explaining why we have not accessed them yet in colliders and other experiments. High order antisymmetric tensor fields, upon compactification, typically give rise to a large number of zero modes, depending on the topology of the compact manifold. Even in the simplest cases, this leads to hundreds of pseudoscalar fields with axion-like properties. This is known as string axiverse [67]. Intuitively, we can think that, although the extra dimensions are not accessible to us at low energies, fields can oscillate along the compactified dimensions, and those oscillations (with their associated energy levels, etc) manifest themselves as scalar fields in the compactified theory. Depending on the particulars of the string theory, one of these axions could also be the QCD axion.

3.3.2 Time evolution

The equation of motion of a scalar field in a homogeneous background is

$$\ddot{\phi} + 3H(t)\dot{\phi} - \frac{1}{a^2}\nabla^2\phi + \frac{\mathrm{d}V(\phi)}{\mathrm{d}\phi} = 0. \tag{3.18}$$

Its full derivation is shown in Sec. B.2. In the early universe, the spontaneously broken symmetry associated with the axion is expected to be restored. The $3H(t)\dot{\phi}$ term is called the Hubble friction term, and as long as the Hubble parameter is larger than the axion mass $H(t) \gg m$ it dominates, effectively freezing the evolution of the field. The field rolls down the potential, and at $t = t_{\mathrm{osc}}$, $H(t_{\mathrm{osc}}) \sim m(t_{\mathrm{osc}})$ it begins to oscillate around the present vacuum value.

3.3.3 Axion dark matter

One of the most important observables connecting dark matter, particle physics and cosmology is the so-called relic density, the currently observed cosmological density of dark matter. Dark matter could have been in interaction with the thermal bath before decoupling from it, or it could have been generated at a time in which its interaction rate was already low. In addition to that, dark matter need not be a single particle species—as long as they have no charges, are long lived and interact weakly with the standard model particles, the relic density could be the sum of many different components.

Light axions are a compelling candidate for dark matter. A straightforward way in which axion dark matter could be produced is the misalignment mechanism [61, 62, 63]. The axion field value before oscilation is, in general, different from the present value. We can parametrize it as

$$\phi(t_i) - \phi(t_0) = \Theta_{\text{in}} \frac{f_a}{N_{\text{DW}}}, \tag{3.19}$$

with $\Theta_{\text{in}} \in [0, \pi]$ a random parameter called the misalignment angle and N_{DW} the number of equivalent vacua. After the phase transition, the field potential energy gets released as axion particles. If the axion model in consideration behaves as dark matter, this could be part or most of the relic density.

The case closest to our interest is ultralight ALP dark matter, with $m(t_{\text{osc}}) = m(t_0)$. Unlike the QCD axion, m and f_a are independent parameters. Taking the simple harmonic approximation for the axion potential, it can be seen that [71]

$$\left[\Omega_{a0} h^2\right]_{\text{ALP}} \simeq 0.1 \cdot \Theta_{\text{in}}^2 \left(\frac{f_a/N_{\text{DW}}}{10^{17}\,\text{GeV}}\right)^2 \left(\frac{m}{10^{-22}\,\text{eV}}\right)^{1/2}. \tag{3.20}$$

Since the relic density has been very precisely measured, it can be used to set constraints on axion models contributing to dark matter. I want to emphasize, however, that axions need not be dark matter. In particular, if there is a spectrum of axions, as is the case in string axiverse, only the lightest one (or more precisely, only the ones which are long-lived) could contribute to the presently observed relic density.

3.3.4 Experimental searches

Axions have a model-dependent coupling to photons of the form

$$\mathcal{L}_{a\gamma\gamma} = -\frac{g_{a\gamma\gamma}}{4} \phi F_{\mu\nu} \tilde{F}^{\mu\nu} = g_{a\gamma\gamma} \phi \mathbf{E} \cdot \mathbf{B}, \tag{3.21}$$

where $F_{\mu\nu}$ is the electromagnetic field-strength tensor, $\tilde{F}_{\mu\nu}$ its dual, and $g_{a\gamma\gamma}$ the axion-photon coupling [64]. In most models, $g_{a\gamma\gamma}$ is nonzero, but suppressed with the axion decay constant. For a general ALP,

$$g_{a\gamma\gamma} = c_\gamma \frac{\alpha_{\text{EM}}}{\pi f_a}, \tag{3.22}$$

where c_γ is the anomaly coefficient of O(1) and α_{EM} is the fine-structure constant. In the presence of background magnetic fields, Eq. (3.21) induces quantum mechanical oscillations between photons and axions. The stronger and more coherent the magnetic field, the larger the probability of conversion. The process which converts axions into photons is called Primakoff effect. Most direct searches are based on our ability to generate strong and coherent magnetic fields over laboratory scales, trying to convert the elusive axions into the much more easily detectable photons.

The Sun may be a major source of axions, as thermal photons in the solar plasma could be turned into axions by the large electromagnetic fields within. Haloscopes are experiments which try to reconvert those solar axions into photons via large magnetic fields. One of the most notable ones is the CERN Axion Solar Telescope (CAST) [73], which will be followed up by the next-generation experiment IAXO [74]. Light-shining-through-walls experiments aim a photon beam at an opaque wall, with strong magnetic fields both before and after the wall. The probability of a photon oscillating into an axion, crossing the wall and then being detected back as a photon is $\propto {g_{a\gamma\gamma}}^2$.

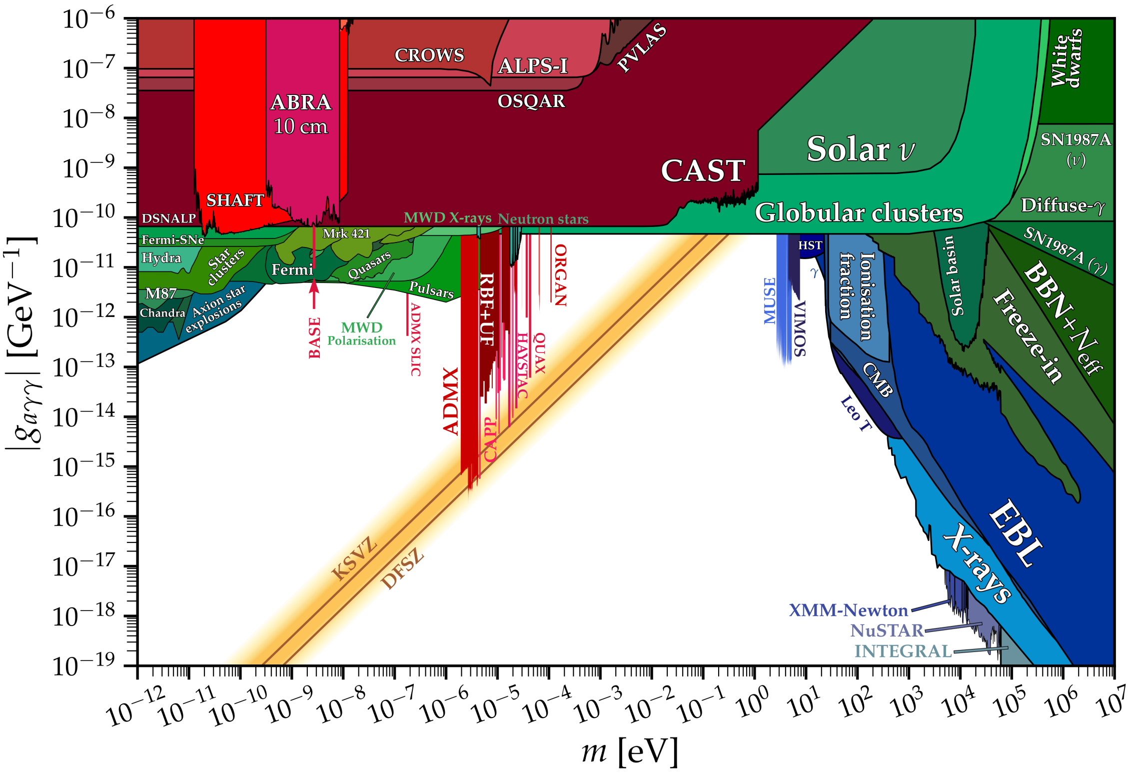

Figure 3.4: Exclusion plot for axion masses m vs axion-photon coupling $g_{a\gamma\gamma}$. In the KSVZ and DFSZ axion models, the relationship between m and $g_{a\gamma\gamma}$ is fixed by the yellow band, but other QCD axion and ALP models can populate the rest of the parameter space. Other solid regions are current experimental bounds. Red corresponds to axion helioscopes and light-shining-through-walls experiments, green corresponds to high energy astrophysical bounds, blue for ultra-deep surveys. Figure courtesy of Ciaran O'Hare [72].

Supernovae can also be utilized to limit the axion coupling to standard model particles. The argument revolves around the duration of the neutrino signal after the supernova burst, as emission of new particles from the proto-neutron star core would compete with the standard model neutrino production. If the axion coupling to nucleons is too large, the core would cool too fast and the neutrino signal length would be shortened. The field of experimental axion physics is very active, as it can be seen in Fig. 3.4.

3.4 Domain walls

3.4.1 Properties

Let us consider a real scalar field ϕ with a potential $V(\phi)$ which has degenerate minima. Its Lagrangian will be

$$\mathcal{L} = \frac{1}{2}(\partial_\mu \phi)^2 - V(\phi). \tag{3.23}$$

The equations of motion can be obtained from

$$\partial_\mu \frac{\partial \mathcal{L}}{\partial\left(\partial_\mu \phi\right)} - \frac{\partial \mathcal{L}}{\partial \phi} = 0. \tag{3.24}$$

Let us consider a static domain wall solution orthogonal to the x axis $\phi(x)$. As it is a static solution of the equations of motion, for the above Lagrangian we find

$$\phi'' - \frac{\partial V}{\partial \phi} = 0 \qquad \Longrightarrow \qquad \frac{1}{2}\phi'^2 - V(\phi) = 0, \tag{3.25}$$

where the prime indicates derivative with respect to x. Let us calulate the energy momentum tensor of a domain wall solution. Its definition is

$$T_{\mu\nu} = \frac{\partial \mathcal{L}}{\partial\left(\partial^\mu \phi\right)} \partial_\nu \phi - g_{\mu\nu}\mathcal{L}. \tag{3.26}$$

We can substitute Eq. (3.23) and Eq. (3.25) to obtain

$$T_{\mu\nu} = \left(\partial_\mu \phi\right)\left(\partial_\nu \phi\right) - g_{\mu\nu}\mathcal{L} = -\delta_{\mu x}\delta_{\nu x}\phi'^2 + g_{\mu\nu}\phi'^2, \tag{3.27}$$

which, after raising one of the indices,

$$T^\mu_\nu = \phi'^2(x)\ \mathrm{diag}\left(1,0,1,1\right). \tag{3.28}$$

If we call the energy density ρ then it becomes

$$T^\mu_\nu = \rho\ \mathrm{diag}\left(1,0,1,1\right). \tag{3.29}$$

Something that must be noted from this expression is that it is independent of time and tangential coordinates, as well as invariant under Lorentz boosts in the tangential plane. This implies that only the transverse motion is observable. Even if it has nonzero tangential velocity its energy density does not change.

The surface energy density is equal to the wall tension in the tangential directions, which we notate with σ_{W}. The tension along the perpendicular direction is zero.

$$\sigma_{\mathrm{W}} = \int T^0_0\ \mathrm{d}x = \int T^2_2\ \mathrm{d}x = \int T^3_3\ \mathrm{d}x, \qquad \sigma_x = 0. \tag{3.30}$$

For a domain wall of thickness δ_{W},

$$\sigma_{\mathrm{W}} = \rho\delta_{\mathrm{W}}. \tag{3.31}$$

In general, the properties of topological defects are rather insensitive to the details of the underlying particle physics. This allows us to use simple models for their study and then, if necessary, complement this analysis with a few comments about more realistic cases. This motivates the study of a simple analytic solution, like the one for the double well potential Eq. (3.13). We had two parameters: λ, which is the quartic field coupling and η, the spontaneous symmetry breaking scale. The mass of the particles of that field is $m = \sqrt{\lambda}\eta$. In the analytic expression of the domain wall solution Eq. (3.14) we could see how it is mostly localized, with a thickness δ_{W} of about the inverse of its mass

$$\delta_{\mathrm{W}} \sim \left(\sqrt{\lambda}\eta\right)^{-1} \sim m^{-1}. \tag{3.32}$$

It is a static solution. Its total energy density is

$$\rho = \frac{1}{2}\left(\partial_x \phi\right)^2 \sim \lambda \eta^4. \tag{3.33}$$

If we calculate the wall tension we obtain

$$\sigma_{\mathrm{W}} = \int \phi'^2(x)\ \mathrm{d}x = \frac{2\sqrt{2}}{3}\sqrt{\lambda}\eta^3. \tag{3.34}$$

If we estimate the tension from the energy density as $\sigma_{\mathrm{W}} \sim \rho\delta_{\mathrm{W}} \sim \sqrt{\lambda}\eta^3$ we obtain qualitatively the same result. The tension can also be written in terms of the mass, $\sigma_{\mathrm{W}} \sim m\eta^2$. For a different potential, some order one numerical factors may appear on these expressions but otherwise we expect their properties to stay the same.

Ipser, Sikivie and Vilenkin were the first to solve the field equations of general relativity for a domain wall. They found that its gravitational potential is nonsingular and repulsive [80, 81]. Their result can be derived as well in the weak field approximation, where the physical intuition is less obscured by the algebra. Starting from the field equations of general relativity Eq. (2.10), we can do a weak stationary field expansion $g_{\mu\nu} = \eta_{\mu\nu} + h_{\mu\nu}(x^i),\ |h_{ij}| \ll |h_{00}|,\ |h_{00}| \ll 1$. After some calculations,

$$\nabla^2 \varphi(x) = 4\pi G (T^0_0 - \sum T^i_i), \tag{3.35}$$

where $\varphi(x)$ is the gravitational potential. In the case that the T^0_0 is the largest component of the stress-energy tensor, we recover Newton's law of gravitation, for which all potentials are attractive. If T^i_i is large, this need not be the case. For the stress-energy tensor of a planar static domain wall like Eq. (3.29) one obtains

$$\varphi''(x) = -4\pi G \rho, \tag{3.36}$$

which can be integrated to obtain

$$\varphi'(x) = -4\pi G \sigma_{\mathrm{W}}. \tag{3.37}$$

Although the numerical factors change with the wall shape, observers on either side of a domain wall accelerate as $\sim G\sigma_{\mathrm{W}}$. It is precisely the wall tension what determines how strong its gravitational repulsion will be.

3.4.2 Dynamics

Let us first discuss Z_2 walls. The initial shape of domain walls after the phase transition is determined by the random variation of the scalar VEV. Thus we expect walls to be very irregular, random surfaces. If a typical correlation length ξ can be defined in the system, then the typical curvature radius of the domain walls will be $R \sim \xi$. In general, the system is dominated by a few infinitely large domain walls of very complicated topology [76].

After formation, tension σ produces a force per unit area $f \sim \sigma/R$. Curved sections tend to straighten, exchanging their gradient energy for kinetic energy, reaching very large velocities. Depending on the model one can relax this mechanism, e.g. by introducing a damping force due to particle scattering, or enhance it, e.g. with a slight potential bias so that walls accelerate towards the true vacuum.

The total conformal area of domain walls decreases with time. If two domain walls collide they annihilate. Also, closed domain walls whose radius is smaller than the horizon $R \ll H^{-1}$ shrink due to wall tension and collapse. These processes lead to the production of ϕ particles, gravitational waves, or whatever particle is associated with fields coupled to ϕ.

During radiation- and matter-dominated universes, the horizon grows faster than the spacetime can expand. This is because $H \propto t^{-1}$ and thus the physical Hubble radius $H^{-1} \propto t$ while physical distances expand as $d \propto t^{1/2}$ and $d \propto t^{2/3}$ for radiation- and matter-dominated universes respectively. From the perspective of momentum space, this implies that larger modes continuously enter the horizon. Thus, in the evolution of the domain wall network there is an interplay between annihilation and growth of the horizon.

The consequence is that, after a few Hubble times have passed, the system reaches an attractor called the **scaling solution** [98, 99, 100, 103]. Each Hubble volume ends up with about one domain wall. In 3D, and up to order 1 numerical factors, we can estimate that the physical surface occupied by this domain wall will be approximately H^{-2} contained within one Hubble volume H^{-3}, resulting in the following energy density

$$\rho_{\mathrm{W}} \sim \frac{\sigma_{\mathrm{W}} H^{-2}}{H^{-3}} \sim \sigma_{\mathrm{W}} H. \tag{3.38}$$

The traditional explanation for why this state is reached is that domain walls reach relativistic velocities and annihilate up to causality, thus only about one wall per horizon can remain. In Sec. 4.3 we show how a scaling solution is also reached for walls formed after inflation (i.e. with scale invariant initial conditions) but that the amount of domain walls formed, as well as the amount present in the scaling solution is less than that of the white noise initial condition case.

Early works found that, for white noise initial conditions, the simulations deviated by some logarithmic factor from the scaling solution at late times [84] but this was shown to be a numerical artifact due to the limited dynamical range of the simulations [98, 105]. The case for scale invariant fluctuations is rather new and was not studied in detail up to our work. For scale invariant initial conditions the numerical artifacts are much larger. In Sec. 4.4 we present a systematic study of those numerical artifacts for the scale invariant initial condition case, showing that for the ideal case of an infinite simulation with infinite resolution the scaling solution should be preserved to great accuracy.

The dynamics of domain wall networks are highly nonlinear, so most results are based on what can be seen in numerical simulations. Analytical results rely on simplified models whose parameters are, in the end, fitted to simulation results. First developed for the study of cosmic strings [94, 95], the one-scale model aims to describe the macroscopic properties of the system through a characteristic scale (either the typical domain wall separation length or the correlation length) and the averaged domain wall velocity [101, 105, 108]. Although it is conceptually simple, we do not expect it to be applicable for all cases. For example, with scale invariant initial conditions, there is no typical correlation length (that is, there are correlations at all scales). In Sec. 4.3.3 we study the power spectrum of the field, which is closely related to the distances between domain walls, and in Sec. 4.5.2 we show a new model which can explain the main qualitative behaviour of the domain wall networks. I believe that the results discussed there are of great interest to researchers interested in their analytical modelling.

A well studied property of domain wall networks is their stability. It has been known that, under a small bias in the initial conditions, domain wall networks tend to collapse and disappear [89, 90, 91, 93, 96, 107, 109]. We found that this was no longer true in the scale invariant case. An in-depth analysis is presented in Ch. 5.

In the case of Z_N walls there are more than two degenerate vacua and we would expect the rise of cellular structures with linear junctions where several walls meet. Depending on the model, those junctions may or may not contain strings. Naively we could think that hexagonal equilibrium structures between multiple minima could be reached, where the whole network would freeze, however simulations show that their evolution is qualitatively similar to the Z_2 case, although less likely to decay when the number of vacua is increased [85]. Although the domain walls that may have been formed in our universe need not necessarily be Z_2, these results showing their similar dynamics greatly motivate the study of this simpler model. In the case of non-abelian walls, the energy dissipation rate is shown to be much smaller than in Z_N models and evidence for the formation of hexagonal equilibrium structures was found [87]. This is due to the large number of different types of wall junctions in the non abelian case.

3.4.3 Cosmological domain wall problem

Let us further analyze the cosmological impact of the energy density of a domain wall network Eq. (3.38). During the radiation dominated universe, $a \sim t^{1/2}$ and $H \sim a^{-2}$. Thus

$$\rho_{\mathrm{W}} \sim \sigma_{\mathrm{W}} a^{-2}. \tag{3.39}$$

Let us define its density parameter as

$$\Omega_{\mathrm{W}} \equiv \frac{\rho_{\mathrm{W}}}{\rho_{\mathrm{cr0}}}. \tag{3.40}$$

The a^{-2} dependence in Eq. (3.39) implies that Ω_{w} dilutes with the universe expansion at a slower rate than $\Omega_r \propto a^{-4}$ and $\Omega_m \propto a^{-3}$. Unless σ_{w} is sufficiently small, domain walls will dominate the energy contents of the universe, which is not what we observe. This was first pointed out by Zel'dovich, Kobzarev and Okun in 1974 and is called the cosmological domain wall problem [75].

We can make a naive estimate on the maximum value of σ_{w} in order to avoid domain wall domination. If we require $\Omega_{\mathrm{w}0} < 0.1$, then

$$\sigma_{\mathrm{w}} < (10\ \mathrm{MeV})^3 . \tag{3.41}$$

A more stringent constraint can be derived from the isotropy of the CMB. If we have about one domain wall per Hubble volume, then we can also estimate that the average separation between walls is $\sim H^{-1}$. We can integrate the derivative of the domain wall gravitational potential Eq. (3.37) along this typical distance to obtain the typical change of gravitational potential

$$\delta\varphi \sim G\sigma_{\mathrm{w}} H^{-1}. \tag{3.42}$$

This will induce density and CMB temperature fluctuations of a similar size

$$\delta\varphi \sim \frac{\delta\rho_m}{\rho_m} \sim \frac{\delta T}{T}. \tag{3.43}$$

The CMB temperature fluctuations are small, of around

$$\frac{\delta T}{T} \lesssim 10^{-5}, \tag{3.44}$$

which gives the following constraint on the tension

$$\sigma_{\mathrm{w}} < (1\ \mathrm{MeV})^3 . \tag{3.45}$$

This was the original estimation given by Zel'dovich et al on their original paper [75]. A similar bound can be obtained by considering the CMB distortions generated by domain-wall-induced metric perturbations (Sachs-Wolfe effect) [137]. The tension bound has been slightly improved by simulating the shape of the CMB anisotropies induced by domain wall networks [140, 141]

$$\sigma_{\mathrm{w}} < (0.92\ \mathrm{MeV})^3 . \tag{3.46}$$

Before modern theories of structure formation were developed, topological defect networks were an attractive feature as they were thought capable to act as seeds for structure formation. However, it was quickly seen that the density perturbations induced by domain walls were too small to account for the observable universe without leading to wall domination [83]. Thus, modern studies of topological defects as seeds for structure just focused on strings and textures [50]. Those were later excluded, since if they were abundant enough to cause gravitational collapse they would lead to a different shape of the CMB peaks than the one we currently observe.

3.4.4 Avoiding wall domination

If domain walls dominate the energy contents of the universe before the present time, it would lead to inhomogeneous expansion, with different Hubble patches expanding at different rates. Thus, cosmologists must build their models with some mechanism in mind to either make the domain wall network nondominant, make it decay before it becomes dominant, or avoid its formation altogether. Some of the proposed mechanisms are the following:

Domain wall formation before inflation. If the symmetry was broken before or during inflation, then the network is stretched far beyond the present Hubble radius and its energy density is diluted to a point in which it does not cause any cosmological problems. Even if the network is formed after inflation, if there is a second inflationary period the same result would happen.

Low enough tension. Even if a domain wall network is formed after inflation, as long as the domain wall tension is under the bound presented in Eq. (3.46), it does not represent a cosmological problem at the present time.

Symmetry nonrestoration. Symmetry restoration at high temperatures happens for a single scalar field [45] and is a general tendency for even more complex models. However, one can contrive models in which it does not happen. Particularly relevant for the topic of domain walls are some PQ models in which the scalar field has no gauge interactions and the PQ symmetry is not restored until energies of the order of the Planck mass [49, 92].

Trivial domain wall number. In the axion/dark matter context, domain walls form during a second phase transition after cosmic strings have already formed. Depending on the number of degenerate vacua, the domain wall number N_{DW} could be as low as one. In that case, only one domain wall attaches to each string and the string-wall network collapses immediately after the QCD phase transition [79]. The decay of the network could explain the observed dark matter density for certain values of f_a [106]. $N_{\mathrm{DW}} = 1$ is allowed in some axion models, notably the KSVZ model. One can achieve $N_{\mathrm{DW}} = 1$ through model building, for example if one associates the spontaneously broken discrete symmetry to a gauge symmetry, the physical degeneracy among different vacua is removed, as they become gauge equivalent. This is known as the Lazarides-Shafi mechanism [78]. Other models have also been built under similar principles [110].

Potential bias. If there exists a small potential bias, then the vacua are only approximately degenerate. The true vacuum will tend to grow while the false vacuum will tend to shrink. Let $\Delta\rho_v = \epsilon \neq 0$ be the difference between the energy density of both vacua. This induces a force per unit area on the walls $f_\epsilon \sim \epsilon$ which becomes dynamically important when it becomes comparable to the force induced by tension. As long as this happens before wall domination, domain walls will accelerate, annihilate with eachother and the network will collapse [82, 114, 115].

Population bias. If the probability distribution of the field values at the time of domain wall formation has a preference for one vacuum over another, that could lead to the decay of the network [89, 90]. The most common way to realize this bias is through cosmological inflation, for which fluctuations of light scalar fields develop at all scales. As we will show in Ch. 5, although the energy density of these networks is ~ 2 times lower than the energy density of networks generated thermally (i.e. white noise initial conditions), networks generated after inflation are very resilient to population biases.

Other scenarios. One can build a model with multiple scalar fields such that a spectator field induces a non-trivial scalar potential to the spontaneously broken field. This non-trivial potential can be such that string formation is not allowed and thus no string-wall network is formed [112]. In models with associated instantons, the instanton effects in the spontaneously broken scalar field can be such that the domain wall network decays [104, 111]. One can also consider models in which primordial black holes perforate the domain walls and destroy them [102].

We must keep in mind that, even if the domain wall network decays, that can lead to other problems like particle/axion overproduction or gravitational wave production after their annihilation [106]. Thus, a nondominant network that has not decayed yet is an appealing candidate to avoid the domain wall problem. In Ch. 6 we see how a stable domain wall network could explain the current hint for isotropic cosmic birefringence and predict anisotropic cosmic birefringence within the current experimental bounds.

3.4.5 Axionic domain walls

The bounds considered in Fig. 3.4 are for general QCD axions/ALPs without an associated domain wall network. In this thesis we are interested in axions with cosmologically viable domain wall networks, for which the axion-photon coupling and the mass region of interest can be seen in Fig. 3.5.

Large axion-photon couplings are excluded due to astrophysical observations. For example, the absence of an associated gamma-ray burst from the supernova SN1987A implies [66]

$$g_{a\gamma\gamma} \lesssim 5.3 \cdot 10^{-12}\mathrm{GeV}^{-1}, \tag{3.47}$$

although it has recently been suggested that this bound could be relaxed or even removed completely [70]. The absence of irregularities in the X-ray power-law spectrum of the radio galaxy M87 gives an even more stringent bound [69]

$$g_{a\gamma\gamma} \lesssim 2.6 \cdot 10^{-12}\mathrm{GeV}^{-1}. \tag{3.48}$$

In order for the domain wall network not to dominate the energy contents of the universe,

$$(1\ \mathrm{MeV})^3 > \sigma_{\mathrm{W}} \sim 8 m {f_a}^2 \sim 4 \cdot 10^{-5} m {g_{a\gamma\gamma}}^{-2}, \tag{3.49}$$

which implies that cosmologically viable axions with domain wall networks must be very light.

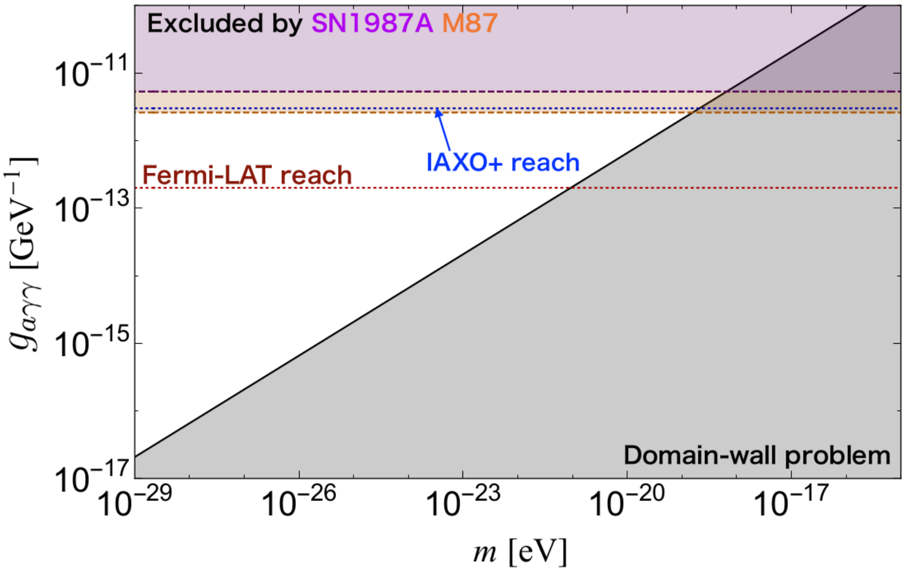

FIGURE 3.5: Various constraints on ultralight axions, with stable domain walls not bounded by strings, shaded regions are excluded. The purple and orange regions above the two horizontal dashed lines are excluded due to the SN1987A (upper) and M87 (lower) bounds, respectively. Also shown are the expected IAXO+ and Fermi-LAT reaches in the blue (upper) and red (lower) dotted lines. The lower right triangle (gray) region is excluded due to the domain wall problem. Figure from [147].

Chapter 4

Domain walls after inflation

Although domain wall network dynamics had been studied in the past literature, their dependence on the initial conditions has stayed unnoticed until now. In Sec. 4.1 we define the power spectrum of scalar fluctuations and see how it differs for a field which is in thermal equilibrium vs for a light scalar field after inflation. The network dynamics are highly nonlinear, so they are studied through simulations. Our computational setup is explained in Sec. 4.2. In Sec. 4.3 we will see how the dynamics of the network change when properly taking into account the inflationary fluctuations. Dynamical range effects in the network dynamics had been noticed previously but they become even more apparent for inflationary fluctuations. We describe them in Sec. 4.4. Finally, in Sec. 4.5 I will present an argument for why an attractor solution exists, and why it is different in the scale invariant initial condition case.

4.1 Initial conditions

The scale dependence of the fluctuations can be characterized by the power spectrum $P(k)$, which is defined as

$$\langle\phi(\mathbf{k})\phi(\mathbf{q})\rangle = (2\pi)^d\delta^{(d)}(\mathbf{k}+\mathbf{q})P(k), \tag{4.1}$$

where the angle brackets mean an ensemble average, d is the number of dimensions. $\phi(\mathbf{k})$ and $\phi(\mathbf{x})$ are the Fourier transforms of eachother

$$\phi(\mathbf{k}) = \int \mathrm{d}x^d \; e^{-i\mathbf{k}\cdot\mathbf{x}}\phi(\mathbf{x}), \tag{4.2}$$

$$\phi(\mathbf{x}) = \int \frac{\mathrm{d}k^d}{(2\pi)^d} \; e^{-i\mathbf{k}\cdot\mathbf{x}}\phi(\mathbf{k}). \tag{4.3}$$

Since the Lagrangian is invariant under spatial rotations, the power spectrum can be written just as a function of $k = |\mathbf{k}|$. If we substitute Eq. (4.3) twice into Eq. (4.1) and remember that

$$\int \mathrm{d}k^d \; \delta^{(d)}(\mathbf{k}+\mathbf{q})f(\mathbf{q}) = f(\mathbf{k}), \tag{4.4}$$

we obtain that the variance of fluctuations in position space can be expressed as

$$\langle \phi(\mathbf{x})^2 \rangle = \int \frac{\mathrm{d}k^d}{(2\pi)^d} \, P(k) = \int \mathrm{d}\ln k \; \mathcal{P}(k), \tag{4.5}$$

where we have introduced $\mathcal{P}(k)$, the reduced power spectrum. Its relationship with the power spectrum depends on the number of dimensions,

$$\mathcal{P}_{\mathrm{2D}}(k) = \frac{k^2 P(k)}{2\pi}, \qquad \mathcal{P}_{\mathrm{3D}}(k) = \frac{k^3 P(k)}{2\pi^2}. \tag{4.6}$$

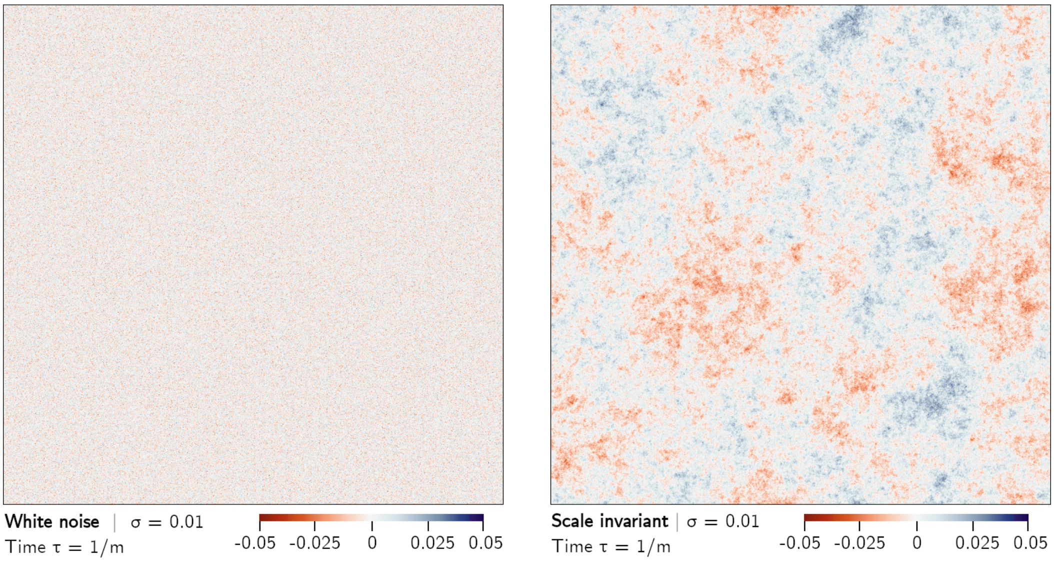

FIGURE 4.1: White noise (left) and scale invariant (right) initial field fluctuations ($\tau = 1/m$). The box contains 100^2 horizons. Both colorscale ranges are equal, and fluctuations have been set so that the position space variance is equal in both cases to $\sigma \approx 0.01$.

A field in thermal equilibrium develops Gaussian fluctuations in all of their degrees of freedom. Uncorrelated fluctuations are of the form

$$\langle \phi(\mathbf{x}) \phi(\mathbf{y}) \rangle = A \cdot \delta^{(d)}(\mathbf{x} - \mathbf{y}), \tag{4.7}$$

where A is a constant. This implies that the power spectrum is constant, and thus the reduced power spectrum in 2D is

$$\text{White noise:} \quad \mathcal{P}_{\mathrm{2D}}(k) = C_2 k^2, \tag{4.8}$$

where C_2 is a constant determining the size of fluctuations. Fluctuations of this type are what we call **white noise** or **thermal** fluctuations.

The spectrum of fluctuations acquired by a scalar field during inflation is very different. In the simplest case in which the Hubble parameter is constant during inflation, light quantum scalar fields develop fluctuations which are scale invariant

$$\text{Scale invariant:} \quad \mathcal{P}_{\mathrm{2D}}(k) = C_0 \qquad \text{constant}, \tag{4.9}$$

where C_0 is a constant determining the size of fluctuations. Please check Appendix A for the full derivation. These are what we call **scale invariant** or **inflationary** fluctuations.

In Fig. 4.1 we can see snapshots of some initial conditions for both cases. We can see how there are no apparent correlations in the white noise case, while for the scale invariant case we have large regions of either negative or positive field values.

4.2 Computational setup

Since domain wall networks are highly nonlinear systems, the amount of information that can be obtained analytically is very limited, so their dynamics are studied through computer simulations. Let us review how cosmological lattice simulations are set up.

Inflationary fluctuations are of quantum origin, but they become classical after horizon exit, which lets us solve the equations of motion classically. We are interested in the regime where domain walls do not dominate the energy contents of the universe. Although the role of backreaction in the context of matter inhomogeneities has been brought up recently [51], in the regime of cosmologically viable domain wall networks their backreaction should be negligible. Thus, their evolution can be solved as fluctuations over a homogeneous, expanding background.

The Lagrangian for a scalar field ϕ with a quartic potential is,

$$\mathcal{L} = \frac{1}{2}(\partial_\mu \phi)^2 - V(\phi), \qquad V(\phi) = \frac{\lambda}{4}(\phi^2 - \eta^2)^2, \tag{4.10}$$

where λ is the quartic coupling and η is the field VEV after the spontaneous symmetry breaking. Since Z_n walls behave similarly to Z_2 walls and the dynamics are not heavily dependent on the potential shape, we choose to use the double well potential for its simplicity. We consider domain walls without strings, for which a plausible generation mechanism is presented in [147]. The equation of motion of a scalar field in a homogeneous background is,

$$\ddot{\phi} + 3\frac{\dot{a}}{a}\dot{\phi} - \frac{1}{a^2}\nabla^2\phi + \frac{\mathrm{d}V(\phi)}{\mathrm{d}\phi} = 0. \tag{4.11}$$

Its derivation, as well as the details about how it is solved in the lattice, are shown in Appendix B.

In the program we need to use dimensionless variables, and it is convenient for those variables to be of order one so that floating point errors are minimized. In particular, the program time is dimensionless $\tau_{\mathrm{pr}} = m\tau$, where τ is conformal time. Conformal time (and in turn, program time) are not physical, we need to fix some normalization with respect to t in order to make sense of them as standalone variables. Conformal time is defined as $\mathrm{d}\tau = \mathrm{d}t/a(t)$. In the radiation dominated universe, $a(t) = a_i\sqrt{t/t_i}$ for some initial time t_i. After integration, this leads to two arbitrary constants, τ_0

and t_0,

$$\tau - \tau_0 = \frac{2t_i^{1/2}}{a_i}(t^{1/2} - {t_0}^{1/2}). \tag{4.12}$$

Both of them are set to zero. a_i must also be fixed in order to make both the scale factor and conformal time physical. It is convenient to set $a_{\rm osc} = a(t_{\rm osc}) \equiv 1$. The time at which the field starts rolling down the potential is $H(t_{\rm osc}) = m$ which, for radiation dominated era, $H = 1/(2t)$, gives $t_{\rm osc} = 1/2m$ and thus

$$a_{\rm osc} = a_i \left(\frac{t_{\rm osc}}{t_i}\right)^{1/2} = \frac{a_i}{(2mt_i)^{1/2}} \equiv 1 \qquad \Longrightarrow \qquad a_i = (2mt_i)^{1/2}. \tag{4.13}$$

This fixes the normalization of τ. In this and the next chapters, conformal times are given in units of $1/m$.

In this system we can identify two important scales—the horizon scale and the domain wall width. Simulations are often performed in comoving coordinates with a special normalization. In order to correctly solve the system, the box size needs to be large enough to contain at least a few horizons and the resolution needs to be fine enough so that there are at least a few cells per domain wall width. However, during the radiation dominated era, in comoving coordinates the domain wall width $\delta_{\rm W}$ decreases in proportion to a^{-1} and the comoving horizon size R_{H0} increases in proportion to a. Thus, the dynamical range at the beginning of the simulation must be good enough to solve the evolution of the system for enough time until the scaling solution is reached.

This is computationally challenging, and particularly during the early stages of research these simulations could not be performed. The first simulation results were published in 1989 by Press, Ryden and Spergel, and the trick they used to resolve the system with limited computational power was making the comoving domain wall width constant in time after domain wall formation. The domain wall evolution was reported to be mostly unaffected by this change, but other aspects like gravitational wave production or possible small scale structure can not be probed with the Press-Ryden-Spergel setup. Thus, it is preferable to solve the equation of motion as it is, without making any a priori assumptions of what does or does not affect the domain wall dynamics.

From Eq. (3.29) we can see how the energy momentum tensor of a domain wall is invariant under Lorentz boosts in the tangential plane, which implies that only the transverse motion of the domain wall is observable. This motivates a setup in which the field is homogeneous over one of the coordinates, and then solving the 3D equation of motion on a 2D slice. This lets us run faster simulations of higher dynamical range, and then just gain more statistics by running multiple simulations and averaging the results.

Modern computers have hardware capable of running multiple tasks at the same time, which can be used to parallelize code. In our case, its appeal is that the equation of motion can be solved faster without any approximations, which in turn implies that the dynamical range can be improved at no time expense. Some researchers [160, 161, 162] have pioneered the techniques of GPU acceleration in the context of cosmological lattice simulations, which depending on the computer can reduce simulation times one or two orders of magnitude. Compared to past GPU accelerated code architectures, mine improves the memory usage and reduces the time each simulation takes. For more information about its implementation, see Appendix C.

The simulation size N_{cell} is determined by the amount of field values taken for each side of the discretized field matrix (box). N_H is the number of horizons per side of the box, which is changes with time. N_H/N_{cell} at initial time determines the resolution of the simulation. The simulation size, initial number of horizons and number of repetitions chosen for each result in this thesis varies, as a compromise between time, dynamical range and good statistics has to be reached. Traditionally, only powers of two were chosen for N_{cell} (e.g. 4096 or 8192) since those were the fastest matrix sizes to run a FFT algorithm on. However, modern FFT libraries are very fast on any matrix size. Some of the 2D results on this thesis are for a 31104^2 matrix, and in 3D, for 960^3, as those are the largest simulation sizes which I can run with my code architecture on my 8 GB DRAM GPU. The details of the simulation size and resolution are specified on each result as they are presented.

4.3 DWs from scale invariant fluctuations

In order to more easily understand what happens in the case of scale invariant initial conditions, it is useful to see the results in contrast to the white noise ones.

4.3.1 Visualizing the network formation

Let us first visualize how the networks look like. The simulation starts at $\tau_{\text{osc}} = 1/m$, and at around $\tau_{\text{form}} = 5/m$, the network has fully formed. At time $\tau = 10/m$, enough time has passed for the network to stabilize at the attractor solution.

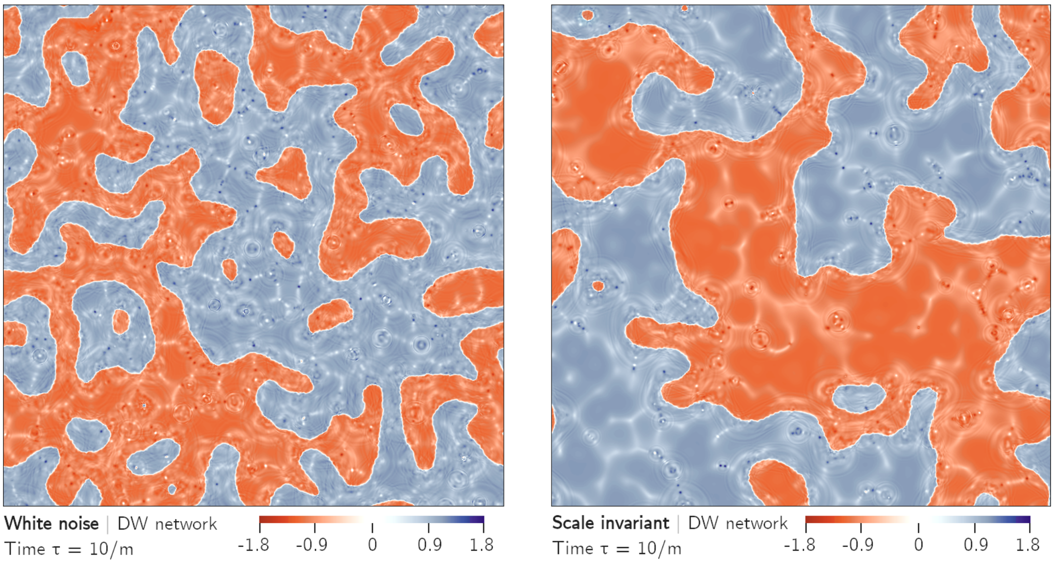

FIGURE 4.2: Field snapshots at time $\tau = 10/m$ for white noise (left) and scale invariant (right) initial conditions. The box contains 10^2 horizons.

The initial conditions shown in Fig. 4.1 are left to evolve, and the resulting domain wall network is shown at Fig. 4.2. Since the horizon size increases as $\propto \tau$ in comoving coordinates, the box now contains 10^2 horizons. In the scale invariant case, the domain wall network becomes more sparce, with the superhorizon correlations turning into relatively straight domain wall segments spanning multiple Hubble radii and voids occupying several Hubble volumes.

4.3.2 Length per horizon

There are many magnitudes one can compute in order to characterize the behaviour of the system. For example, the average domain wall velocity, kinetic, potential or gradient energies... One magnitude which is both fast to compute and easy to interpret is the normalized domain wall length per Hubble volume. Since this is a magnitude which we will make extensive use of, for convenience, let us do a slight abuse of notation and call it L, instead of something along the lines of L/H^{-1}. In 2D, this magnitude can be computed by

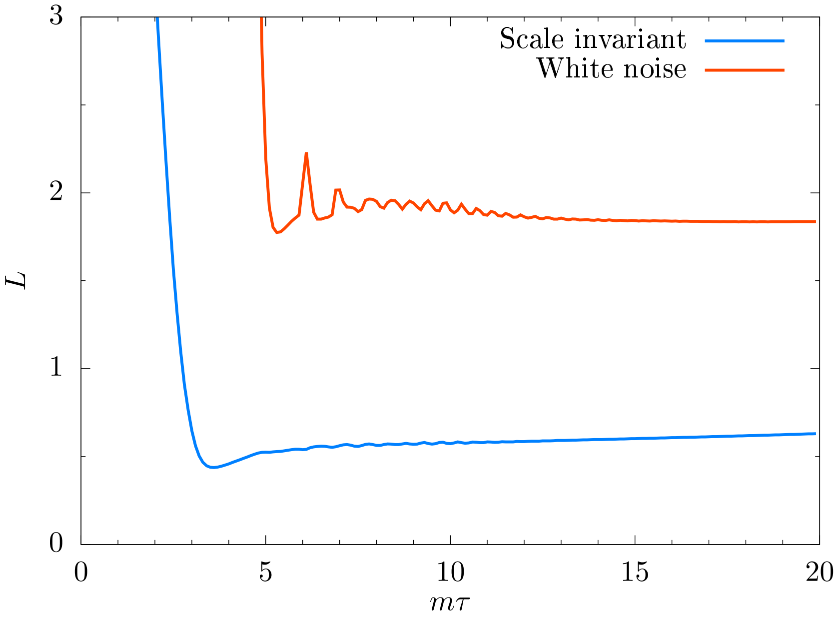

FIGURE 4.3: Time evolution of the normalized domain wall length L for scale invariant (blue) and white noise (orange) initial conditions. For large $m\tau$, L asymptotes to a certain value, which is interpreted as the system reaching an attractor solution. Data from 31104^2 simulations, 1600^2 (400^2) horizons at initial time and 70 (10) averages for scale invariant (white noise) initial conditions.

$$L = \frac{\text{Total physical DW length}}{{N_H}^2 H^{-1}}. \tag{4.14}$$

This is a dimensionless quantity—if the total domain wall length on the numerator is comoving (physical), then the Hubble radius on the denominator must be comoving (physical) as well. The normalized domain wall length quantifies how many domain walls there are within a Hubble volume, and thus for the scaling solution we expect this to be of order 1.

In Fig. 4.3 we can see how L evolves with time for both kinds of initial conditions. As $m\tau$ becomes large, L asymptotes to a constant value, which we will call L_{attr}. This is a convenient aspect of L, just by visual inspection we can see whether the system has reached the scaling solution or not.

The way in how the domain wall length is calculated is by computing how many contiguous cells have field values of opposite sign and then multiplying that by an appropiate factor. Before the domain wall is fully formed, this calculation does not make physical sense, which is why L takes very large values at early times. We can also see some small bumps at values of $\tau \sim 8/m$, which correspond to large scalar fluctuations at small scales. Those are the ripples between the domain walls which can also be seen in Fig. 4.2. The initial spectrum of fluctuations can be set with suppressed small scale correlations (an UV cut in momentum space) so that these high frequency modes are not introduced into the system, and thus we do not need to wait for them to decay. The large time behaviour of the system does not seem to change significatively even if an initial UV cut is applied.

4.3.3 Field power spectrum

We can calculate the field power spectrum as defined in Eq. (4.6) after the domain wall formation to see how the field correlations evolved with time.

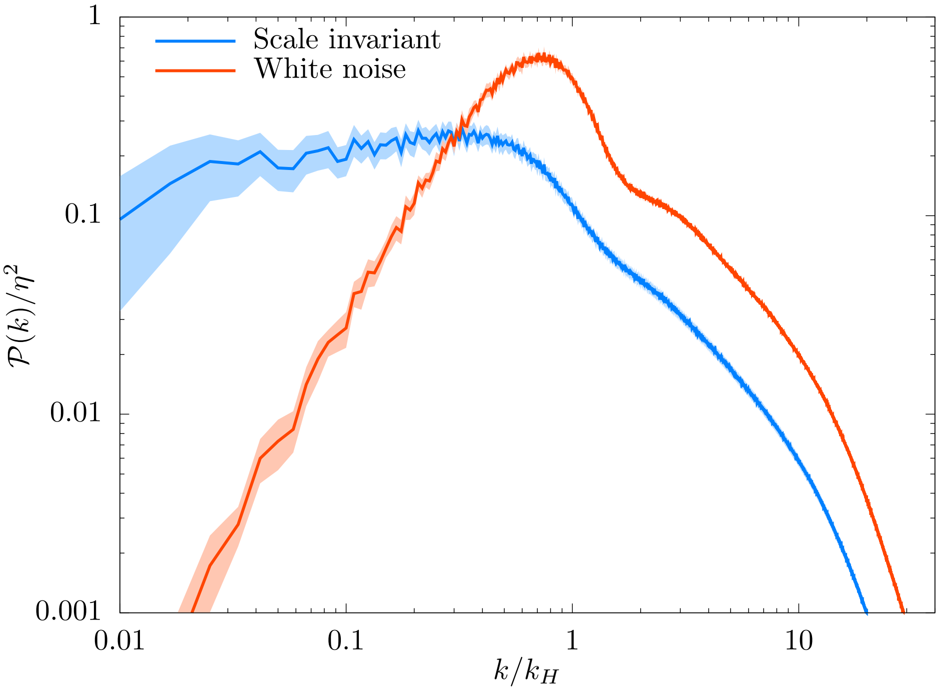

FIGURE 4.4: Reduced power spectrum $\mathcal{P}(k)$ normalized by the VEV squared η^2 evaluated at time $\tau = 10/m$ for both scale invariant (blue) and white noise (orange) initial conditions. Data from 31104^2 simulations of 1200^2 horizons in size. 100 (30) averages taken for the scale invariant (white noise) case, the shaded regions are 1σ confidence intervals from this average.

In Fig. 4.4 we can see the reduced power spectrum at $\tau = 10/m$ for both scale invariant and white noise cases. Wavenumbers k are normalized by the one corresponding to the horizon size k_H, as defined in Eq. (2.21), in order to easily identify which k are sub-horizon (small scales, $k/k_H > 1$) or super-horizon (large scales, $k/k_H < 1$). The wavenumber associated with domain wall width in our simulation at that time is $k/k_H \sim 16$, for which we can see a drop in the slope of the power spectrum, indicating that there is no small scale within the domain walls. The horizon scale is $k/k_H = 1$, and the value of the reduced power spectrum there is correlated to the amount of domain walls at the attractor solution L_{attr}.

During domain wall formation (from τ_{osc} to τ_{form}), large scale fluctuations grow in size. This is because due to these large scale correlations nearby field values will be either mostly positive or mostly negative, and as the field rolls down the potential it will do so coherently. One would, naively, expect the increase of values of $\mathcal{P}(k)$ from τ_{osc} to τ_{form} to be in such a way that causality protects the shape of the power spectrum at superhorizon scales. That is, if the initial power spectrum was scale invariant at the initial time, to still be scale invariant at superhorizon scales after domain wall formation. In other words, we would naively expect the scalar field dynamics to be able to access small scale correlations (i.e. to form domain walls) but not to generate nor suppress correlations at scales larger than the horizon.

In Fig. 4.4 we can see how the reduced power spectrum at superhorizon scales for white noise is still approximately $\propto k^2$, but for the scale invariant case it is visibly not constant. Surprisingly, the shape of the reduced power spectrum has developed a slight tilt with time. We argue that the reason for this tilt is that, although the power spectrum takes a simple form in momentum space, the evolution of each individual k is not decoupled. The scalar field evolution is happening in the position space, where fluctuations of all sizes stack up, and thus the aforementioned "coherence" when rolling down the potential is not the same for all scales.

Let us estimate the increase of the values of the reduced power spectrum from the initial time of oscillation τ_{osc} to the time of domain wall formation τ_{form} like

$$\mathcal{P}_{\mathrm{form}}(k_R) \simeq \mathcal{P}_{\mathrm{osc}}(k_R) \cdot \frac{\langle \phi^2(x) \rangle_R^{\mathrm{form}}}{\langle \phi^2(x) \rangle_R^{\mathrm{osc}}}, \tag{4.15}$$

where $\mathcal{P}_{\mathrm{osc}}(k) = C_0 \ \forall k$ is the initial scale invariant reduced power spectrum, and $\langle \phi^2(x) \rangle_R$ is the position space field fluctuation variance averaged over a spatial region of size R. Let us not get confused by this notation, (x) is the variable averaged over, and $\langle \phi^2(x) \rangle_R$ is in essence a function of a wavenumber $k_R = 2\pi/R$.

We can estimate that $\langle \phi^2(x) \rangle_R^{\mathrm{form}} \simeq \eta^2$ since, after domain wall formation, the field will fall to either minima and thus the field variance will be approximately the VEV squared. For $\langle \phi^2(x) \rangle_R^{\mathrm{osc}}$ we need to be a bit more careful. In order to avoid discussions about the small scale fluctuations, which are of no interest to this effect, let us compute this as its difference with respect to its value over a Hubble volume. Then, for $R > H^{-1}$, $\mathcal{P}_{\mathrm{osc}}(k) = C_0$,

$$\left\langle \phi^2(x) \right\rangle_R^{\mathrm{osc}} - \left\langle \phi^2(x) \right\rangle_{H^{-1}}^{\mathrm{osc}} = \int_{k_R}^{k_H} \mathrm{d} \ln k \ \mathcal{P}(k) = C_0 \ln k_H/k_R \ > \ 0, \tag{4.16}$$

where $\langle \phi^2(x) \rangle_{H^{-1}}^{\mathrm{osc}}$ is some finite value. This implies that, even though the power spectrum is scale invariant, the real space fluctuation variance is larger on superhorizon scales compared to that at horizon scales, with a logarithmic dependence on the scale. After domain walls have formed, the reduced power spectrum becomes

$$\mathcal{P}_{\text{form}}(k_R) \simeq C_0 \cdot \frac{\eta^2}{\langle \phi^2(x) \rangle^{\text{osc}}_{H^{-1}} + C_0 \ln k_H/k_R}, \tag{4.17}$$

which depends on k.

The scale invariant power spectrum is quite peculiar, namely because the real space fluctuation variance tends to infinity for any nonzero C_0 and no maximum nor minimum momentum,

$$\left\langle \phi^2(x) \right\rangle = \int_{k_{\min}}^{k_{\max}} \mathrm{d}\ln k \; C_0 = C_0 \ln k_{\max}/k_{\min} \xrightarrow[k_{\min}\to 0]{k_{\max}\to\infty} \infty. \tag{4.18}$$

This *could* be problematic for the above argument—either we set a maximum and minimum k, or otherwise C_0 is ill-defined. In realistic scenarios there is a maximal scale for which the fluctuations are scale invariant, related to the number of e-folds of inflation, and small scale fluctuations are not scale invariant but rather $\propto k^{-2}$. In any case, Eq. (4.17) can also be obtained for a reduced power spectrum of the form

$$\mathcal{P}_{\text{osc}}(k) = C_\epsilon k^\epsilon, \quad |\epsilon| \ll 1, \tag{4.19}$$

for which we would obtain

$$\begin{aligned} \left\langle \phi^2(x) \right\rangle^{\text{osc}}_R - \left\langle \phi^2(x) \right\rangle^{\text{osc}}_{H^{-1}} &= \int_{k_R}^{k_H} \mathrm{d}\ln k \; C_\epsilon k^\epsilon = \frac{-C_\epsilon}{1-\epsilon}\left({k_H}^\epsilon - {k_R}^\epsilon\right) \\ = \frac{-C_\epsilon}{1-\epsilon}\,{k_H}^\epsilon \left[1 - \left(\frac{k_R}{k_H}\right)^\epsilon\right] &\xrightarrow{|\epsilon|\ll 1} \left(\epsilon C_\epsilon\right) \ln \frac{k_H}{k_R} \; \left(1 + \mathcal{O}(\epsilon)\right). \end{aligned} \tag{4.20}$$

If we then make ϵ tend to zero and define $C_0 \equiv \epsilon C_\epsilon$ it would be like doing the calculation for the scale invariant spectrum in a regularized form. If not, then Eq. (4.20) shows that even with a slight blue or red tilt on the initial power spectrum, after domain wall formation, the reduced power spectrum shape at superhorizon scales after domain wall formation is still modified logarithmically on k.

4.3.4 3D simulations

Up until now, all results had been shown for 2D simulations. This is because we are limited by memory size, and thus we can reach better dynamical range by taking large 2D simulations and then many averages, rather than just one 3D simulation. However, we want to know if the features and dynamics found in 2D simulations are indeed similar to those in 3D simulations.

In Fig. 4.5 we can see the reduced power spectrum along constant z slices, one per horizon in the z axis, for 3D simulations. We can see that, although the dynamical range is worse and thus we cannot probe scales as large nor small as in Fig. 4.4, the general features are remarkably similar to those seen in 2D simulations.

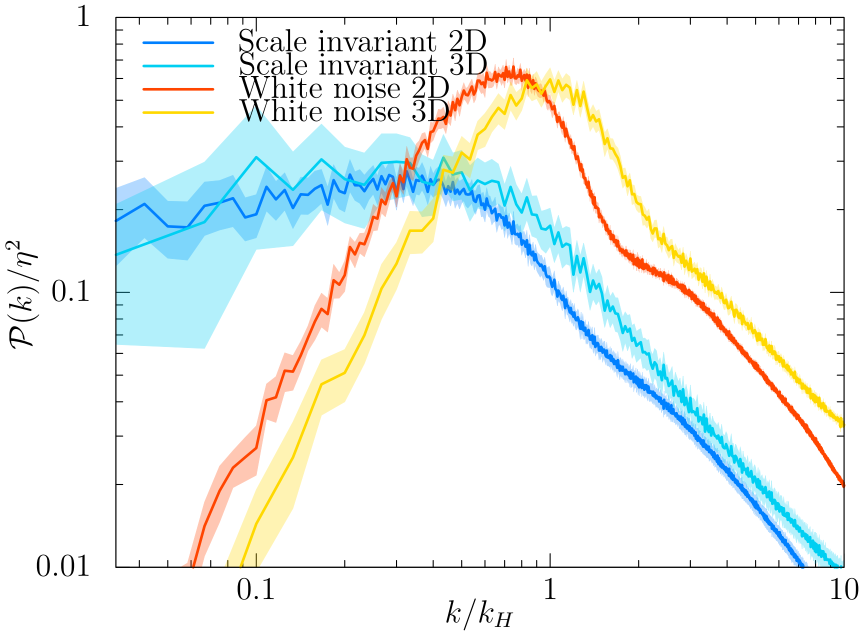

FIGURE 4.5: Reduced power spectrum $\mathcal{P}(k)$ normalized by the VEV squared η^2 in 3D simulations at time $\tau = 10/m$. Computed along constant z slices, one per horizon in the z axis, for both scale invariant (skyblue) and white noise (yellow) initial conditions. Simulations are 960^3, with 300^3 horizons at initial time. One slice per horizon in the z direction was taken and the results averaged over 5 simulations, the shaded regions are 1σ confidence intervals from this average. For reference, the reduced power spectrum for 2D, 31104^2 simulations of 1200^2 horizons at initial time, with scale invariant (blue) and white noise (orange) initial conditions are also shown.

4.4 Deviations from the scaling solution

Some early papers [84, 93, 96, 97, 98] found some late time deviations from the scaling solution in the case of white noise initial conditions. However, it was later seen [99] that it was due to the limited dynamical range of the simulations, and not a physical effect. The smallest wavelength that the simulation can resolve is the side of one individual cell N_H/N_{cell}, which corresponds to

$$\frac{k_{\text{max}}}{k_H} = \frac{2\pi N_{\text{cell}}}{N_H}, \tag{4.21}$$

while the largest wavelength that can appear in the simulation corresponds to the diagonal of the box $\sqrt{2}N_H$, for which

$$\frac{k_{\text{min}}}{k_H} = \frac{\sqrt{2}\pi}{N_H}. \tag{4.22}$$

In Fig. 4.3 we can see a slight increase for the normalized length $\Delta L/\Delta m\tau$ even in a simulation with a dynamical range large enough not to induce noticeable deviations from the scaling solution in white noise initial condition simulations. In order to study if this is a physical effect or not, we performed several simulations with different box sizes and measured the increase in each of them. One plausible hypothesis for this increase was the existence of some winding mode, that is, the periodic boundary conditions were allowing field fluctuations to wind along the box, which could induce an increase of the normalized domain wall length L with time. In order to check that hypothesis, large simulations with an initial IR cut on the initial conditions (i.e. the initial reduced power spectrum was set to zero for all $k \leq k_{\mathrm{min}}$) were also performed, and the increase of L with time, measured.

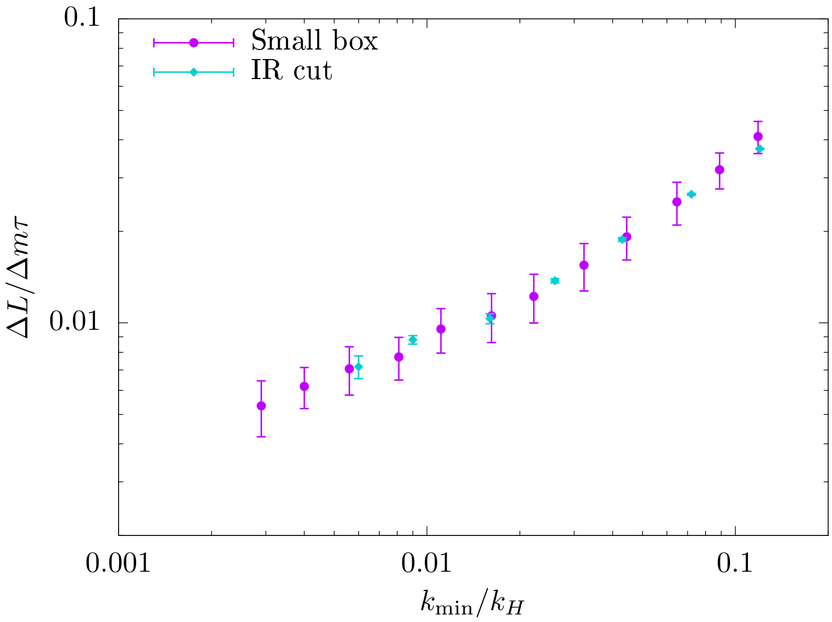

FIGURE 4.6: Linear increase of the normalized length L with time $m\tau$ for simulations of constant resolution ($N_H/N_{\mathrm{cell}} = 0.051$ at initial time) but different size (in purple), and for simulations of constant size (31104^2, 1600^2 horizons, resolution $N_H/N_{\mathrm{cell}} = 0.051$) but with various IR cuts (in blue).

The results can be seen in Fig. 4.6. When the increase $\Delta L/\Delta m\tau$ is plotted over k_{min}/k_H both results agree, suggesting that the problem is not the existence of winding modes, but rather that the maximum correlation length is limited at the initial time by the simulation size.

The k_{min} dependence in Fig. 4.6 is not perfectly linear in the log-log plot. Looking at the data, it looks like even as k_{min} tends to zero, $\Delta L/\Delta m\tau$ still has a nonzero value. Let us divide the length increase into two different components,

$$\frac{\Delta L}{\Delta m\tau} = \left[\frac{\Delta L}{\Delta m\tau}\right]_{\mathrm{IR}} + \left[\frac{\Delta L}{\Delta m\tau}\right]_{\mathrm{UV}}, \tag{4.23}$$

where $[\Delta L/\Delta m\tau]_{\mathrm{IR}}$ is the length increase due to the presence of a k_{min} in the initial power spectrum, and $[\Delta L/\Delta m\tau]_{\mathrm{UV}}$ is the length increase due to the discretization of the lattice. Let us suppose that $[\Delta L/\Delta m\tau]_{\mathrm{IR}}$ has a power law dependence with k_{min} and thus separate both contributions by doing a nonlinear regression to

$$\frac{\Delta L}{\Delta m\tau} = A\left(\frac{k_{\mathrm{min}}}{k_H}\right)^B + \left[\frac{\Delta L}{\Delta m\tau}\right]_{\mathrm{UV}}, \tag{4.24}$$

where A, B and $[\Delta L/\Delta m\tau]_{\mathrm{UV}}$ are the regression coefficients. This is done for several simulation sets with different IR cuts and resolutions.

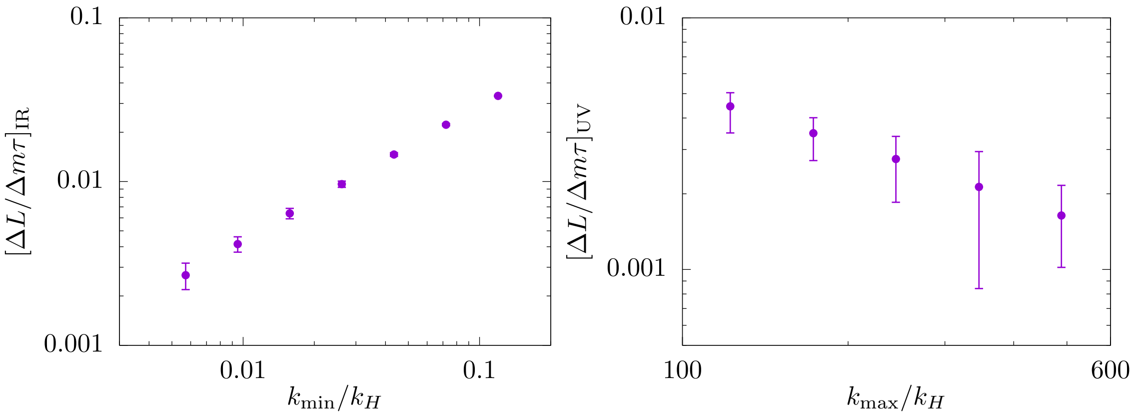

FIGURE 4.7: Contributions to the linear increase of the normalized length with time $\Delta L/\Delta m\tau$ corresponding to a $k_{\min}$ on the initial power spectrum (left) and to a limited UV resolution (right). Both contributions are separated through a nonlinear fit to Eq. (4.24). The values of $\Delta L/\Delta m\tau$ come from 31104^2 simulations × 30 repetitions for each individual IR cut and resolution.

The results can be seen in Fig. 4.7. They suggest that as the dynamical range gets better, the normalized length truly asymptotes to a constant value.

The reason why $[\Delta L/\Delta m\tau]_{\mathrm{IR}}$ is more noticeable in the case of scale invariant initial conditions is because fluctuations at superhorizon scales are larger. With white noise initial conditions, even if a $k_{\min}$ exists, the correlations larger than the box size are of smaller magnitude than for the scale invariant case. Notice that $[\Delta L/\Delta m\tau]_{\mathrm{UV}}$ is about one order of magnitude smaller than $[\Delta L/\Delta m\tau]_{\mathrm{IR}}$. This is to be expected: as long as there are several field values per domain wall width, which is the smallest scale in the system, the system should be being mostly correctly solved for.

4.5 Existence of an attractor solution

The existence of an attractor solution has remained solely as a phenomenological truth in the study of domain walls. It was shown to exist for the one-scale model [101], but we do not expect this model to remain valid for scale invariant conditions as no characteristic scale can be properly defined. In this section I will present how, for a certain generalized set of initial conditions, simulations show that an attractor solution exists. We also found for which kinds of initial conditions the attractor solution is not reached. The qualitative behaviour of the system can be derived from a phenomenological model, which is developed in Sec. 4.5.2.

4.5.1 Generalized initial conditions

Let us consider an initial reduced power spectrum of the form

$$\mathcal{P}(k) = C_n k^n, \tag{4.25}$$

where C_n is a constant coefficient that depends on the power n but not on k. The case $n = 0$ corresponds to scale invariant initial conditions and $n = 2$ to white noise. We are interested in the case in which the position space fluctuations are constant in n. If we substitute Eq. (4.25) into Eq. (4.5) and set the position space field standard deviation σ to be constant, we get

$$C_n = \begin{cases} \dfrac{\sigma^2 n}{{k_{\text{max}}}^n - {k_{\text{min}}}^n}, & n \neq 0 \\ \dfrac{\sigma^2}{\ln\left(k_{\text{max}}/k_{\text{min}}\right)}, & n = 0 \end{cases} \tag{4.26}$$

where k_{max} and k_{min} depend on the size and resolution of the simulation. Their values can be obtained from Eq. (4.21) and Eq. (4.22) respectively. Integrating up to an unique k_{min} is not exactly true: all modes of wavelength N_H (side of the box) fit in the simulation but only some with $\sqrt{2}N_H$ (diagonal of the box) do so. There is no need to worry too much about this, this integration is only realized to set C_n in the code so that σ is constant and the results for different n can be easily compared, but even if σ has a slight dependence on n the results remain mostly unchanged.

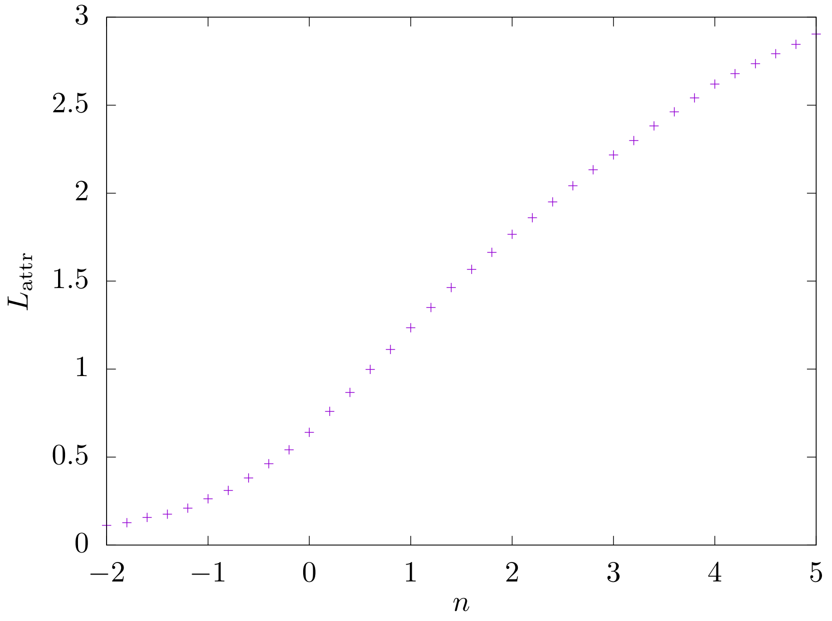

FIGURE 4.8: Value of the normalized domain wall length at the attractor solution L_{attr} as a function of n. L_{attr} is estimated as the minimum value of L after domain wall formation at $\tau_{\text{form}} \approx 6/m$. From a set of 2D, 4096^2 simulations with 300^2 horizons at the starting time, 50 averages per value of n.

What we saw in the simulations is that all of these initial conditions led to an attractor solution, with the amount of domain walls in it depending on the particular value of n, as one can see in Fig. 4.8. A slight increase in L over $m\tau$ is observed for most values of n, although from the study presented in Sec. 4.4 for $n = 0$ we believe that this is not physical and that an attractor solution exists for this set of initial conditions.

The fact that an attractor solution is found for such a wide range of initial conditions raises the following question: when is an attractor solution not reached? The fact that L increased when an IR cut is introduced in the initial conditions gives us an important clue. If one can define a characteristic wavenumber at superhorizon scales k_c from the power spectrum alone, then k_c/k_H will evolve with time, and the system will not reach an attractor solution until this mode enters the horizon and the fluctuation size at superhorizon scales becomes constant with time. In this case, the initial power spectrum has the following form

$$\mathcal{P}(k) = \begin{cases} C_0, & k > k_{\text{cut}} \\ 0, & k < k_{\text{cut}}. \end{cases} \tag{4.27}$$

Here, k_{cut}/k_H changes with time and the fluctuation size at superhorizon scale also changes with time, which causes the domain wall length to grow. That can be understood from Fig. 4.8: the attractor length for $n = 0$ is smaller than the one for $n > 0$, so as the fluctuations at superhorizon scale become less and less correlated, L grows.

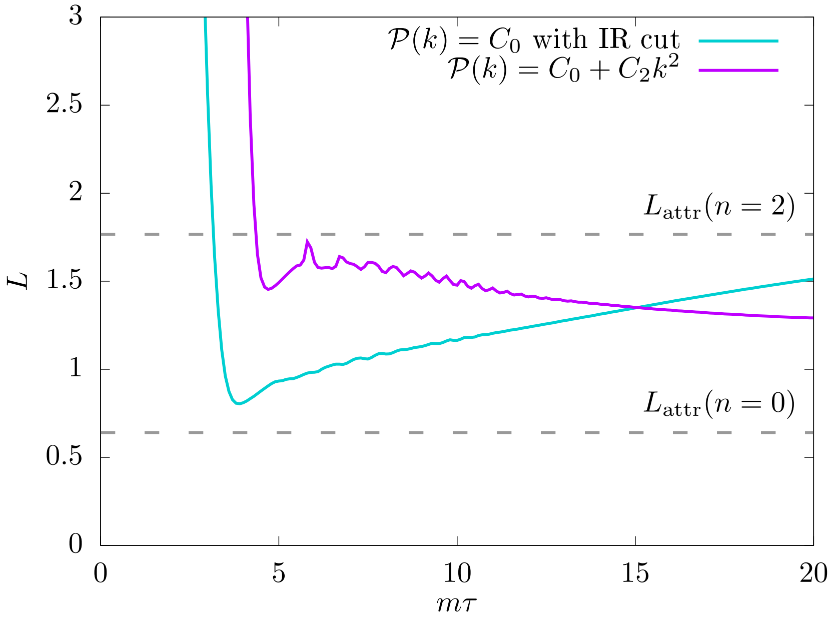

FIGURE 4.9: Normalized domain wall length L for two different power spectrums with time dependent superhorizon fluctuations. In blue, $\mathcal{P}(k) = C_0$ with an infrared cutoff at $k_{\text{cut}}/k_H = 0.12$ at initial time. In purple, $\mathcal{P}(k) = C_0 + C_2k^2$ with a characteristic scale Eq. (4.29) with values such that $k_{02}/k_H = 1/7$ at initial time. Data from 16384^2 simulations, 800^2 horizons at initial time, 50 averages. The attractor values L_{attr} for white noise and scale invariant initial conditions are shown in dashed lines.

We can also contrive some initial conditions so that L decreases with time. For example, let us consider a power spectrum of the form

$$\mathcal{P}(k) = C_0 + C_2k^2. \tag{4.28}$$

Here we can define a characteristic scale k_{02}, the wavenumber at which both terms are comparable in size

$$k_{02} = \sqrt{\frac{C_0}{C_2}}. \tag{4.29}$$

If $k_{02}/k_H \gg 1$, then the domain walls form mostly under Gaussian fluctuations, and as $k_{02}/k_H \sim 1$, the superhorizon fluctuations will be mostly scale invariant, which will make the domain wall network decay until it reaches the $n = 0$ attractor. In Fig. 4.9 we can see how that is indeed the case.

4.5.2 Phenomenological model

The qualitative behaviour of this system can be seen with a simple phenomenological model. Our objective now is to build a differential equation in which the three main dynamics of the system (expanding universe, domain wall annihilation, superhorizon fluctuations) are taken into account.

Let us define L in three dimensional space as

$$L = \frac{\text{Total physical DW surface}}{{N_H}^3 \cdot H^{-2}}. \tag{4.30}$$

This is a dimensionless quantity. We want to know how L changes with time for a static domain wall network. That is, a network where the scalar field dynamics have been switched off and is just following the universe expansion. The total physical DW surface and the amount of Hubble horizons ${N_H}^3$ have to be both evaluated over the same volume. Both in the simulations and in the following argument, that is a box of fixed comoving size.

In radiation dominated era, $H \propto \tau^{-2}$ and $a \propto \tau$. The box size is constant in comoving coordinates, but evolves $\propto a$ in physical coordinates. Thus, the number of horizons on one side of the box evolves as $N_H \propto a/H^{-1} \propto \tau^{-1}$. The total comoving DW hypersurface is constant, and thus the total physical DW surface evolves as $\propto a^2 \propto \tau^2$. Putting everything together, L will evolve as

$$L(\tau) \propto \tau. \tag{4.31}$$

When differentiating with respect to τ, results in the following,

$$\frac{\partial L}{\partial \tau} = \frac{L}{\tau}. \tag{4.32}$$

Now, in order to estimate the annihilation probability, imagine placing N straight lines randomly on a plane. If none are parallel, they will intersect $N(N-1)/2$ times, which motivates the inclusion of a term of the form $L(L - L_{\text{attr}})/\tau_{\text{ann}}$ in the above equation,

$$\frac{\partial L}{\partial \tau} = \frac{L}{\tau} - \frac{L^2}{\tau_{\text{ann}}} + L_{\text{attr}} \frac{L}{\tau_{\text{ann}}}. \tag{4.33}$$

Intuitively, it makes sense for the annihilation term to go as L^2 since they annihilate in pairs, as well as to have a linear correction to it. The solution to this differential equation is

$$L(\tau) = \frac{L_{\text{attr}}}{1 + c_1 L_{\text{attr}} \exp(-L_{\text{attr}}\tau/\tau_{\text{ann}})\tau^{-1} + \mathcal{O}\left((L_{\text{attr}}\tau/\tau_{\text{ann}})^{-1}\right)}, \tag{4.34}$$

where c_1 is an integration constant which can be identified with the initial conditions of the system. All of the time-dependent terms decay with time, and we see how for $\tau \gg \tau_{\text{ann}}$, this solution tends to a constant value.

$$L(\tau \gg \tau_{\text{ann}}) = L_{\text{attr}}. \tag{4.35}$$

Fluctuations at the superhorizon scale only affect the domain wall network evolution through a localized bias which varies randomly for each Hubble sphere and in time $\delta(x, \tau)$. As we will see in Ch. 5, an overall bias induces an exponential decay of L such as

$$L(\tau) \sim \exp(-\tau/\tau_L) \tag{4.36}$$

where τ_L is a characteristic lifetime that depends on the bias. The particulars of the dependence of the lifetime with the bias δ are discussed in Sec. 5.1.4 but most important for us is that the dependence is not linear. The above ODE is written in terms of spatially averaged quantities. Even though the spatial average of the bias is zero $\langle\delta\rangle = 0$ the spatial average of the lifetime will not be zero $\langle\tau_L\rangle \neq 0$. This motivates the inclusion of a term like $-L/\tau_L$. The full ODE then becomes

$$\frac{\partial L}{\partial \tau} = \frac{L}{\tau} - \frac{L^2}{\tau_{\text{ann}}} + \frac{L}{\tau_{\text{ann}}}\left(L_{\text{attr}} - \frac{\tau_{\text{ann}}}{\tau_L}\right), \tag{4.37}$$

which at large τ tends to

$$L(\tau \gg \tau_{\text{ann}}) = L_{\text{attr}} - \frac{\tau_{\text{ann}}}{\tau_L}. \tag{4.38}$$

The size of superhorizon fluctuations decreases with n, so we expect the lifetime τ_L to increase with n. This explains qualitatively the results shown in Fig. 4.8.

τ_L is constant only when the superhorizon fluctuations remain constant in time. For the two power spectrums discussed in Fig. 4.9, $\tau_L = \tau_L(\tau)$. If we solve the ODE considering $\tau_L(\tau)$ to be slowly varying, then the solution becomes

$$L(\tau \gg \tau_{\text{ann}}) = L_{\text{attr}} - \frac{\tau_{\text{ann}}}{\tau_L(\tau)}, \tag{4.39}$$

which is not constant. If τ_L becomes very small (e.g. due to the inclusion of an overall bias), then the last term in Eq. (4.37) flips its sign and becomes negative, with the solution of the ODE now becoming a decaying exponential

$$L(\tau \gg \tau_{\text{ann}}) \propto \tau \exp\left(-\frac{\tau}{\tau_L}\right). \tag{4.40}$$

I want to clarify that this model was not built with the objective of fitting the simulation data, but rather to show that the qualitative behaviour of the system can be seen from just a simple model with easily interpretable terms. That is, there is an attractor solution, and the value of the normalized length in this solution varies with n due to the localized bias introduced by the superhorizon fluctuations. For the sake of simplicity we introduced exponential decay through the $-L/\tau_L$ term in the ODE, but actually the form of that term should be derived so that Eq. (4.40) is a decaying exponential, without that extra τ factor. Additionally, if one wanted to make this a predictive model, one would have to consider that τ_{ann} and τ_L depend on the velocities and the size of the voids in the network, which as well depend on n. A model for the velocities would also need to be included, and the values of all the coefficients would need to be fitted through simulations.

Chapter 5

Domain wall stability with biased initial conditions

If the initial distribution of field values at the time of oscillation is biased towards one of the minima (population bias), the dynamics of the domain wall network will change. It was seen that, for white noise initial conditions, even relatively small biases lead to the rapid decay of the network [89, 90]. This was thus proposed as a way to avoid wall domination, with inflation as a straightforward mechanism to induce large-scale biases onto the system.

However, as we have seen, if inflationary initial conditions are properly taken into account, the domain wall networks are generated differently. In Sec. 5.1 we will see how networks with inflationary fluctuations are very stable, even for relatively large biases. In Sec. 5.2 we will delve further into the behaviour of the system by studying how the network formation and lifetime are affected by population biases for a general power law power spectrum of initial fluctuations.

5.1 Stability for inflationary initial conditions

In order to more easily understand what happens in the case of scale invariant initial conditions, let us see the results in contrast to the white noise ones.

5.1.1 Quantifying the bias size

The computer simulations have a limited box size. Although there may be local biases, the field average at the whole simulation size is almost zero for both white noise and scale invariant initial conditions. The way in how the bias is introduced is by adding a fixed value δ to all of the field values at initial time.

The effect of this bias δ in the simulation will depend on how large the fluctuations are. For this purpose we introduce the bias parameter b_d,

$$b_d \equiv \frac{\langle \phi \rangle}{\sqrt{\langle \phi^2 \rangle}} = \frac{\delta}{\sigma}, \tag{5.1}$$

where σ is the standard deviation of the field values at the initial time.

5.1.2 Visualizing the network decay

In Fig. 5.1 we can see how, in the absence of biases, the network is stable, but for progressively larger biases the network becomes more and more sparse over time. It is also worth noting that even for relatively large biases ($b_d = 0.5$, bottom row) the network still does not decay completely during the simulation time.

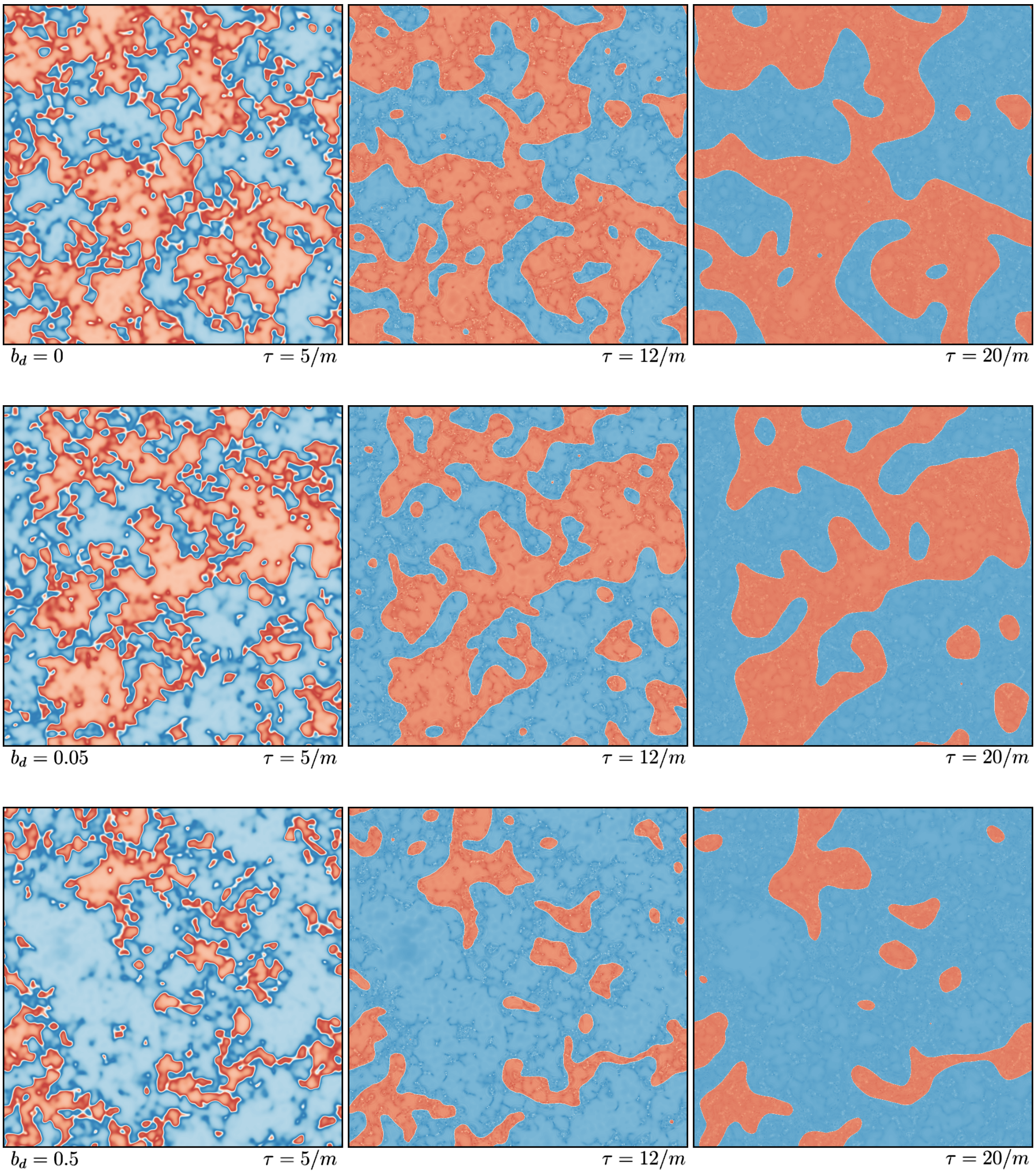

FIGURE 5.1: Snapshots of the domain wall network for bias parameter $b_d = 0$ (top row), 0.05 (middle row) and 0.5 (bottom row); at times $m\tau = 5$ (left column), $m\tau = 12$ (middle column) and $m\tau = 20$ (right column). Blue and red regions correspond to $\phi > 0$ and $\phi < 0$ respectively. The initial fluctuation power spectrum is scale invariant for all bias parameters. The box contains $\sim 40^2(10^2)$ horizons at time $m\tau = 5(20)$.

5.1.3 Quantifying the network decay

Normalized length

Following our studies in the past chapter, a straightforward way to quantify the network decay is to see how the normalized domain wall length L, as defined in Eq. (4.14), evolves with time for a network with nonzero bias.

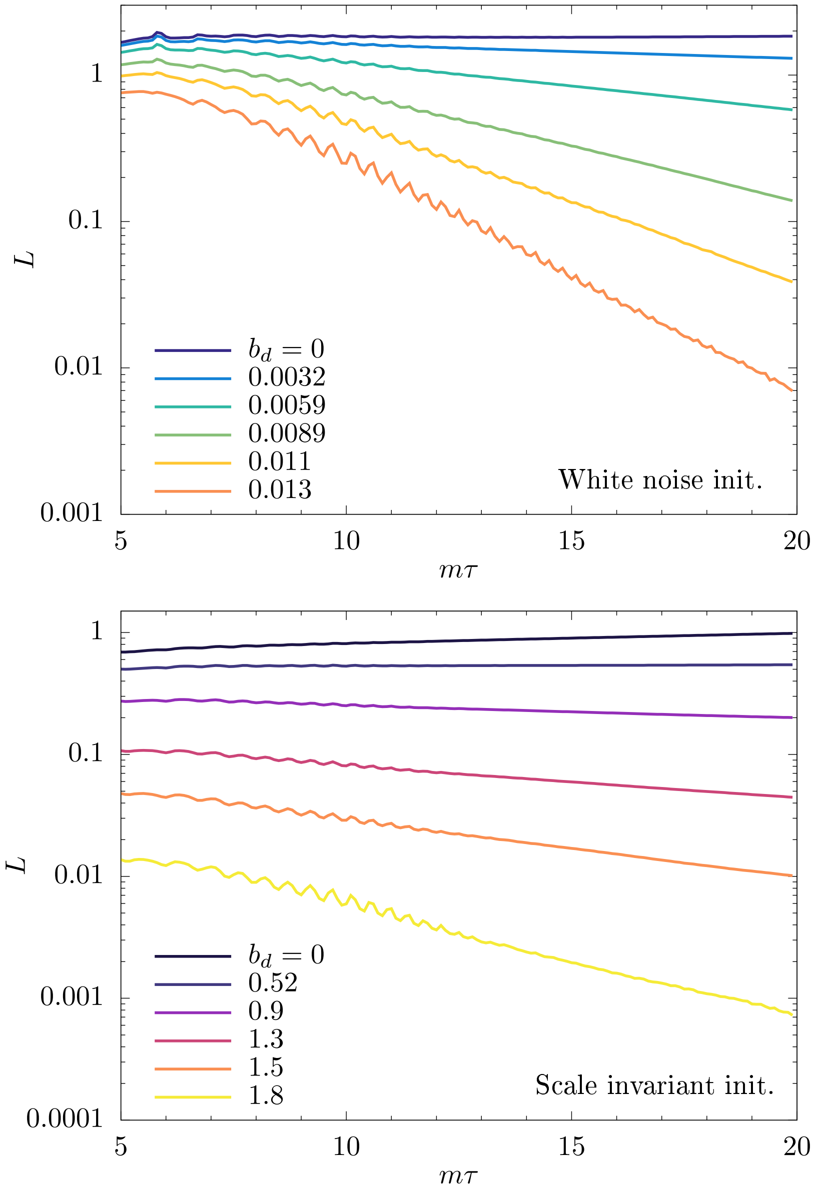

FIGURE 5.2: Time evolution of the normalized length L for various values of the bias parameter b_d for which the domain wall network forms and subsequently decays. The values of b_d are chosen differently for white noise (top) and scale invariant (bottom) initial conditions, as the latter are more stable than the former. We can see how, in both cases, the magnitude L follows an exponential decay law. From a set of 2D, 4096^2 simulations with 200^2 horizons at initial time, 50 averages taken per bias parameter. Field values are set such that the position space field variance is $\sigma = 0.1$. Very similar results were found for $\sigma = 0.01$, 0.001 as well as when setting the white noise values in Fourier space.

If b_d is too small, then the decay is not noticeable, but if it is too large, the network will not form in the first place. In Fig. 5.2 we can see how L evolves with time, for bias parameters chosen so that the network forms and subsequently decays.

The first thing to note is that the bias parameters studied for scale invariant initial conditions are about 2 orders of magnitude larger than those for white noise initial conditions. That is to say, for $b_d = \mathcal{O}(1)$, networks with white noise initial conditions would not form altogether, and for $b_d = \mathcal{O}(0.01)$, which leave networks with scale invariant initial conditions almost unaffected, networks with white noise initial conditions almost decay completely.

The second feature to note is that the decay seems to be exponential in τ. The fact that the energy density ρ decays exponentially was first noticed in 1996 for white noise initial conditions by Coulson et al [93]. We are studying L, which is directly proportional to the energy density if appropiately normalized by the horizon size. It is reassuring to see that the decay also follows an exponential law in the scale invariant case—that suggests that although the networks are more stable, the domain wall dynamics themselves remain unchanged.

Another aspect to note is that L at the time of domain wall formation (around $m\tau = 5 \sim 6$) is reduced considerably for the decay-inducing biases in the scale invariant initial condition case. This is because the bias are so large that domain wall formation is severely hindered from the start.

We think that the reason why these network are so stable is because of the void structure mentioned in Sec. 4.3.1. Even if domain wall formation is hindered due to the bias, superhorizon correlations induce voids and relatively straight domain walls which span several Hubble horizons. As the universe expands, these large scale correlations keep entering the horizon and avoid the network from completely decaying.

The consequences of these findings for axion cosmology are drastic—if a high energy domain wall network is generated, an initial population bias will not be enough to make it decay in time. On the other hand, the bound on domain wall tension is relaxed. The initial domain wall length for $\mathcal{O}(1)$ bias parameter and scale invariant fluctuations is ~ 6 times smaller than for unbiased white noise, which means that the $\sigma_{\rm W} < (0.92\ {\rm MeV})^3$ bound from [140, 141] now becomes

$$\sigma_{\rm W} < (1.7\ {\rm MeV})^3\,. \tag{5.2}$$

Volume ratio

Another interesting observable of the system is what we call the volume ratio r

$$r \equiv \frac{2S_-}{S_+ + S_-}, \tag{5.3}$$

where $S_+(S_-)$ is the total area where field values of ϕ are positive (negative). Here, r is defined so that it is bounded as $r \in [0, 2]$. For the unbiased case, the initial value is $r = 1$ and we would expect it to remain constant and equal to 1 as time goes on, given that the statistics are good enough.

In Fig. 5.3 we can see how r evolves with time for the same decay-inducing biases used in Fig. 5.2. The observed features are remarkably similar to those of the time evolution of L, with an exponential decay law being followed in both cases. Interestingly, the small ripples in L are not found in r, as small-scale scalar fluctuations affect the way in how we calculate L but not r.

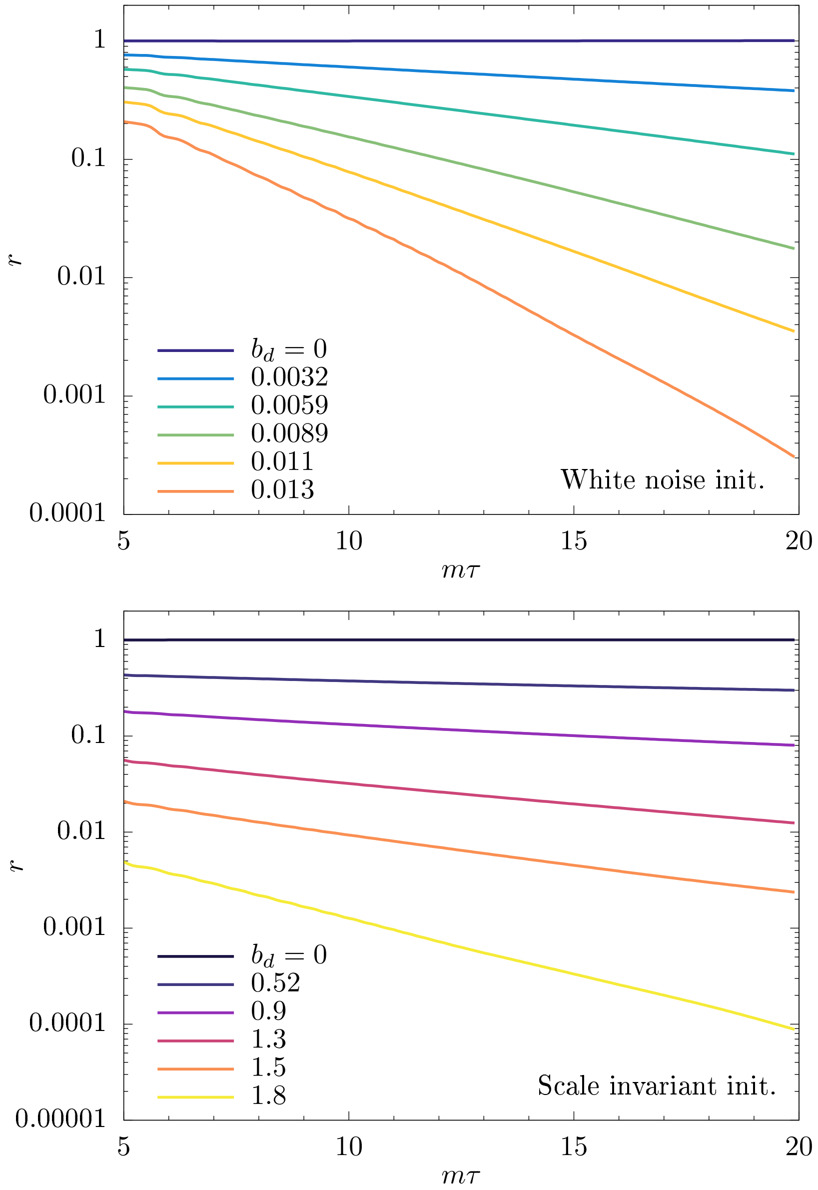

FIGURE 5.3: Time evolution of the volume ratio r for various values of the bias parameter b_d for which the domain wall network forms and subsequently decays. The values of b_d are chosen differently for white noise (top) and scale invariant (bottom) initial conditions, as the latter are more stable than the former. We can see how, in both cases, the magnitude r follows an exponential decay law. From a set of 2D, 4096^2 simulations with 200^2 horizons at initial time, 50 averages taken per bias parameter. Field values are set such that the position space field variance is $\sigma = 0.1$. Very similar results were found for $\sigma = 0.01$, 0.001 as well as when setting the white noise values in Fourier space.

5.1.4 Lifetime

Both L and r seem to follow exponential decay laws in τ, which inspires a computation of associated decay time scales, or lifetimes τ_L and τ_r like

$$L(\tau) \propto 10^{-\tau/\tau_L}, \tag{5.4}$$

$$r(\tau) \propto 10^{-\tau/\tau_r}. \tag{5.5}$$

Choosing a base 10 for the exponential lets us interpret the lifetimes more easily—for one lifetime τ_L the normalized length will have decayed, on average, one order of magnitude.

In Fig. 5.4 we can see the lifetimes for both scale invariant and white noise initial conditions, for both L and r. Notice that, in the same way as in the previous plots, the b_d ranges of interest are also different for each initial condition setting.

At first glance, the results may look discouraging—both lifetimes do not match! Indeed, these two time scales cannot be used straightforwardly to describe the lifetime of the system in an unified way, and it is easy to gain an intuition of why that is the case.

Let us consider an idealized case of a system that just has one infinitely long, zigzagging but otherwise straight domain wall. As time goes on, the zigzags become smoothed out and L will first decrease, then increase proportional to τ after it has become straight enough. On the other hand, r stays constant. τ_L and τ_r are the decay lifetimes of two magnitudes which are, geometrically, uncoupled, as one quantifies something in $d-1$ dimensions while the other is in d. The only thing coupling the time evolutions of L and r are the network dynamics.

In Fig. 5.5 we can see the same lifetimes, but now plotted like τ_L as a function of τ_r. We can see how the results for both initial condition settings approximately match up. This is, again, reassuring. The ratio between τ_L and τ_r changes depending on the relative amounts of smoothing and contraction of the domain walls. Even if the different initial conditions make the networks more stable, we would expect that the dynamics themselves do not change that much, and thus the results should approximately match. The match is not exact, which tells us that the dynamics do indeed change slightly with the initial conditions. This would have to be taken into account in a detailed model of the network dynamics, if we were to build one.

Another important takeaway from this figure is that τ_L is not linear with τ_r. If their relationship were linear, then we could just use one of them to describe the lifetime of the system as a whole and obtain the other through some simple dimensionality factor. However, that is not the case—the amounts of stretching and shrinking of the domain walls change depending on the bias.

As a technical note, in the unbiased case, L increases slightly with time. Since we have seen that this is a dynamical range effect, we estimate that the increase will be mostly independent on the bias, and subtract this increase from the biased simulation results before making the fit to τ_L.

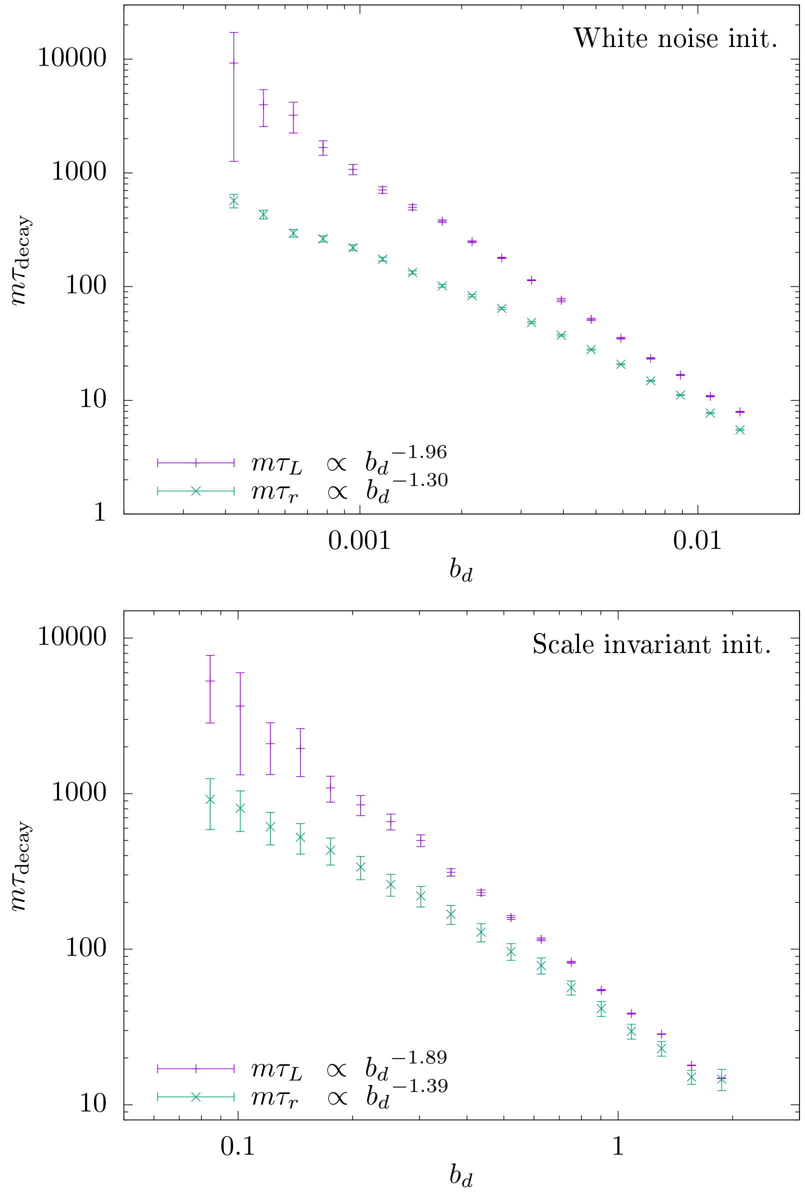

FIGURE 5.4: Lifetimes of the normalized length (τ_L, in purple) and volume ratio (τ_r, in green) assuming exponential decay, for both white noise (top) and scale invariant (bottom) initial conditions. Values of τ_L (τ_r) are computed as -1 times the inverse of the slope of the base-10 logarithm of L (r) in the interval $[\tau_{\mathrm{form}}, \tau_{\mathrm{end}}] = [6, 20] \cdot 1/m$. The increase of L due to the limited dynamical range is estimated with unbiased simulations, and then subtracted from the values of L in biased simulations before computing the slope, with the assumption that this increase depends weakly on b_d. Power law fits for the lifetimes are shown in the legend. From a set of 2D, 4096^2 simulations with 200^2 horizons at initial time, 50 averages taken per bias parameter. 1σ errorbars from weighted least squares fit uncertainties. Field values are set such that the position space field variance is $\sigma = 0.1$. Very similar results were found for $\sigma = 0.01$, 0.001 as well as when setting the white noise values in Fourier space.

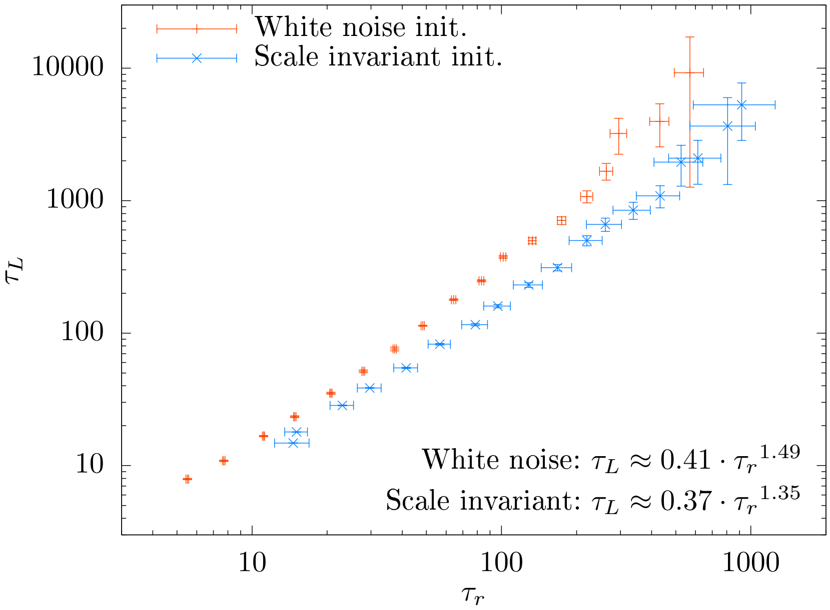

FIGURE 5.5: Relationship between the lifetime of the normalized length (τ_L, y axis) and volume ratio (τ_r, x axis), for both white noise (orange) and scale invariant (blue) initial conditions. We can see how they are not proportional to eachother, but rather follow a power law dependence between them. Fitted values are shown on the bottom right corner. See Fig. 5.4 for the values of the chosen bias parameters b_d as well as for how the decay lifetimes are calculated.

5.1.5 Percolation theory

Consider a space of d dimensions with a certain regular tiling. Let us consider a cubic lattice for simplicity, with a certain finite lattice spacing, and assume that at each lattice site the physical system can be in one or two vacua, which we will call $[+]$ and $[-]$. The probability of a lattice site being in $[+]$ is denoted by p, with $0 \leq p \leq 1$, while the probability for $[-]$ is $1-p$. If there is no correlation between the vacuum structures at any two different lattice sites, then we can apply percolation theory to compute the critical threshold p_c for which, as long as $p < p_c$, a percolating cluster (an infinitely connected cluster of $[-]$ cells) can form.

This argument was used in early literature [1, 89, 90, 91, 93, 96] to analytically describe whether the domain wall network is stable or not under a certain bias. That is, as long as a percolating cluster forms, the network will be stable. However, this argument cannot be used—the percolating threshold depends on the dimensionality, on what we consider a first neighbour (bond vs site percolation) as well as on the lattice shape. This is completely different from what we are studying! The scalar field dynamics do not change depending on which discretization of the continuum we choose, but the percolation thresholds are different, for example, for a square lattice and for a triangular lattice. Furthermore, for a square/cubic lattice in 3D, if unbiased ($p = 0.5$), an infinitely percolating cluster is found, while in 2D it is not found. This radical change in behaviour with the number of dimensions is not what we expect from the behaviour of the scalar field. Although part of the literature has moved on from this percolation theory picture, no paper had yet disproven its applicability to the study of domain wall networks.

5.2 Stability for generalized initial conditions

Although the case of most cosmological interest are scale invariant initial conditions, parametrizing the initial fluctuation power spectrum as in Sec. 4.5.1 lets us transition smoothly from the scale invariant to the white noise cases, and thus better understand the behaviour of the system.

5.2.1 Computational setup

The reduced power spectrum of initial fluctuations is set to,

$$\mathcal{P}(k) = C_n k^n, \tag{5.6}$$

where C_n is defined as Eq. (4.26) so to make the position space fluctuation size constant with n. The value $n = 0$ corresponds to scale invariance and $n = 2$ to white noise in 2D. Simulations are run for a set of 36 different $n \in [-0.5, 3.0]$ linearly spaced, as well as 36 different bias parameters, logarithmically spaced $b_d \in [1.5 \cdot 10^{-4}, 3]$. The number of repetitions varies depending on the combination of n and b_d, being higher for the regions of stable domain wall formation (5 repetitions) and visible decay (25 repetitions), for a total of ~ 8000 repetitions.

Something that I glossed over in Sec. 4.5.1 was that, when studying these generalized initial conditions, I switched from setting random Gaussian noise in position space to Fourier space. In unbiased simulations both are equivalent, but in biased simulations, the Fourier space setting is preferred. This is because the small error of the pseudorandom number generator accumulates over all field values when setting them in position space, while when setting in Fourier space, the inverse Fourier transform partially cancels them out. For a 16384^2 lattice size, without introducing any bias nor correction, using the Kahan summation method to minimize numerical error, I obtained,

$$\begin{aligned} \langle \phi_{\text{pr}} \rangle_{\text{Pos. space}} &\approx 10^{-6} \\ \langle \phi_{\text{pr}} \rangle_{\text{Fourier}} &\approx 10^{-12}, \end{aligned} \tag{5.7}$$

where ϕ_{pr} is the dimensionless program field values. If the studied biases are large, then this small accumulated error is not relevant, but in our case, $\sigma = 0.01$ and thus the minimum bias δ applied to the field is of comparable size to this accumulated error. If future research becomes interested in the behaviour for even smaller biases, then I believe that a careful study of the pseudorandom number generator statistics may be necessary.

5.2.2 Domain wall generation

The first magnitude we are interested in is the values of L and r at the time of domain wall formation, $\tau_{\text{form}} = 6/m$. The results can be seen in Fig. 5.6. We see how, for L, both large biases and large superhorizon fluctuations hinder the domain wall formation. The unbiased value of r is 1 for all values of n so the contours in that case become simpler.

5.2.3 Zones of decay

Another magnitude of interest is the increment of L or r from the time of domain wall formation to the final time of the simulation, which I called ΔL and Δr respectively. The results can be seen in Fig. 5.7. Red zones are those of high network decay. We can see how these form a diagonal line, and suggesting that the network in the region of large superhorizon fluctuations, small bias, either does not decay at all or does so beyond our computational reach.

The previously studied increase of L with time due to the limited dynamical range appears in the top plot as a light blue region. I think that it is interesting how the limited dynamical range effects are less noticeable, or maybe even unnoticeable, in the Δr plot (bottom half). Let us focus our attention to the light grey isolines, $\Delta L = 0.1$ on the top, $\Delta r = 0$ on the bottom plots. The objective of those isolines is to make the result variance more easily visible. We can see how the $\Delta L = 0.1$ isoline is mostly vertical, showing that the increase is indeed higher for larger superhorizon fluctuations. On the other hand, the result variance for Δr does not have that dependence on n. Also interesting to note is how the blue shaded region abruptly stops at $n = 2$, thus suggesting that the dynamical range effects are almost unnoticeable for $n > 2$.

5.2.4 Lifetimes

Finally, we are interested in the lifetimes of L and r. The results can be seen in Fig. 5.8. We can see both lifetimes have a simple dependence on b_d and n, which suggests to me that these are well chosen parameters to build an analytical model.

A quirk of the phenomenological model presented in Sec. 4.5.2 was that, even for a global nonzero bias, only when the last term in Eq. (4.37) flips sign, then the system can decay. Maybe with incredibly large statistics and precision we can disprove this and find that even for very small biases, the system does slightly decay. However, in Fig. 5.8 we can see two regions of large fluctuations of the lifetimes (bottom-left quadrants), which did not seem to improve even when increasing the statistics. A more careful study would be required, but these results are a hint that that model quirk may actually be present in the realistic system as well. That is, for these regions which large result variance of τ_L and τ_r, the network may be completely stable even with a small, nonzero bias.

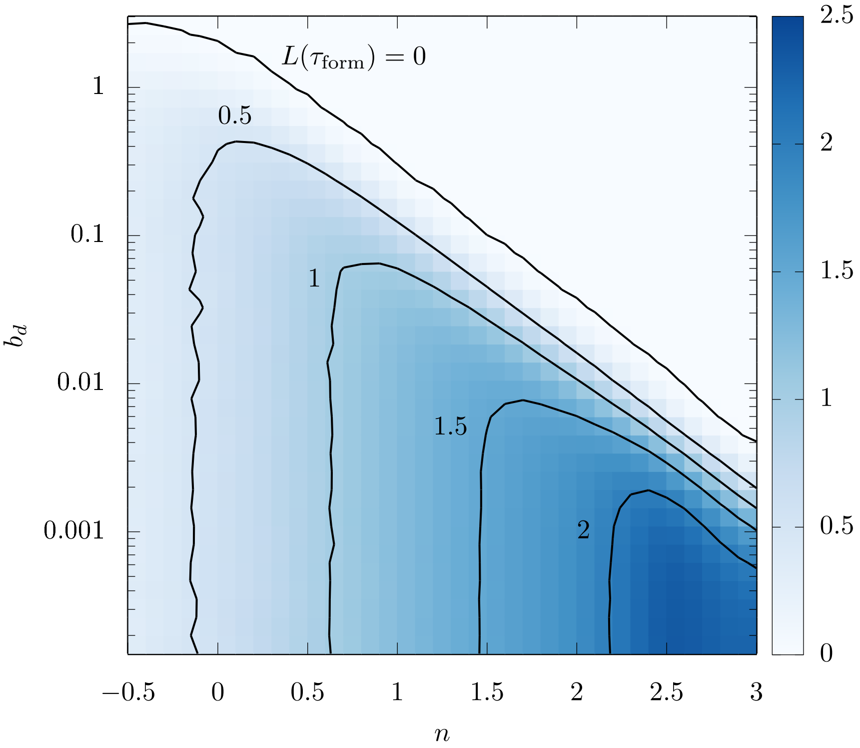

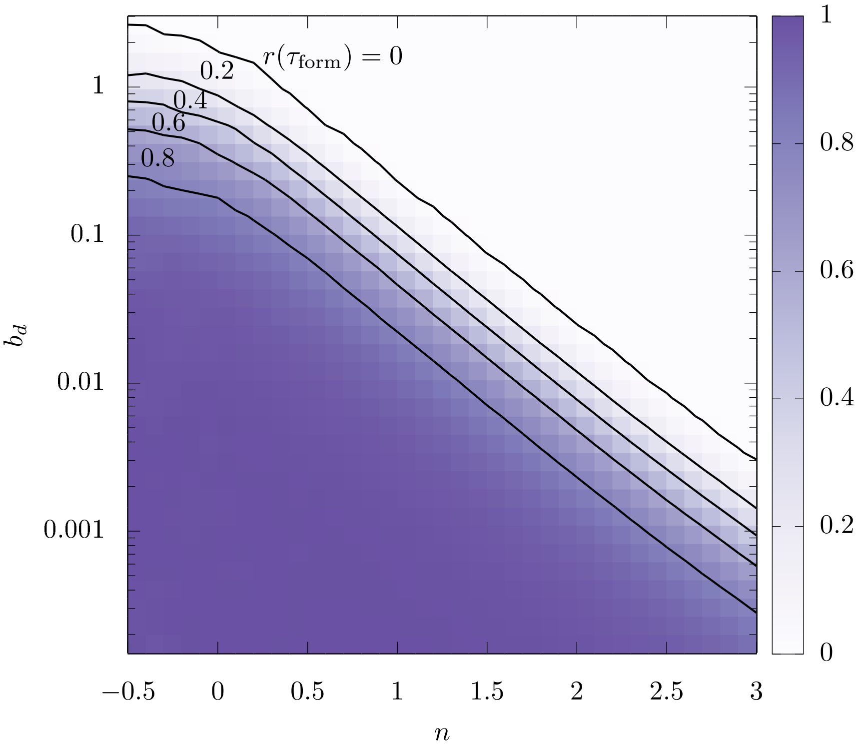

FIGURE 5.6: Normalized length (L, top) and volume ratio (r, bottom) at the time of domain wall formation $\tau_{\rm form} = 6/m$. Values from a set of 2D, 16384^2 simulations with 800^2 horizons at initial time of varying initial condition spectral index n and bias parameter b_d. Computed values are shown with color, zones of the parameter space where domain walls form are shown in either blue or purple, while zones in which domain walls do not form altogether are shown in white. The low-bias values of L increase with n since, for the unbiased case, $L(\tau_{\rm form}) \approx L_{\rm attr}$ which depends on n. Isolines are obtained by interpolation, shown for linear increments of both L and r.

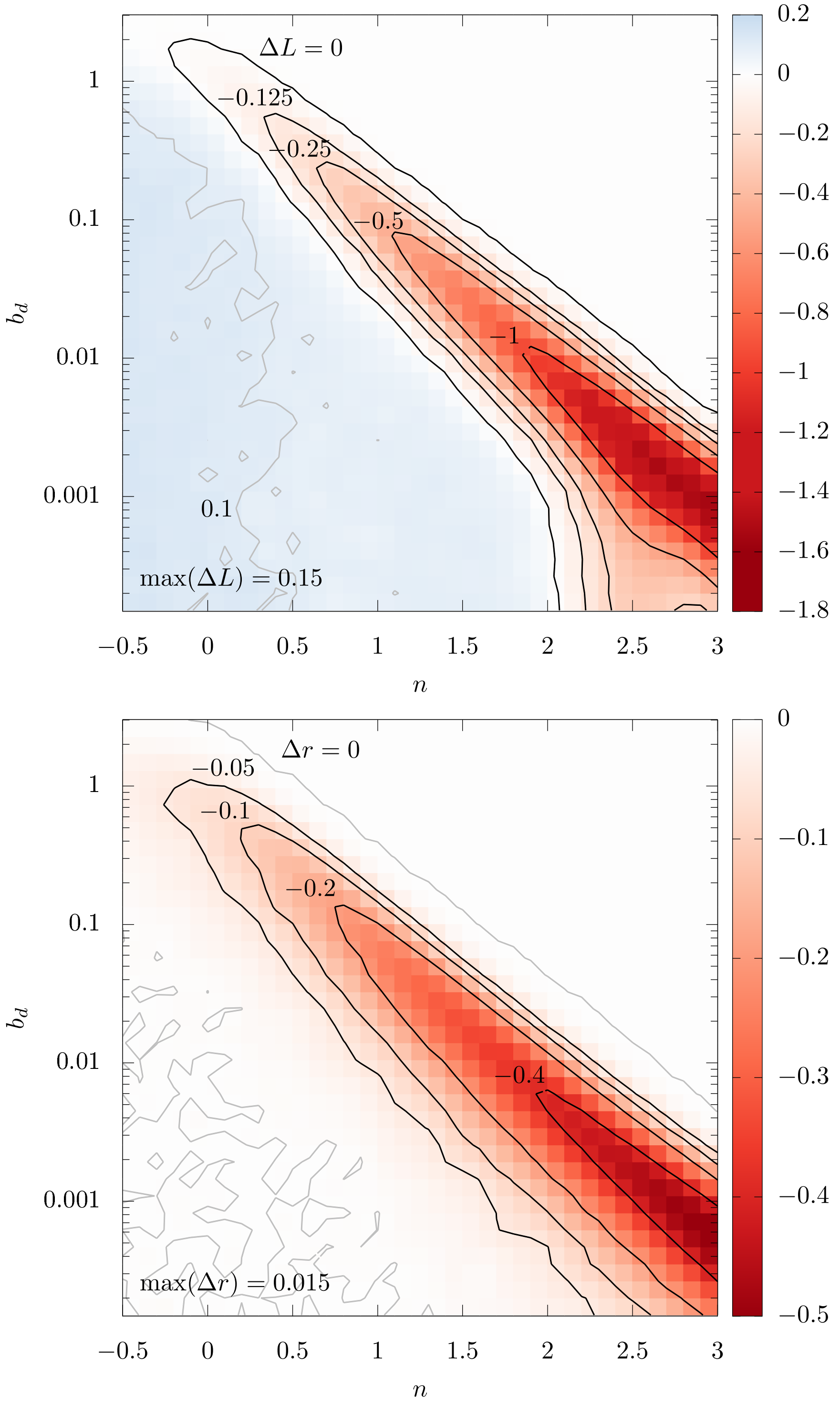

FIGURE 5.7: Increment of the normalized length (ΔL, top) and volume ratio (Δr, bottom) from the time of formation $\tau_{\text{form}} = 6/m$ to the end of the simulation $\tau_{\text{end}} = 20/m$. Values from a set of 2D, 16384^2 simulations with 800^2 horizons at initial time of varying initial condition spectral index n and bias parameter b_d. Computed values are shown with color, with zones of network decay appearing in red, stability in white. The increase of L due to the limited dynamical range is shown in blue. Isolines are obtained by interpolation, shown for logarithmic increments of both ΔL and Δr. An extra isoline for visualizing the result variance in the low-bias, high-cosmic variance zone (bottom left quadrant) has been added in light grey, as well as the maximum values of both ΔL and Δr.

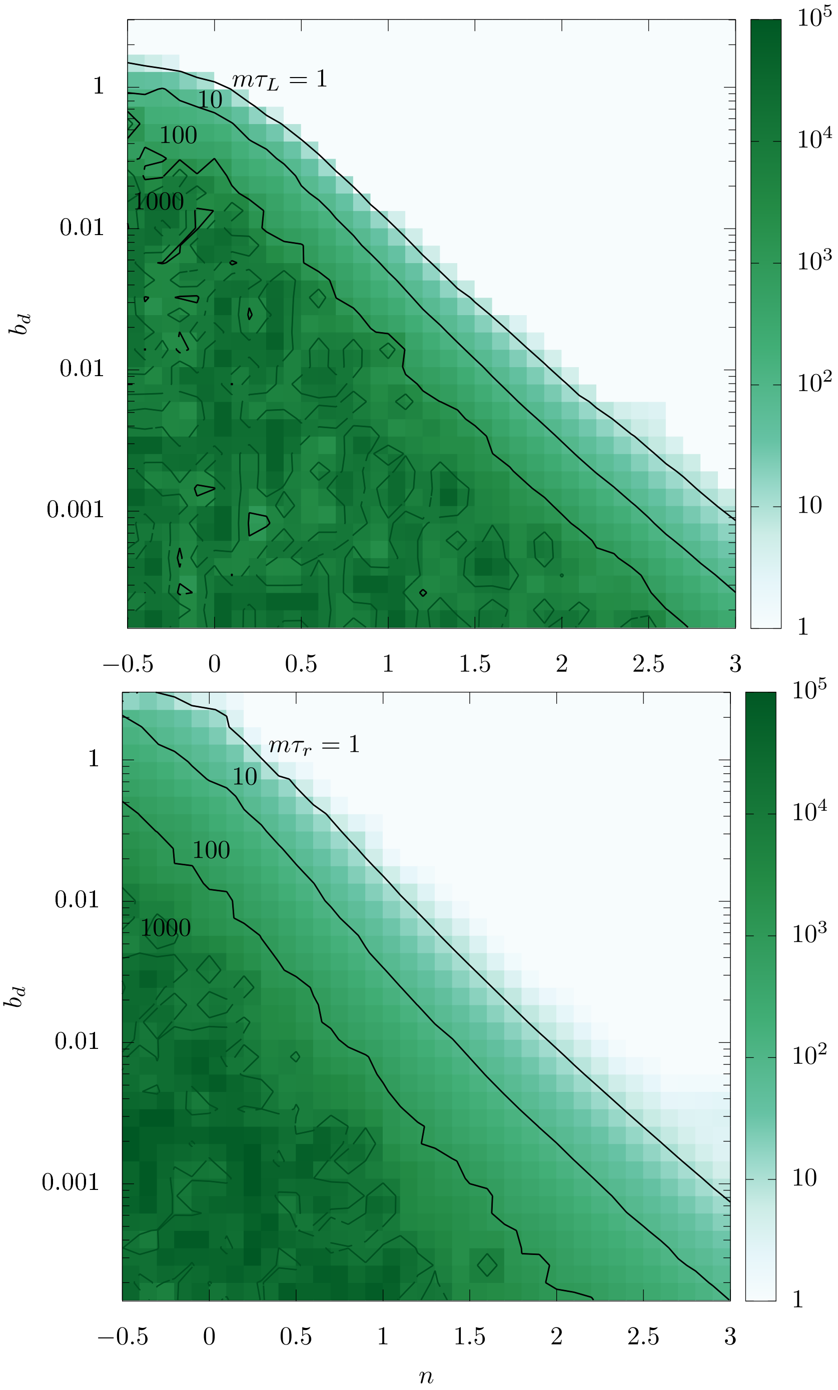

FIGURE 5.8: Lifetimes of the normalized length (τ_L, top) and volume ratio (τ_r, bottom) assuming exponential decay. Values from a set of 2D, 16384^2 simulations with 800^2 horizons at initial time of varying initial condition spectral index n and bias parameter b_d. Values of $\tau_L(\tau_r)$ are computed as -1 times the inverse of the slope of the base-10 logarithm of $L(r)$ in the interval $[\tau_{\text{form}}, \tau_{\text{end}}] = [6, 20] \cdot 1/m$. The increase of L due to the limited dynamical range is estimated with unbiased simulations, and then subtracted from the values of L in biased simulations before computing the slope, with the assumption that this increase depends weakly on b_d. The colorbar is in log scale. In the cases where either L (after corrections) or r increased with time, its corresponding lifetime was set to a very large value ($\sim 10^5/m$). Zones of stable network formation appear in deep green, decay zones in light green, no formation in white. Isolines are obtained by interpolation, shown for logarithmically spaced intervals. An extra isoline for visualizing the result variance in the low-bias, high-cosmic variance zone (bottom left quadrant) has been added in green.

Chapter 6

DW network signatures in the CMB

The CMB has become a vital tool to probe the universe at the time of recombination. Anisotropies of the CMB are directly related to the structure formation in the universe, as galaxies and galaxy clusters formed from the same primordial density fluctuations that left their imprint on the CMB. If a domain wall network already existed during recombination, it would leave its mark on the CMB anisotropies. We will review various of these signatures in Sec. 6.1.

CMB light is linearly polarized. It can be decomposed into parity-even E modes and parity-odd B modes. In recent years, the B mode measurement accuracy has improved considerably, which has led to the first hint of isotropic cosmic birefringence—the rotation of the polarization of the CMB light during its propagation. Stable domain wall networks lead to nonzero isotropic and anisotropic cosmic birefringence. We discuss this novel effect in detail in Sec. 6.2.

6.1 CMB anisotropies

At $z > 1100$ the universe was almost completely ionized, with photons, protons and electrons tightly coupled via electromagnetic interactions. Photons scatter mostly off electrons since the photon-proton scattering cross-section is suppressed by a factor of $(m_e/m_p)^2 \sim 10^{-6}$. As the universe expands and cools down, electrons and protons combine to form neutral hydrogen, turning the universe transparent. This process is known as recombination. It is a confusing name, since there has been no previous "combination" period, but it is called like this for historical reasons. Photons cease to scatter, and free stream in all directions. What we observe in our experiments is the intersection of our past light cone with the surface of constant cosmic time at $z \sim 1100$, which is called the last scattering surface (LSS).

The transition from the opaque universe to the free-streaming photons was not instantaneous, which implies that the LSS has a finite thickness. This is important for two reasons: first, small angle anisotropies appear smeared out as this three-dimensional LSS is projected onto the two-dimensional celestial sphere. This leads to the damping of the small-scale acoustic peaks. Second, these last few scatters determined the polarization of the CMB light, as the scattering amplitudes are polarization-dependent.

Temperature and polarization anisotropies were imprinted during this transitional epoch at $z \sim 1100$. Since the CMB spectrum is an extremely good blackbody with a nearly constant temperature across the sky T_0, it is studied in terms of its temperature fluctuations $\Theta(\hat{\mathbf{n}}) = \Delta T/T_0$. Their multipole expansion is defined as

$$\Theta_{lm} = \int \mathrm{d}\hat{\mathbf{n}} Y^*_{lm}(\hat{\mathbf{n}})\Theta(\hat{\mathbf{n}}), \tag{6.1}$$

where $\hat{\mathbf{n}}$ is a unitary vector for the direction on the sky and $Y^*_{lm}(\hat{\mathbf{n}})$ are the spherical harmonics. The TT power spectrum is defined as

$$\langle \Theta^*_{lm}\Theta_{l'm'}\rangle = \delta_{ll'}\delta_{mm'}C_l^{TT}. \tag{6.2}$$

If the CMB fluctuations are Gaussian, then it is fully characterized by its power spectrum [123]. Power spectrums of E modes (EE), B modes (BB) and their cross correlations (TE, TB, EB) are defined similarly. We will see those in detail later in Sec. 6.2.2 after we formally define E and B modes.

6.1.1 The acoustic peaks

The first domain wall constraint is found within the CMB acoustic peaks.

Prior to recombination, due to radiation pressure, the plasma undergoes acoustic oscillations at subhorizon scales. Once the photons become free-streaming, the former low and high density regions of the plasma are imprinted in the photon energies. In the case of inflationary fluctuations, acoustic oscillations of a given wave number k are all in phase and have a fixed amplitude at decoupling. Modes caught at extrema of their oscillations become the peaks in the CMB temperature power spectrum Fig. 6.1, forming a harmonic series based on the distance sound can travel by recombination, the sound horizon.

Plenty of very interesting physics can be obtained from the size and position of these peaks. Odd-numbered peaks (first, third, fifth...) are associated with how much the plasma has fallen into gravitational potential wells, while even-numbered peaks (second, fourth...) are associated with how the plasma rebounds, i.e. how much it rarefies. Thus, the baryon contents of the universe are going to enhance the size of odd-numbered peaks. The nonzero thickness of the LSS blurs small scale fluctuations, which is why peaks at high multipoles are smaller in size. The curvature of the universe affects the position of the peaks, as the characteristic distance (the sound horizon) corresponds to a different angular amplitude depending on how light rays propagate through spacetime.

Prior to the precise measurement of the first few peaks, two theories contended for explaining the formation of structure on the universe: inflation and high energy topological defects such as cosmic strings, also called field ordering theories. If topological defects contribute significatively to the gravitational collapse and subsequent structure formation, modes of a given wavenumber k are in general not in phase and the distinctive series of acoustic peaks is blurred into one large peak [138, 50]. We can understand this intuitively the following way. Although the time evolution of the field is deterministic, defect network evolution is highly non-linear

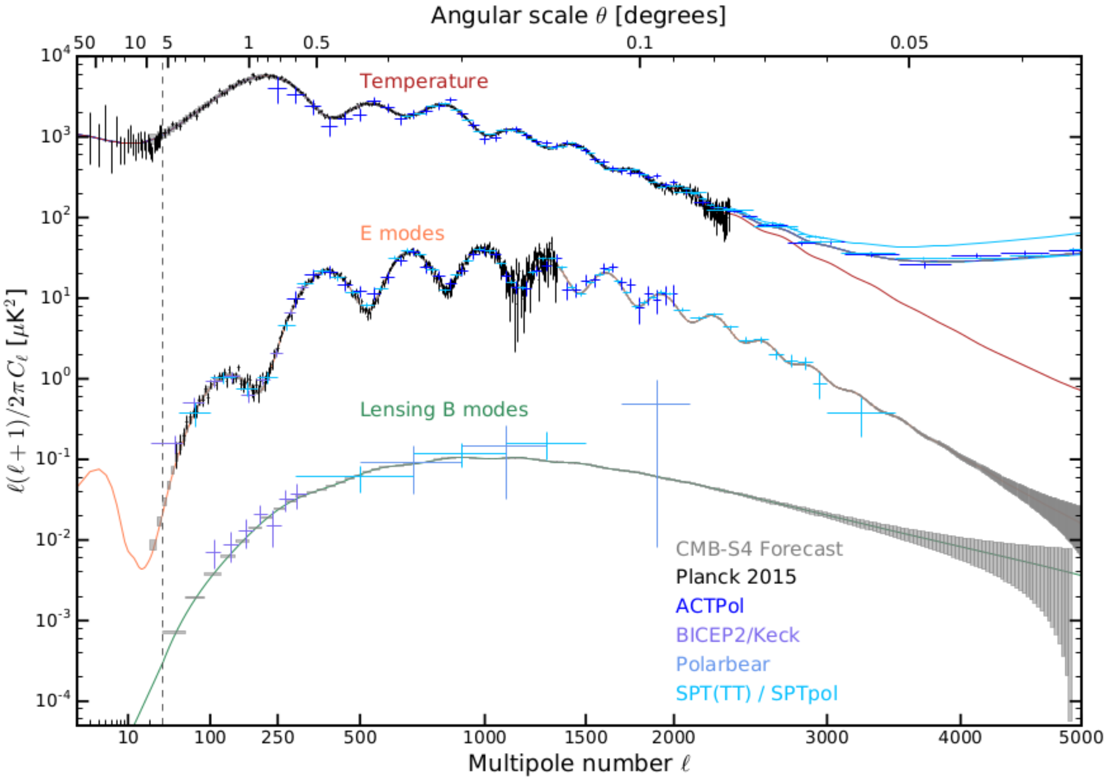

FIGURE 6.1: Current measurements of the angular power spectrum of the CMB temperature and polarization anisotropies. Best-fit models of residual foregrounds plus primary CMB anisotropy power for temperature datasets are also plotted. Projections for next-generation CMB experiments (CMB-S4) are shown in grey. Figure from [130].

and thus different Fourier modes get mixed. The fact that a clear series of acoustic peaks was observed greatly constrained all topological defect models, domain walls among them.

6.1.2 Sachs-Wolfe effect

There are several processes which distort the CMB photon trajectories and energies as we observe them today from the Solar System. Variations in the gravitational potential (e.g. due to matter overdensities) will induce gravitational redshift onto photons propagating through the potential well, which is seen as a change in the photon energy. This is known as the Sachs-Wolfe effect [116]. In regular CMB cosmology it is usually further divided into two types, non-integrated Sachs-Wolfe effect, for the anisotropic distortion coming from the primordial matter overdensities on the LSS; and integrated Sachs-Wolfe effect, for the isotropic distortion coming from the many galaxies and clusters between the LSS and us.

Any kind of fluctuation of the metric will produce a Sachs-Wolfe effect. Of our particular interest are domain walls, which depending on their tension will induce stronger or weaker metric fluctuations. Considering that we have not directly seen the Sachs-Wolfe effect induced by domain wall networks, their tension becomes bounded by $\sigma_\mathrm{W} < (1\ \mathrm{MeV})^3$ [137].

6.1.3 Scalar, vector and tensor modes

The spacetime metric expanded in linear perturbation theory is,

$$g_{\mu\nu}(\tau,\vec{x}) = \eta_{\mu\nu}(\vec{x}) + a^2 h_{\mu\nu}(\tau,\vec{x}), \tag{6.3}$$

where $\vec{x}$ is the comoving coordinate 3-vector, $\eta_{\mu\nu}$ is the unperturbed (Minkowski) metric, and $h_{\mu\nu}$ is the linear metric perturbation. As a symmetric 4×4 matrix, $h_{\mu\nu}$ has 10 degrees of freedom, which can be expressed as a sum of scalar, vector and tensor components. These refer to their transformation properties under rotations in the background space, not under gauge transformations. The breakdown of these modes is as follows [122, 135],

$$\begin{aligned} 1+1+1+1 = 4 &\quad \text{scalar} \quad (2\text{ physical, }2\text{ gauge}),\\ 2+2 = 4 &\quad \text{vector} \quad (2\text{ physical, }2\text{ gauge}),\\ 2 = 2 &\quad \text{tensor} \quad (2\text{ physical}). \end{aligned} \tag{6.4}$$

The important thing about this decomposition is that, in linear perturbation theory, scalar, vector and tensor modes evolve independently. Scalar modes correspond to matter density perturbations. Vector and tensor modes, although they do perturb the CMB, do not contribute to density perturbations and thus for studying structure formation one may just focus on the scalar modes. There is no way to source primordial vector modes with a single scalar field, and thus in simple models of inflation, primordial vector perturbations vanish. Primordial tensor modes correspond to gravitational waves. The prodution of an almost scale invariant background gravitational waves is a prediction of any cosmological inflationary model, with their amplitude strongly depending on the energy scale of inflation [131].

Topological defects present during recombination can generate both vector and tensor perturbations [139]. This was first studied in the context of defects seeding structure formation, and thus domain walls were not studied in detail, as domain walls which are the dominant component in structure formation lead to domain wall domination. Years later and outside this structure formation context, simulations were performed to see the impact of non-dominant domain wall networks in the CMB anisotropies [140]. The individual constributions can be seen in Fig. 6.2.

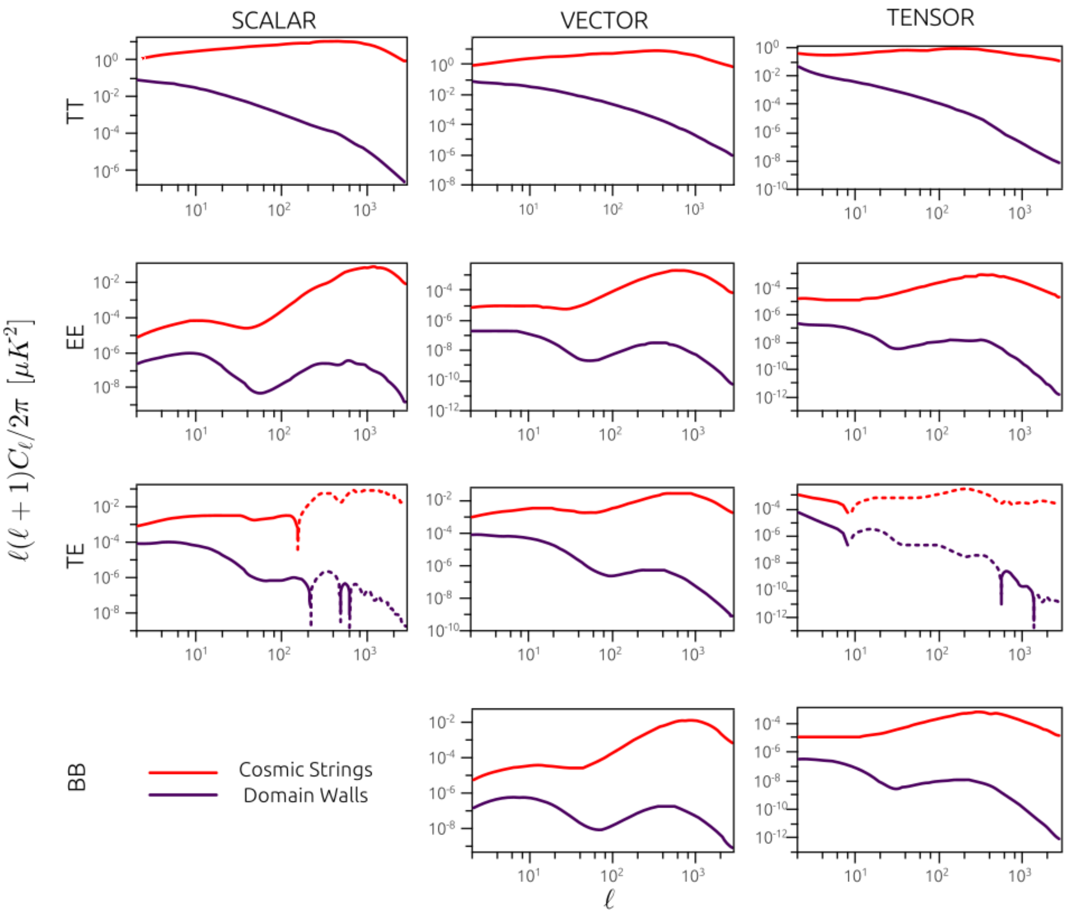

FIGURE 6.2: Comparison between the angular power spectra generated by domain wall (purple lines) and by cosmic string (red lines) networks. From top to bottom, TT, EE, TE and BB power spectra, as a function of the multipole moment l. The left, middle and right panels represent the scalar, vector and tensor components, respectively. Domain wall tension has been set so that it is non-dominant. From [140].

6.2 Cosmic birefringence

Axion fields are pseudoscalar fields which couple to photons via a Chern-Simons coupling Eq. (3.21). If the axion field value changes, then the plane of linear polarization rotates. Thus, light propagating through space with a position-dependent axion field behaves as if space was filled with a birefringent material, reason why this phenomenon is called cosmic birefringence (CB). A stable domain wall network determines how the axion field changes as we move through space, and allows us to calculate how much CB is induced upon the CMB light.

Understanding this requires us to follow a few steps. In Sec. 6.2.1 we will see why only linear polarization is generated at the time of recombination. In Sec. 6.2.2 we will define the polarization-related magnitudes which we can measure (the Stokes parameters) as well as how they relate to the E and B mode decomposition. In Sec. 6.2.3 we will see why the axion-photon coupling rotates linearly polarized light. We will estimate both isotropic and anisotropic cosmic birefringence induced by a domain wall network, and compare it to the present experimental data.

6.2.1 Origin of CMB polarization

Photons at the time of recombination have an energy 3 orders of magnitude smaller than the electron mass m_e, which implies that they scatter elastically via Thomson scattering. This scattering is polarization dependent, which leads to a polarization of the CMB anisotropies when the fact that recombination does not occur instantaneously is taken into account. The scattering cross section σ_T depends on polarization as [129],

$$\frac{\mathrm{d}\sigma_T}{\mathrm{d}\Omega} = \frac{e^4}{{m_e}^2}(\hat{\epsilon}_i \cdot \hat{\epsilon}_f)^2, \tag{6.5}$$

where $\mathrm{d}\Omega$ is the solid angle differential, e fundamental charge, $\hat{\epsilon}_i$ and $\hat{\epsilon}_f$ are the initial and final polarization vectors respectively. We can think of this as if the incident photon set up oscillations of the electron in the direction of the incident polarization. Since light cannot be polarized along its direction of motion, only one linear polarization state gets scattered. The scattered radiation intensity peaks in the direction normal to, with polarization parallel to, the incident polarization.

In reality we have a multitude of photons scattering at the same time. If incoming radiation were isotropic, then it would balance out so that the outgoing radiation would remain unpolarized. But if it had a quadrupole variation in intensity or temperature (i.e. peaks at $\pi/2$ separation), the scattered radiation becomes linearly polarized, as seen in Fig. 6.3.

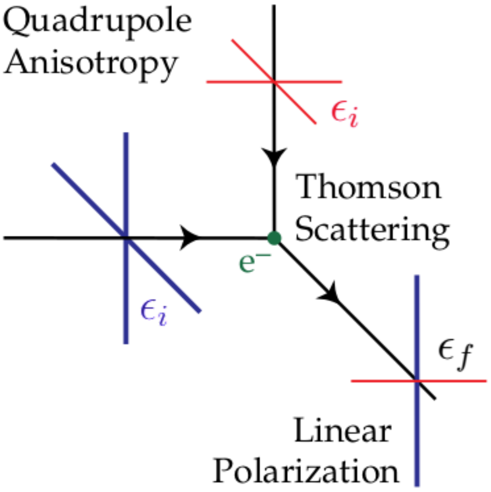

FIGURE 6.3: Thomson scattering of radiation with a quadrupole anisotropy generates linear polarization. Blue (red) represents hot (cold) radiation. Adapted from [121].

If Thomson scattering is rapid, then photons randomize and light becomes unpolarized. Understanding the polarization of the CMB reduces to understanding the quadrupolar temperature fluctuations at last scattering. Earlier we discussed scalar vector and tensor perturbations in the context of metric perturbations, which are directly related to the scalar ($m = 0$), vector ($m = \pm 1$) and tensor ($m = \pm 2$) perturbations of the quadrupole ($l = 2$) temperature anisotropy. Vector quadrupole anisotropies are expected to be negligible, acoustic density perturbations generate scalar quadrupole anisotropies, and gravitational waves generate tensor quadrupole anisotropies. Each of these sources generates distinct polarization patterns. For the following sections we just need to remember that CMB light becomes linearly polarized after the last scattering, and that circular polarization cannot be generated from Thomson scattering and quadrupole anisotropies alone.

6.2.2 E and B modes

Let us consider a monochromatic electromagnetic wave of frequency ω_0 propagating in the z-direction. Its electric field components (E_x, E_y) are

$$E_x = a_x(t)\cos[\omega_0 t - \theta_x(t)], \qquad E_y = a_y(t)\cos[\omega_0 t - \theta_y(t)]. \tag{6.6}$$

The Stokes parameters are defined as the following time averages [120]

$$\begin{aligned} I &\equiv \left\langle {a_x}^2 \right\rangle + \left\langle {a_y}^2 \right\rangle , \\ Q &\equiv \left\langle {a_x}^2 \right\rangle - \left\langle {a_y}^2 \right\rangle , \\ U &\equiv \left\langle 2 a_x a_y \cos(\theta_x - \theta_y) \right\rangle , \\ V &\equiv \left\langle 2 a_x a_y \sin(\theta_x - \theta_y) \right\rangle . \end{aligned} \tag{6.7}$$

I is positive definite and gives the radiation intensity. Q, U, and V can take either sign and describe the polarization state. For unpolarized radiation, E_x and E_y are uncorrelated and thus $Q = U = V = 0$. I and V are physical observables, but Q and U depend on the axes in relation to which the linear polarization is defined. After a rotation α around the z-axis,

$$\begin{aligned} Q' &= Q\cos(2\alpha) + U\sin(2\alpha), \\ U' &= -Q\sin(2\alpha) + U\cos(2\alpha). \end{aligned} \tag{6.8}$$

We can see how linear polarization behaves as a tensor under spatial rotations. In spherical polar coordinates (θ, φ) the metric is $g_{ab} = \mathrm{diag}(1, \sin^2\theta)$ and the polarization tensor P_{ab} becomes

$$\mathrm{P}_{ab}(\hat{\mathbf{n}}) = \frac{1}{2}\begin{pmatrix} Q(\hat{\mathbf{n}}) & -U(\hat{\mathbf{n}})\sin\theta \\ -U(\hat{\mathbf{n}})\sin\theta & -Q(\hat{\mathbf{n}})\sin^2\theta \end{pmatrix} . \tag{6.9}$$

The $\sin\theta$ factors appear since the basis is othogonal but not orthonormal. Since circular polarization cannot be generated during Thomson scattering, we expect $V = 0$ for the CMB and will not consider it further. Just as a scalar function can be expanded in terms of spherical harmonics, the polarization tensor can be expanded in terms of two sets of orthonormal tensor harmonics [120]

$$\frac{\mathrm{P}_{ab}(\hat{\mathbf{n}})}{T_0} = \sum_{l=2}^{\infty} \sum_{m=-l}^{l} \left[E_{lm} Y^{E}_{lm\,ab}(\hat{\mathbf{n}}) + B_{lm} Y^{B}_{lm\,ab}(\hat{\mathbf{n}}) \right] , \tag{6.10}$$

where T_0 is the mean CMB temperature and the expansion coefficients are

$$E_{lm} = \frac{1}{T_0} \int \mathrm{d}\hat{\mathbf{n}}\ \mathrm{P}_{ab}(\hat{\mathbf{n}}) Y_{lm}^{E\,ab\,*}(\hat{\mathbf{n}}), \tag{6.11a}$$

$$B_{lm} = \frac{1}{T_0} \int \mathrm{d}\hat{\mathbf{n}}\ \mathrm{P}_{ab}(\hat{\mathbf{n}}) Y_{lm}^{B\,ab\,*}(\hat{\mathbf{n}}). \tag{6.11b}$$

We can now give the expressions for the remaining power spectrums,

$$\langle E_{lm}^* E_{l'm'} \rangle = \delta_{ll'} \delta_{mm'} C_l^{EE}, \tag{6.12a}$$

$$\langle B_{lm}^* B_{l'm'} \rangle = \delta_{ll'} \delta_{mm'} C_l^{BB}, \tag{6.12b}$$

$$\langle E_{lm}^* B_{l'm'} \rangle = \delta_{ll'} \delta_{mm'} C_l^{EB}, \tag{6.12c}$$

$$\langle \Theta_{lm}^* E_{l'm'} \rangle = \delta_{ll'} \delta_{mm'} C_l^{TE}, \tag{6.12d}$$

$$\langle \Theta_{lm}^* B_{l'm'} \rangle = \delta_{ll'} \delta_{mm'} C_l^{TB}. \tag{6.12e}$$

These E and B modes have nothing to do with the electric and magnetic fields. The E modes are parity-even, while B modes are parity-odd. Scalar perturbations produce exclusively E mode polarization, while tensor perturbations produce B modes as well. The foregrounds (dust clouds, galaxies etc between the LSS and our detectors) can also produce B modes, and thus the foregrounds must be well understood and subtracted to obtain the primordial signal. If primordial B modes are detected, that would be an indirect detection of the gravitational wave background at the time of recombination.

If it were not for the fact that Q and U Stokes parameters are much smaller than the anisotropies of I, measuring polarization would not pose a particular experimental challenge. Most detectors are polarization sensitive or can easily be made so. However, as we have seen in Fig. 6.1, primordial E modes and B modes from the foregrounds are orders of magnitude smaller than the temperature anisotropies, which has motivated the development of polarization-exclusive probes such as Polarbear [126], the South Pole Telescope [127] and BICEP2/Keck [128]. Future experiments such as CMB-S4 [130], the Simons Observatory [132], PICO [133], and LiteBIRD [134] are designed to greatly improve current measurements.

The primary target of CMB polarization experiments is the detection of primordial tensor perturbations, but other fundamental physics can be studied by improved B-mode measurements, such as the sum of neutrino masses, the number of relativistic particle species in the early universe, possible modifications of gravity, annihilation rates of dark matter candidates, and of course cosmic birefringence [130].

6.2.3 CB in the presence of a varying axion field

The effects of a parity-violating term in the electromagnetic Lagrangian were first studied by Carroll and Field [117, 118] and then applied to the axion photon coupling one year later by Harari and Sikivie [119]. The complete Lagrangian of the electromagnetic tensor, axion field and their coupling is

$$\mathcal{L} = -\frac{1}{4} F_{\mu\nu} F^{\mu\nu} + \frac{1}{2} \partial_\mu \phi \partial^\mu \phi + \frac{1}{4} g_{a\gamma\gamma} \phi F_{\mu\nu} \tilde{F}^{\mu\nu}. \tag{6.13}$$

If the coupling term were not to be there, we would just have the Maxwell equations in vacuum and the massless Klein-Gordon equation. The coupling term modifies these equations like (in purple) [119],

$$\nabla \cdot \mathbf{E} = \frac{\rho}{\epsilon_0} \quad \Longrightarrow \quad \nabla \cdot \mathbf{E} = g_{a\gamma\gamma} \nabla\phi \cdot \mathbf{B}, \tag{6.14a}$$

$$\nabla \cdot \mathbf{B} = 0 \quad \Longrightarrow \quad \nabla \cdot \mathbf{B} = 0, \tag{6.14b}$$

$$\nabla \times \mathbf{E} = -\frac{\partial \mathbf{B}}{\partial t} \quad \Longrightarrow \quad \nabla \times \mathbf{E} = -\frac{\partial \mathbf{B}}{\partial t}, \tag{6.14c}$$

$$\nabla \times \mathbf{B} = \mu_0 \mathbf{j} + \frac{\partial \mathbf{E}}{\partial t} \quad \Longrightarrow \quad \nabla \times \mathbf{B} = g_{a\gamma\gamma} \left[\mathbf{E} \times \nabla\phi - \mathbf{B}\frac{\partial \phi}{\partial t} \right] + \frac{\partial \mathbf{E}}{\partial t}, \tag{6.14d}$$

$$\Box\, \phi = 0 \quad \Longrightarrow \quad \Box\, \phi = -g_{a\gamma\gamma} \mathbf{E} \cdot \mathbf{B}, \tag{6.14e}$$

where $\Box \equiv \partial_\mu \partial^\mu$ is the d'Alembert operator, ϵ_0 and μ_0 the vacuum permittivity and permeability respectively. If we take the curl of Eq. (6.14c) and Eq. (6.14d), for the Maxwell's equations in vacuum (left side), we arrive at free wave equations for **E** and **B**. If we do the same for the coupled equations (right side) and neglect second order derivatives of ϕ we obtain [119]

$$\Box \mathbf{E} = 0 \quad \Longrightarrow \quad \Box \left[\mathbf{E} + \frac{1}{2} g_{a\gamma\gamma} \phi \mathbf{B} \right] = \frac{1}{2} g_{a\gamma\gamma} \phi \Box \mathbf{B}, \tag{6.15a}$$

$$\Box \mathbf{B} = 0 \quad \Longrightarrow \quad \Box \left[\mathbf{B} - \frac{1}{2} g_{a\gamma\gamma} \phi \mathbf{E} \right] = -\frac{1}{2} g_{a\gamma\gamma} \phi \Box \mathbf{E}. \tag{6.15b}$$

Suppose that during the propagation of the CMB photon from the LSS to us, the ALP field value changes in time and space slowly enough compared to the frequency of the photon. Then, at lowest order of perturbation, the right hand side of Eq. (6.15a) and Eq. (6.15b) are negligible and thus the combinations $\mathbf{E} + g_{a\gamma\gamma}\phi\mathbf{B}/2$ and $\mathbf{B} - g_{a\gamma\gamma}\phi\mathbf{E}/2$ are now the ones satisfying free wave equations. What this implies is that, as the axion field changes in value $\Delta\phi$ along the trajectory of an electromagnetic wave, **E** and **B** rotate by an angle $\Delta\Phi$ given by

$$\Delta\Phi = \frac{1}{2} g_{a\gamma\gamma} \Delta\phi. \tag{6.16}$$

A common heuristic given in the literature is that a change on the axion field makes the phase velocities of right- and left-handed states of photons different, and thus linearly polarized light (which consists on both states superposed) changes its polarization plane. However, I hope that the above derivation clarified the origin of cosmic birefringence and how it does not require introducing circular polarization to be understood.

If we substitute the expression of $g_{a\gamma\gamma}$ in terms of the anomaly coefficient Eq. (3.22) and suppose that axion domain walls have existed from the time of recombination to the present, then the net rotation of the polarization is

$$\Delta\Phi(\Omega) \simeq 0.42 c_\gamma \left(\frac{\phi_{\text{today}} - \phi_{\text{LSS}}(\Omega)}{2\pi f_a} \right) \ [\text{deg}], \tag{6.17}$$

where ϕ_{today} and ϕ_{LSS} are the axion field values at the solar system today and at the LSS respectively, and Ω the angular direction in by polar coordinates. A natural expectation for the anomaly coefficient is $c_\gamma \sim \mathcal{O}(1)$, but in principle it can be an arbitrary number. If c_γ is very large, strong electromagnetic effects occur on astronomical scales irrespective of the value of f_a, provided the involved axion field is massless or extremely light [119].

The isotropic cosmic birefringence angle β can be obtained by integrating Eq. (6.17) across the sky

$$\beta = \frac{1}{4\pi}\int \mathrm{d}\Omega\, \Delta\Phi(\Omega). \tag{6.18}$$

We measure CMB polarization through the Stokes parameters, and then we can compute the E (parity-even) and B (parity-odd) modes from those. Let us denote with a prime the values of the power spectrum coefficients after the cosmic birefringence rotation. The TE, EE and BB power spectra are parity-even. Their values change with cosmic birefringence as [124]

$$C_l'^{TE} = C_l^{TE}\cos(2\beta), \tag{6.19a}$$

$$C_l'^{EE} = C_l^{EE}\cos^2(2\beta) + C_l^{BB}\sin^2(2\beta), \tag{6.19b}$$

$$C_l'^{BB} = C_l^{BB}\cos^2(2\beta) + C_l^{EE}\sin^2(2\beta). \tag{6.19c}$$

However, these changes are hard to detect since the power spectra before the rotation are nonzero. The TB and EB power spectra are parity-odd. If parity is not violated in the temperature distribution at recombination, then TB and EB power spectra are zero before the rotation, but afterwards their values become

$$C_l'^{TB} = C_l^{TE}\sin(2\beta), \tag{6.20a}$$

$$C_l'^{EB} = \frac{1}{2}(C_l^{EE} - C_l^{BB})\sin(4\beta). \tag{6.20b}$$

Thus, a measurement of nonzero TB or EB would imply nonzero isotropic cosmic birefringence. One major challenge comes from detector calibration, as miscalibration of the polarization detectors can also result in nonzero EB, as well as from the foreground contribution. After taking those into account, the current observational value is [152]

$$\beta = 0.30 \pm 0.11 \text{ [deg]}. \tag{6.21}$$

If the axion field ϕ varies in value along the LSS, then the rotation of polarization $\Delta\Phi$ will also vary depending on the angle. This phenomenon is called anisotropic cosmic birefringence. Let us define the anisotropic part of the rotation of the polarization

$$\Delta\tilde{\Phi} \equiv \Delta\Phi - \beta. \tag{6.22}$$

We can expand $\Delta\tilde{\Phi}$ in spherical harmonics,

$$\tilde{\Phi}_{lm} = \int \mathrm{d}\Omega\, \Delta\tilde{\Phi}(\Omega) Y_{lm}^*(\Omega), \tag{6.23}$$

and define the power spectrum as usual

$$\langle \tilde{\Phi}^*_{lm} \tilde{\Phi}_{l'm'} \rangle = \delta_{ll'} \delta_{mm'} C_l^{\Phi\Phi}. \tag{6.24}$$

The power spectrum coefficients are correlated to β as [147]

$$C_l^{\Phi\Phi} \propto \beta^2. \tag{6.25}$$

To compute this power spectrum, first a self-calibration is performed. That is, β is obtained so that TB and EB power spectra are minimized, and then this value is subtracted. The polarization maps become sensitive just to anisotropic rotations. The current best bound is from the BICEP/Keck collaboration [136]

$$\frac{l(l+1)C_l^{\Phi\Phi}}{2\pi} \leq 0.014 \text{ [deg}^2\text{]}. \tag{6.26}$$

6.2.4 CB induced by a stable DW network

If a domain wall network is present at recombination, that means that the value of the field along the LSS varies in a predictable way. For this to be cosmologically viable, we need to be within the white region of Fig. 3.5, or otherwise a stable domain wall network would dominate the energy contents of the universe, or would have been measured already. Our results in Ch. 5 are important here—even if a bias is present, the network will not decay and the amount of domain walls per horizon will not change significatively.

The angle shift along a certain line of sight Ω just depends on which vacuum the axion field was at that angle in the LSS. $\Delta\Phi = 0$ if the vacuum at that angle in the LSS is the same as ours, $\Delta\Phi = c_\gamma \alpha_{\text{EM}}$ if the vacuum is different from ours. If we average over the whole space, the result is nonzero,

$$\beta = \frac{1}{2} c_\gamma \alpha_{\text{EM}} \approx 0.21 c_\gamma \text{ [deg]}. \tag{6.27}$$

For $c_\gamma \sim \mathcal{O}(1)$ this value is very close to the current experimental value Eq. (6.21).

The calculation of the anisotropic cosmic birefringence is a bit more involved. We can map the reduced power spectrum of domain walls $\mathcal{P}(k)$ obtained in Ch. 4 to $C_l^{\Phi\Phi}$ via the flat-sky approximation [125],

$$\frac{\sqrt{l(l+1)}}{d_L} \longleftrightarrow k, \tag{6.28a}$$

$$\frac{l(l+1)C_l^{\Phi\Phi}}{2\pi\beta^2} \longleftrightarrow \frac{\mathcal{P}(k)}{\eta^2}, \tag{6.28b}$$

where d_L is the comoving distance to the LSS and η is the axion field VEV. Our previous results for the domain wall power spectrum, with the corresponding mapped l and $C_l^{\Phi\Phi}$ are shown in Fig. 6.4. The predicted $C_l^{\Phi\Phi}$ for each l for a scale invariant domain wall network can be seen from the values taken in the right y axis by the red line. The prediction is barely above the experimental bound (black line with arrow), but let us keep in mind that this power spectrum is for an unbiased network. For a bias $\mathcal{O}(1)$ the predicted $C_l^{\Phi\Phi}$ is reduced.

The measurements of the isotropic and anisotropic cosmic birefringences will improve considerably in next-generation experiments. As we can see in Fig. 6.4, CMB-S4 [130], the Simons Observatory [132], PICO [133], and LiteBIRD [134] all are expected to have enough sensitivity to check whether the anisotropic cosmic birefringence matches the prediction considering a stable scale invariant domain wall network. The literature has boomed recently, with many other papers considering the expected cosmic birefringence by different kinds of axion fields [142, 145, 146, 148, 150, 153, 155] as well as axion strings [144, 149, 151, 156].

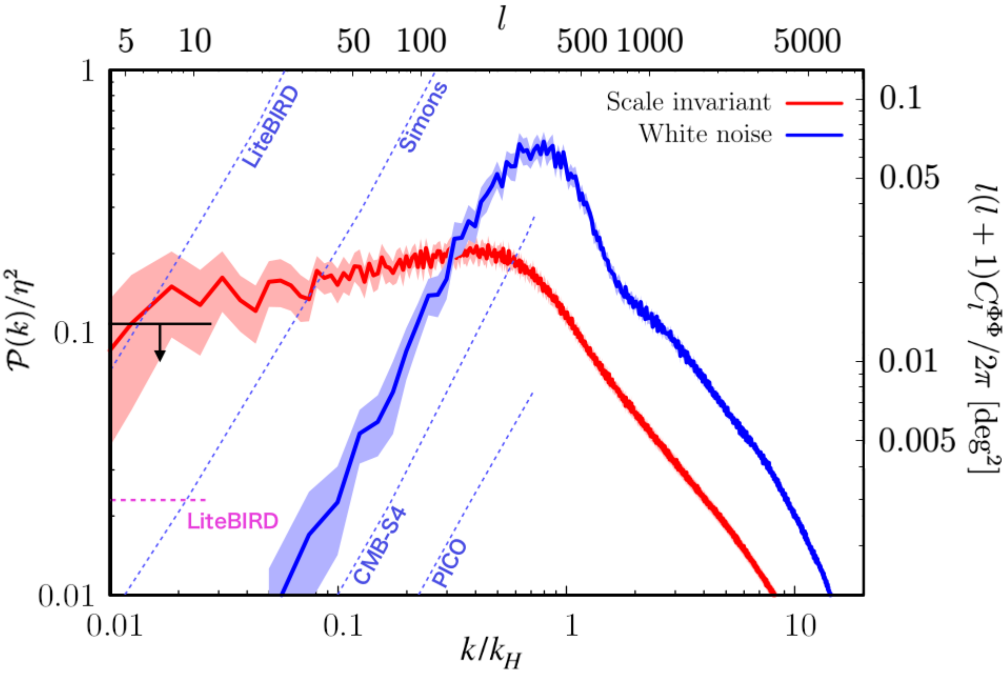

FIGURE 6.4: Reduced power spectrum of the scalar field at $\tau = 10/m$ with scale invariant (red) and white noise (blue) initial conditions in the absence of bias. In addition to what we had shown in Fig. 4.4, the multipole l and the angular power spectrum $l(l+1)C_l^{\Phi\Phi}/2\pi$ in the flat-sky approximation [125] of the anisotropic cosmic birefringence induced by axion domain walls are also shown. The horizontal solid black line shows the current $C_l^{\Phi\Phi}$ bound by BICEP/Keck [128]. Oblique discontinuous lines in blue correspond to the expected 1σ statistical uncertainties (i.e. experimental noise) for next generation experiments, supposing a white noise power spectrum. The horizontal discontinuous line in pink is the uncertainty for LiteBIRD supposing a scale invariant spectrum. Uncertainties for Simons, CMB-S4 and PICO are all past the plot axis limits and below that of LiteBIRD, thus all four next-generation experiments would be able to probe the predicted anisotropic cosmic birefringence. Uncertainties adapted from [143].

Chapter 7

Summary

Historically, the study of domain walls has been neglected in comparison to the other types of defects. Seen as an undesirable aspect of the models, most of the literature up until now has revolved around finding ways of making domain walls decay. However, decaying domain walls have their own set of challenges and it is nontrivial to make convincing models following that route. Axiverse predicts hundreds of axion fields, of which several could form domain walls after inflation. Depending on the particulars of the underlying string theory, consequences of their decay (particle and gravitational wave production) or their stability (energy domination, cosmic birefringence) could add up.

The monograph by Vilenkin and Shellard is now more than 20 years old, and with no other reviews on the subject, reading through domain wall literature can feel like navigating a labyrinth of assumptions and different model quirks that leaves the reader wondering to which extent each result can be used in conjunction to the others. One of my objectives with this thesis was presenting, in my opinion, a well needed English review of the field, hopefully laying the foundations upon which modern studies of domain walls can be built on.

We have showed how many of the established truths in the field were wrong or vastly incomplete. First of all, percolation theory is not an apt method to study biased networks analytically. The scaling solution does not just appear from domain wall annihilation and the existence of a causal horizon, it appears as a result of a careful balance between the universe expansion and an annihilation rate which depends on the fluctuations at superhorizon scales. That is to say, it was thought that the existence of an attractor solution meant that initial conditions were quickly forgotten, but we saw that the initial conditions leave a characteristic imprint on the network dynamics and on the details of the attractor solution itself. The Kibble mechanism is insufficient to argue for the causal inevitability of the formation of domain wall networks in the cosmological context. Furthermore, the details of domain wall formation depend heavily on the initial condition power spectrum and overall population bias. For large superhorizon fluctuations (spectral index n close or lower than zero, i.e. scale invariant) the networks are exceptionally stable, thanks to the presence of voids spanning multiple horizons in size. The presence of an overall population bias affects those networks by inhibiting domain wall formation in the first place, more than by making it decay afterwards.

Within the field of subdominant domain walls, there are various plausible research lines after our findings. One could search for mechanisms that induce domain wall decay even with inflationary initial conditions (e.g. a potential bias), inhibit the undesirable consequences of a stable network (e.g. dynamic ways of keeping all pseudoscalar field masses low) or avoid their formation altogether (e.g. mechanisms to drive the domain wall formation period prior to inflation).

On the other hand, the recent surge of hints for anisotropy at cosmological scales gives a riskier but nevertheless interesting research line in studying the universe dynamics. That is, universe dynamics under some cases of domain wall dominance (e.g. a locally dominating but very sparse network, or a network which dominated in the past but that became subdominant later on). It seems like non-FLRW and anisotropic cosmology will be a key research line going forward, so it is reasonable to think that domain walls may play their role in there as well.

From the various novel results in this thesis, I would like to emphasize two of them. First, if domain walls form after inflation, they are very resilient to population biases. Secondly, a subdominant stable domain wall network is a cosmologically viable explanation for the current observed hint of isotropic cosmic birefringence and is within observational bounds for the anisotropic cosmic birefringence.

The direct search for dark matter and axions has received few positive results despite sustained efforts. This leads me to believe that the next hint for axion physics will probably be found elsewhere. The physics behind the CMB B modes is fascinating and next generation experiments like CMB-S4, the Simons Observatory, PICO and LiteBIRD are expected to vastly improve our current knowledge. If primordial B-modes are convincingly detected, then funding for CMB polarization experiments will further increase. The current hint for isotropic cosmic birefringence points to the existence of parity-violating interactions. An improvement of both isotropic and anisotropic measurements will put additional constraints onto the axion model parameter space, which could in turn guide future axion direct detection experiments.

Acknowledgements

I want to thank my supervisor, Fuminobu Takahashi, for the brilliant insights and careful guidance which he has given me during this thesis. I also want to thank my other research colleagues, Wen Yin and Naoya Kitajima. This work was supported by the MEXT scholarship grant number 203069.

Appendix A

Scalar field fluctuations during inflation

Inflationary theories are a well motivated class of beyond the standard model theories, presenting a plausible solution for the flatness problem, the horizon problem and the exotic relic problem, and realizing dynamically the cosmological principle. One of the most interesting features of inflation is that it predicts the generation of scale invariant power spectrums for the density perturbations, the inflaton field perturbations as well as the perturbations of other scalar fields. Even though the theory was not engineered for it, this explains the almost scale invariant density perturbation spectrum seen in CMB observations [26].

In this thesis we have studied the properties and dynamics of domain wall networks generated from a scale invariant power spectrum. In this annex we will derive how this scale invariant spectrum of perturbations is generated on a scalar field quantized on the de Sitter background (i.e. in an universe with constant Hubble parameter H).

A.1 Action quadratic in the perturbations

We are interested in the perturbations a the scalar field which will later lead to domain wall network formation, e.g. an axion/ALP field. Let us call this field ϕ and its potential, $V(\phi)$. Its action is,

$$S = \int \mathrm{d}^4x \sqrt{-g} \left[\frac{1}{2} g^{\mu\nu} \partial_\mu \phi \partial_\nu \phi - V(\phi) \right], \tag{A.1}$$

where $g \equiv \det(g_{\mu\nu})$. When evaluating it on the unperturbed FLRW metric,

$$S = \int \mathrm{d}^4x \left[\frac{1}{2} a^2 \left((\phi')^2 - (\nabla\phi)^2 \right) - a^4 V(\phi) \right], \tag{A.2}$$

where the prime denotes derivatives with respect to conformal time τ. In a general case we would have to consider coupled fluctuations of the field $\delta\phi$ and the metric $\delta g_{\mu\nu}$. Axion fields of our interest (i.e. ones that do not lead to domain wall domination) have subdominant energy and thus their effect on the metric is negligible. Let us write the scalar field values ϕ as their average $\bar{\phi}$ plus perturbations around it $\delta\phi$. For convenience, let us define f as

$$f(\tau, \mathbf{x}) \equiv a(\tau)\delta\phi(\tau, \mathbf{x}), \tag{A.3}$$

and thus

$$\phi(\tau, \mathbf{x}) = \bar{\phi}(\tau) + \frac{f(\tau, \mathbf{x})}{a(\tau)}. \tag{A.4}$$

To study the linearised dynamics of ϕ, we need the action at quadratic order in fluctuations. We can substitute this into the scalar field action and keep only the terms quadratic in f,

$$S \simeq \frac{1}{2} \int \mathrm{d}^4x \left[(f')^2 - (\nabla f)^2 - 2Hff' + \left(H^2 - a^2 \frac{\partial^2 V}{\partial \phi^2} \right) f^2 \right]. \tag{A.5}$$

If we integrate the ff' term by parts,

$$S \simeq \frac{1}{2} \int \mathrm{d}^4x \left[(f')^2 - (\nabla f)^2 + \left(\frac{a''}{a} - a^2 \frac{\partial^2 V}{\partial \phi^2} \right) f^2 \right]. \tag{A.6}$$

In the de Sitter background, $H =$ constant, $a \propto e^{Ht}$ and

$$\frac{a''}{a} \simeq \frac{2a'aH}{a} = 2a^2H^2 = \frac{2}{\tau^2}. \tag{A.7}$$

The axion mass is protected by its shift symmetry, so it is assumed to be very light. Since its mass is much smaller than the Hubble parameter, we can see how the $a^2\partial^2 V/\partial\phi^2$ term is subdominant,

$$a^2 \left| \frac{\partial^2 V}{\partial \phi^2} \right| \simeq \frac{m}{H^2\tau^2} \ll \frac{2}{\tau^2}. \tag{A.8}$$

With these, the action simplifies to

$$S \simeq \int \mathrm{d}^4x \frac{1}{2} \left[(f')^2 - (\nabla f)^2 + \frac{a''}{a} f^2 \right]. \tag{A.9}$$

The above action implies the following equation of motion, called the Mukhanov-Sasaki equation (MS equation)

$$f_k'' + \omega_k^2(\tau) f_k = 0, \tag{A.10}$$

where

$$\omega_k^2(\tau) \equiv k^2 - \frac{a''}{a}, \qquad k \equiv |k|. \tag{A.11}$$

In the de Sitter background (i.e. substituting Eq. (A.7)), the frequencies take the following form

$$\omega_k^2(\tau) = k^2 - \frac{2}{\tau^2}. \tag{A.12}$$

A.2 Canonical quantization of the scalar field

Let us perform the canonical quantization of the scalar field in the Heisenberg picture, where operators vary in time while states are time-independent. The momentum conjugate to f is

$$\pi \equiv \frac{\partial \mathcal{L}}{\partial f'} = f' \tag{A.13}$$

First, we promote the fields $f(\tau, \mathbf{x})$ and $\pi(\tau, \mathbf{x})$ to quantum operators, $\hat{f}(\tau, \mathbf{x})$ and $\hat{\pi}(\tau, \mathbf{x})$. The operators satisfy the following commutation relation at equal times

$$[\hat{f}(\tau, \mathbf{x}), \hat{\pi}(\tau, \mathbf{y})] = i\delta^{(3)}(\mathbf{x} - \mathbf{y}). \tag{A.14}$$

The delta function is a signature of locality, it implies that modes at different points in space are independent and thus their operators commute. If we Fourier transform Eq. (A.14) we find a similar expression but for the wavenumbers,

$$[\hat{f}_{\mathbf{k}}(\tau), \hat{\pi}_{\mathbf{q}}(\tau)] = i\delta^{(3)}(\mathbf{k} - \mathbf{q}). \tag{A.15}$$

Let us now write the operator $\hat{f}$ in terms of its corresponding creation and annihilation operators $\hat{a}^\dagger$ and $\hat{a}$,

$$\hat{f}_{\mathbf{k}}(\tau) = f_k(\tau)\hat{a}_{\mathbf{k}} + f_k^*(\tau)\hat{a}_{\mathbf{k}}^\dagger. \tag{A.16}$$

$f_k(t)$ and $f_k^*(t)$ are called the mode functions and they are two linearly independent solutions of the MS equation. Since the frequencies $\omega_k(t)$, as defined in Eq. (A.12), only depend on k, the mode functions are direction independent as well. The creation and annihilation operators $\hat{a}$ and $\hat{a}^\dagger$ are, in general, direction dependent.

In order to obtain the normalization of the mode functions we substitute Eq. (A.16) into Eq. (A.15), which yields

$$W[f_k] \times [\hat{a}_{\mathbf{k}}, \hat{a}_{\mathbf{q}}^\dagger] = \delta^{(3)}(\mathbf{k} - \mathbf{q}), \tag{A.17}$$

where we have defined the Wronskian $W[f_k]$ as

$$W[f_k] = -i(f_k \dot{f}_k^* - \dot{f}_k f_k^*). \tag{A.18}$$

We can choose to normalize f_k such that $W[f_k] \equiv 1$, and thus Eq. (A.17) becomes

$$[\hat{a}_{\mathbf{k}}, \hat{a}_{\mathbf{q}}^\dagger] = \delta^{(3)}(\mathbf{k} - \mathbf{q}). \tag{A.19}$$

The quantum states in the Hilbert space are constructed by defining the vacuum state $|0\rangle$ via

$$\hat{a}_{\mathbf{k}} |0\rangle = 0, \quad \forall \mathbf{k}, \tag{A.20}$$

and by producing excited states through the application of creation operators $\hat{a}^\dagger$.

A.3 The vacuum state, initial conditions and mode functions

In order to define the vacuum state we need to fix the mode functions. Although in general this is ambiguous, in the case of the de Sitter background there is a preferred choice. Since at sufficiently early times all modes of cosmological interest were deep inside the horizon, their wavenumbers were large and thus their associated frequencies Eq. (A.12) were time-independent,

$$\omega_k^2(\tau) \simeq k^2 - \frac{2}{\tau^2} \longrightarrow k^2, \tag{A.21}$$

and thus Eq. (A.10) reduces to the equation for a free field in Minkowski space,

$$f_k'' + k^2 f_k \simeq 0. \tag{A.22}$$

This has two independent solutions in the form of plane waves of frequency k

$$f_k(\tau) \propto e^{\mp ik\tau}. \tag{A.23}$$

Only the positive frequency mode (the minus sign on the above equation) corresponds to the ground state of the Hamiltonian. This corresponds to the following initial condition

$$\lim_{\tau\to-\infty} f_k(\tau) = \frac{1}{\sqrt{2k}} e^{-ik\tau}, \tag{A.24}$$

which defines a preferable set of mode functions as well as an unique physical vacuum, called the Bunch-Davies vacuum.

The MS equation on the de Sitter background,

$$f_k''(\tau) + \left(k^2 - \frac{2}{\tau^2}\right) f_k(\tau) = 0. \tag{A.25}$$

has the following exact solution,

$$f_k(\tau) = \alpha \frac{e^{-ik\tau}}{\sqrt{2k}} \left(1 - \frac{i}{k\tau}\right) + \beta \frac{e^{ik\tau}}{\sqrt{2k}} \left(1 + \frac{i}{k\tau}\right), \tag{A.26}$$

where α and β are constants determined by the initial conditions. Taking the limit for $\tau \to -\infty$ and comparing the result to Eq. (A.24) gives $\alpha = 1$ and $\beta = 0$, and thus the mode function becomes

$$f_k(\tau) = \frac{e^{-ik\tau}}{\sqrt{2k}} \left(1 - \frac{i}{k\tau}\right). \tag{A.27}$$

A.4 Power spectrum of scalar fluctuations

We are interested in the quantum statistics of $\hat{f}(\tau, \mathbf{x})$,

$$\hat{f}(\tau, \mathbf{x}) = \int \frac{\mathrm{d}^3 k}{(2\pi)^{3/2}} \left[f_k(\tau) \hat{a}_{\mathbf{k}} + f_k^*(\tau) \hat{a}_{\mathbf{k}}^\dagger \right] e^{i\mathbf{k}\cdot\mathbf{x}}. \tag{A.28}$$

Its expectation value vanishes,

$$\langle \hat{f} \rangle \equiv \langle 0 | \, \hat{f} \, | 0 \rangle = 0. \tag{A.29}$$

However, its variance is nonzero due to quantum fluctuations,

$$\begin{aligned} \langle | \hat{f} | \rangle &\equiv \langle 0 | \, \hat{f}^\dagger(\tau, \mathbf{0}) \hat{f}(\tau, \mathbf{0}) \, | 0 \rangle \\ &= \int \frac{\mathrm{d}^3 k}{(2\pi)^{3/2}} \int \frac{\mathrm{d}^3 q}{(2\pi)^{3/2}} \langle 0 | \, (f_k^*(\tau) \hat{a}_{\mathbf{k}}^\dagger + f_k(\tau) \hat{a}_{\mathbf{k}})(f_q(\tau) \hat{a}_{\mathbf{q}} + f_q^*(\tau) \hat{a}_{\mathbf{q}}^\dagger) \, | 0 \rangle \\ &= \int \mathrm{d}^3 k \int \mathrm{d}^3 q \frac{1}{(2\pi)^3} f_k(\tau) f_q^*(\tau) \, \langle 0 | \, [\hat{a}_{\mathbf{k}}, \hat{a}_{\mathbf{q}}^\dagger] \, | 0 \rangle \\ &= \int \mathrm{d}^3 k \, \frac{|f_k(\tau)|^2}{(2\pi)^3} = \int \mathrm{d} \ln k \, \frac{k^3 |f_k(\tau)|^2}{2\pi^2} \equiv \int \mathrm{d} \ln k \, \mathcal{P}_f(k, \tau) \end{aligned} \tag{A.30}$$

where we have defined the reduced power spectrum of scalar field fluctuations $\mathcal{P}_{\delta\phi}$ as in Eq. (4.6) and, since $\delta\phi = f/a$,

$$\mathcal{P}_f(k, \tau) \equiv a^2 \mathcal{P}_{\delta\phi}(k, \tau). \tag{A.31}$$

If we substitute the mode function Eq. (A.27) we find that the reduced power spectrum of fluctuations of a quantum scalar field during inflation is

$$\mathcal{P}_{\delta\phi}(k, \tau) = \left(\frac{H}{2\pi} \right)^2 \left(1 + \left(\frac{k}{aH} \right)^2 \right). \tag{A.32}$$

The second term in Eq. (A.32) becomes negligible soon after the horizon crossing $k = aH$. Thus, we approximate the shape of the reduced power spectrum at horizon crossing by this asymptotic value, evaluated at $k = aH$,

$$\mathcal{P}_{\delta\phi}(k, \tau) \simeq \left(\frac{H}{2\pi} \right)^2 \Bigg|_{k=aH} \tag{A.33}$$

Different modes exit the horizon at slightly different times. In a realistic case, the background is quasi-de Sitter, which means that H varies slightly during inflation, implying that the spectrum will not be exactly scale invariant but it will have a slight tilt with k. However, for our purposes, considering it scale invariant is a very good approximation.

Appendix B

The lattice simulation

Cosmological lattice simulations solve for the evolution of the scalar field in discretized time and space intervals. In Sec. B.1 we will derive the scalar field equation of motion in the expanding universe and in Sec. B.2 we convert it to program variables and see how it can be solved in discretized timesteps. In Sec. B.3 we explain how the normalized domain wall length is calculated.

B.1 Scalar field equation of motion

The action of a scalar field ϕ is,

$$S = \int \mathrm{d}^4x\sqrt{-g}\left(\frac{1}{2}g^{\mu\nu}\partial_\mu\phi\partial_\nu\phi - V(\phi)\right), \tag{B.1}$$

where g is the metric determinant. Let us calculate its variation δS with respect to $\delta\phi$,

$$\begin{aligned}\delta S &= \int \mathrm{d}^4x\sqrt{-g}\left[\delta\left(\frac{1}{2}g^{\mu\nu}\partial_\mu\phi\partial_\nu\phi\right) - \delta V(\phi)\right]\\ &= \int \mathrm{d}^4x\sqrt{-g}\left[\frac{1}{2}g^{\mu\nu}\delta\left(\partial_\mu\phi\partial_\nu\phi\right) - \frac{\partial V(\phi)}{\partial\phi}\delta\phi\right]\\ &= \int \mathrm{d}^4x\sqrt{-g}\left[g^{\mu\nu}\partial_\mu(\delta\phi)\partial_\nu\phi - \frac{\partial V(\phi)}{\partial\phi}\delta\phi\right]\\ &= \int \mathrm{d}^4x\left[\underbrace{\partial_\mu(\sqrt{-g}g^{\mu\nu}\delta\phi\partial_\nu\phi)}_{\text{total derivative }\to\text{ }0} - \delta\phi\partial_\mu(\sqrt{-g}g^{\mu\nu}\partial_\nu\phi) - \sqrt{-g}\frac{\partial V(\phi)}{\partial\phi}\delta\phi\right]\\ &= -\int \mathrm{d}^4x\left[\partial_\mu(\sqrt{-g}g^{\mu\nu}\partial_\nu\phi) + \sqrt{-g}\frac{\partial V(\phi)}{\partial\phi}\right]\delta\phi\end{aligned} \tag{B.2}$$

where we have used that $g^{\mu\nu}$ is symmetric. We are interested in the extrema of δS when varying with respect to $\delta\phi$, for which the term within brackets must be zero $\forall\phi$,

$$\frac{1}{\sqrt{-g}}\partial_\mu(\sqrt{-g}g^{\mu\nu}\partial_\nu\phi) + \frac{\partial V(\phi)}{\partial\phi} = 0. \tag{B.3}$$

If $g_{\mu\nu} = \eta_{\mu\nu}$ the Minkowski metric and $V(\phi)$ a quartic potential, then we just reach the usual Klein-Gordon equation. The leftmost term in Eq. (B.3) is usually called the Laplace-Bertrani operator $\nabla_\mu\nabla^\mu\phi \equiv \partial_\mu(\sqrt{-g}g^{\mu\nu}\partial_\nu\phi)/\sqrt{-g}$ and is the generalization of the d'Alembertian $\Box \equiv \partial_\mu\partial^\mu$ for a general metric space.

The FLRW metric in our chosen metric signature, is

$$g_{\mu\nu} = \begin{pmatrix} 1 & 0 & 0 & 0 \\ 0 & -a^2 & 0 & 0 \\ 0 & 0 & -a^2 & 0 \\ 0 & 0 & 0 & -a^2 \end{pmatrix}, \qquad g^{\mu\nu} = \begin{pmatrix} 1 & 0 & 0 & 0 \\ 0 & -1/a^2 & 0 & 0 \\ 0 & 0 & -1/a^2 & 0 \\ 0 & 0 & 0 & -1/a^2 \end{pmatrix}, \tag{B.4}$$

thus $g = -a^6$ and $\sqrt{-g} = a^3$. Let us separate temporal and spatial components in Eq. (B.3)

$$\frac{1}{a^3}\partial_t(a^3\partial_t\phi) - \frac{1}{a^3}\partial_i\left(a^3\frac{1}{a^2}\partial_i\phi\right) + \frac{\mathrm{d}V(\phi)}{\mathrm{d}\phi} = 0, \tag{B.5}$$

where t is the (physical) time component and i the three spatial (comoving) components. Notating time derivatives as

$$\frac{\mathrm{d}\bigcirc}{\mathrm{d}t} \equiv \dot{\bigcirc}, \tag{B.6}$$

we reach the final expression for the equation of motion (EOM),

$$\ddot{\phi} + 3\frac{\dot{a}}{a}\dot{\phi} - \frac{1}{a^2}\nabla^2\phi + \frac{\mathrm{d}V(\phi)}{\mathrm{d}\phi} = 0. \tag{B.7}$$

B.2 Time and space discretization

B.2.1 Program variables

Floating point errors can be minimized if quantities in the program do not vary wildly in order of magnitude. Thus, program variables are normalized to make them dimensionless and of order 1. Let us use the subindex pr to indicate program variables. Let us define the rescaled variables as

$$\phi_{\mathrm{pr}} \equiv Aa^r\phi, \qquad \vec{x}_{\mathrm{pr}} \equiv B\vec{x}, \qquad \mathrm{d}t_{\mathrm{pr}} \equiv Ba^s\mathrm{d}t, \tag{B.8}$$

where the rescaling coefficients are A, B, r and s. If we substitute in Eq. (B.7) and go from physical to program time derivatives (notated with a prime) we get,

$$\phi''_{\mathrm{pr}} + (s-2r+3)\frac{a'}{a}\phi'_{\mathrm{pr}} - a^{-2s-2}\nabla^2_{\mathrm{pr}}\phi_{\mathrm{pr}} - \left[r(s-r+2)\left(\frac{a'}{a}\right)^2 + r\frac{a''}{a}\right]\phi_{\mathrm{pr}} + \frac{\mathrm{d}V_{\mathrm{pr}}}{\mathrm{d}\phi_{\mathrm{pr}}} = 0, \tag{B.9}$$

where the program potential is defined as

$$V_{\mathrm{pr}} \equiv \frac{A^2}{B^2}a^{-2s+2r}V. \tag{B.10}$$

This reveals something very interesting: if we choose the rescalings so that

$$s \equiv 2r - 3, \tag{B.11}$$

then the term with the first derivative of the field will vanish, which is beneficial for the computation of the field evolution. This technique was first introduced to cosmological lattice simulations by the LATTICEEASY code [158].

A dominant potential term of the form

$$V = \frac{C}{n}\phi^n, \tag{B.12}$$

enters the equation of motion as

$$\frac{\mathrm{d}V_{\mathrm{pr}}}{\mathrm{d}\phi_{\mathrm{pr}}} = \underbrace{CA^{2-n}B^{-2}}_{\equiv 1} a^{\overbrace{-2s + r(2-n)}^{\equiv 0}} \phi^{n-1}. \tag{B.13}$$

In order to simplify it as much as possible, the braced terms are set to 1 and 0 respectively. We are still free to choose either A or B however we want. If we set $A = 1/\eta$, where η is the field VEV, then considering all of the aforementioned conditions, the rescaling coefficients become,

$$A = \frac{1}{\eta}, \qquad B = \sqrt{C}\eta^{-1+n/2}, \qquad r = \frac{6}{2+n}, \qquad s = 3\frac{2-n}{2+n}. \tag{B.14}$$

In this thesis we have studied the double well potential,

$$V = \frac{1}{4}\lambda(\phi^2 - \eta^2)^2, \tag{B.15}$$

in which case $C = \lambda$ and $n = 4$. For those,

$$A = \frac{1}{\eta}, \qquad B = \sqrt{\lambda}\eta = m, \qquad r = 1, \qquad s = -1, \tag{B.16}$$

and then the equation of motion becomes,

$$\phi''_{\mathrm{pr}} - \frac{a''}{a}\phi_{\mathrm{pr}} - \nabla^2_{\mathrm{pr}}\phi_{\mathrm{pr}} + (\phi^2_{\mathrm{pr}} - a^2)\phi_{\mathrm{pr}} = 0. \tag{B.17}$$

Let us look again at the rescaled variables for our particular case,

$$\phi_{\mathrm{pr}} \equiv \frac{a}{\eta}\phi, \qquad \vec{x}_{\mathrm{pr}} \equiv m\vec{x}, \qquad \mathrm{d}t_{\mathrm{pr}} \equiv \frac{m}{a}a^s\mathrm{d}t. \tag{B.18}$$

Going through the A, B, r and s is useful if we are interested in a different potential, or if we want to make a code valid for any potential. Most importantly, I think that it is valuable to see why the ϕ'_{pr} term can be removed, and how it is not dependent on the potential choice. If one is just interested in quartic potentials, then building the code in terms of Eq. (B.17) and Eq. (B.18) is enough.

B.2.2 The staggered leapfrog method

We want to solve the differential equation in finite timesteps. In order to solve a second order in time equation for ϕ_{pr}, we need to store the value of ϕ_{pr} and its first time derivative $\phi'_{\rm pr}$ at each step, and then use those to calculate the values of $\phi''_{\rm pr}$.

There are many ways of proceeding. Symplectic integrators are interesting as they conserve the energy, but they can be slow. The staggered leapfrog method is a good balance between precision and speed, as it is faster but less precise than symplectic or Runge-Kutta methods. The idea of the staggered leapfrog method is to store in the code the values of the field and its derivatives at different times, separated by $\Delta t/2$, where Δt is the timestep. Schematically, the iterations look like,

$$\begin{aligned} \phi(t) &= \phi(t-\Delta t) + \Delta t\, \phi'(t-\Delta t/2), \\ \dot{\phi}(t+\Delta t/2) &= \dot{\phi}(t-\Delta t/2) + \Delta t\, \phi''[\phi(t)], \\ \phi(t+\Delta t) &= \phi(t) + \Delta t\, \phi'(t+\Delta t/2), \\ &\dots \end{aligned} \tag{B.19}$$

where pr subindices have been ommitted for simplicity. This method relies on being able to calculate the second derivative of the field in terms of the field $\phi''[\phi(t)]$. Accuracy and stability are lost if ϕ'' also depends on ϕ', which is why we removed that term with the rescalings.

If the timestep is too large, the integration will be unstable. The condition for the timestep is

$$\Delta t \ll \frac{1}{\sqrt{d}}\frac{N_H}{N_{\rm cell}}, \tag{B.20}$$

where d is the number of dimensions, N_H the number of Hubble horizons along one of the sides, and $N_{\rm cell}$ the number of field values taken per side. This condition is known as the Courant condition [158].

B.3 Normalized domain wall length

The definition of 2D normalized domain wall length is,

$$L = \frac{\text{Total physical DW length}}{{N_H}^2 H^{-1}}. \tag{B.21}$$

If this is written in terms of program variables, we get,

$$L = \frac{L_{\rm count} t_{\rm pr}}{N_{Hi} N_{\rm cell}}, \tag{B.22}$$

where N_{Hi} is the number of horizons along one side of the box at initial time, and $L_{\rm count}$ is a dimensionless number, the total domain wall length in the simulation taking one cell side as the unit length.

The estimation of $L_{\rm count}$ can be made pretty naively. We can just sweep through x and y directions, and add one to $L_{\rm count}$ each time contiguous values of the field ϕ change sign. In pseudocode, that is

```
for (0<x<Ncell) {
    for (0<y<Ncell) {
        if ( phi(x,y)*phi(x+1,y) < 0 ) Lcount++;
        if ( phi(x,y)*phi(x,y+1) < 0 ) Lcount++;
    }
}
```

This estimate can be improved by considering blocks of 4 field values instead of just 2. In the following figure, red means positive values and blue, negative values. The thick black line represents the domain wall. There are more possible combinations of positive and negative values, but there are only 4 possible contributions to L_{count}.

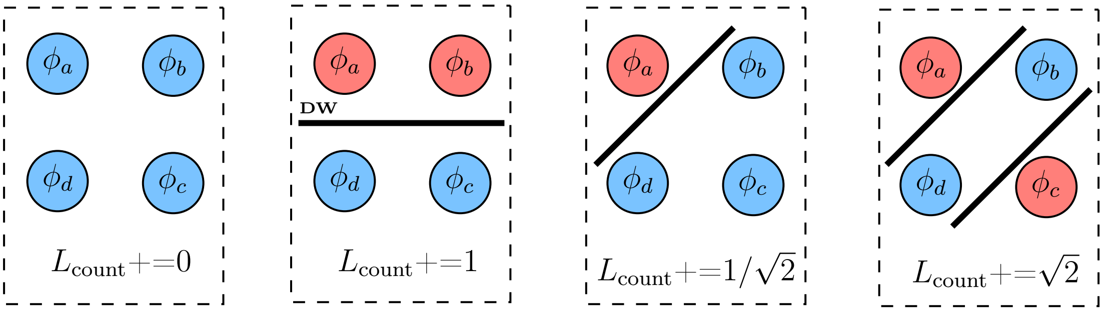

This computation can be done rather efficiently. In pseudocode,

```
for (0<x<Ncell) {
    for (0<y<Ncell) {
        a = phi(x,y);
        b = phi(x+1,y);
        c = phi(x+1,y+1);
        d = phi(x,y+1);
        if(a*b*c*d<0) Lcount += 1/sqrt(2);
        else if(a*c<0) Lcount += 1;
        else if(a*b<0) Lcount += sqrt(2);
    }
}
```

We could compute L_{count} more precisely, by interpolating the field values or by considering larger field value blocks. However, the above is precise enough for our purposes, at a small computational cost.

Appendix C

GPU-accelerated lattice simulations

In Ch. B we have seen how the evolution of a scalar field in an expanding universe can be solved by discretizing the problem in both space (lattice) and time (timesteps). The amount of hubble horizons that can be computed each time is limited by the grid size, which in turn is limited by the hardware. We have to run many simulations in order to have enough statistics, as well as to study the evolution under different initial conditions. Any code speedups will directly translate into better statistics and better granularity in the final data.

Using **parallel programming** for optimizing cosmological lattice simulations is an established practice [158, 160, 161, 162]. In this chapter I will explain the basics of both CPU and GPU parallelization as well as how my code improves on previous implementations for both the 2D and 3D cases.

Before continuing, let me do a brief summary of the speedups that I obtained in my laptop[1]. Compared to the single threaded code, GPU parallelized code ran ~ 100 times faster for the 2D case and ~ 200 times faster for the 3D case. 2D simulations (maximum grid size 31104^2) up to time $m\tau_{\text{end}} = 20$ take about 2 minutes and about 4 minutes for the 3D case (maximum grid size 960^3, $m\tau_{\text{end}} = 15$). The large granularity and high resolution obtained in the figures in Sec. 5.2 was thanks to these GPU acceleration techniques. If I had used single threaded code, it would have taken 4 years instead of the 2 weeks that were required.

C.1 GPU vs CPU parallel computing

The **central processing unit** (CPU) is the main component of a computer, being in charge of reading and writing data, performing logical operations and controlling all of the other components. Most modern computers have many CPUs, which are commonly called cores. Programs are broken down into processes, which in turn are composed of threads. Each core can take one thread at a time, and the data each thread operates on is independent. If a program is designed so that some or all of their threads can run at the same time (i.e. in parallel) the program's performance will increase.

The **graphics processing unit** (GPU) is a coprocessor present in most modern computers. With thousands of cores, arrays of data are processed simultaneously

---

[1] Intel i7-10875H @2.3GHz x16, NVIDIA GeForce RTX 2070m Super.

under the same instructions. This makes GPUs exceptionally good at image and video processing, thus their development was linked to video games and 3D rendering. Since the early 2000s, **general purpose programming in GPUs** (GPGPU) has been on the rise. As long as the program can be written in this "single instruction, multiple data" format, GPUs can be used to speed up applications, scientific simulations, artificial intelligence (AI), machine learning, cryptocurrency mining, etc.

CPU parallelization consists just on identifying which parts of the code can run in parallel (i.e. do not require previous data to run) and marking them as such. In this way, one can usually parallelize a serial code with relatively little restructuring. On the other hand, GPU parallelization usually requires restructuring the code. GPUs are incredibly fast at computing but comparatively slow at reading data, so designing the code usually revolves around minimizing read/write time and maximizing the memory bandwidths.

However, CPU parallelization is not all advantages. Dividing the program in more threads comes at a cost (overhead). Since the resources are all shared, switching between threads (context switching) requires some time. For $\mathcal{O}(10)$ cores the speedups are linear with the number of cores, but that scaling gets worse from $\mathcal{O}(50)$ and beyond, up to the point where adding more threads could even make the program slower. In a GPU, resources are partitioned so context switching is virtually free. Programs can be designed so that the slow read/write speeds (memory latency) are hidden under other calculations, making the speedup linear with the number of cores even for large GPU clusters.

A difference that is not usually emphasized, but that is important for simulations, is that modern (64 bit) computers are designed to perform operations at `double` precission while GPUs operate at `float` precission. Using `doubles` on current GPUs other than those from the NVIDIA Tesla series and higher will result in significant slowdowns.

The fixed pattern under which data are read is called a **stencil**, and simulations like cosmological lattice simulations form part of what are called **iterative stencil loops**. In our case, the stencil has $2N+1$ data points– the center value and its first neighbours N. The bigger the stencil gets, the more efficient GPU parallelization becomes. In the end, depending on the particulars of the code, the best method varies. Cosmological lattice simulations are best programmed for a GPU, since the same data instructions are run on millions of data points at a time.

As for how to implement each of this methods in a code, for CPU parallelization, the most commonly used library is MPI [166]. For GPU parallelization, CUDA [165] is the most popular language, although it is propietary software that only works with NVIDIA cards. For other brands, OpenCL is used [164] although as it is less specialized it is said to be less efficient.

C.2 Past published codes

The widely acclaimed **LATTICEEASY** [158] was released together with a MPI version called **CLUSTEREASY**. LATTICEEASY uses an order 1 stencil and a staggered leapfrog algorithm, which could be said to be a naive solution but it is good enough for many situations. The first GPGPU implementation of a lattice simulation was in 2009, called **CUDAEASY** [160]. To account for the decreased accuracy of GPU's floating point precission, it used a bigger, second order stencil [157]. Years later, the same author developed a Python implementation of this code, **PyCOOL** [161], now with a symplectic integrator to achieve better energy conservation. In 2017, Correia and Martins studied the main bottlenecks of an OpenCL implementation of the PRS algorithm [162]. Although the code was not named nor made public, we know from their findings that the main bottleneck is memory usage and that single precision is preferred over double for GPU simulations, as it is faster, less memory intensive and yields good enough results. Recently, the pseudolibrary **CosmoLattice** [163] was made public. It uses object oriented programming to completely separate the physics from its implementation and allows the user to run simulations with any number of coupled scalar and gauge fields. Its aim seems to be versatility more than speed, although it allows for MPI parallelization. My code uses an order 1 stencil and a staggered leapfrog algorithm, and is programmed in C++ and CUDA.

I cannot do a direct speed comparison with CUDAEASY nor PyCOOL since the codes are not available anymore, but in my laptop, a 3D simulation runs 200 times faster than with LATTICEEASY and 12 times faster than with CLUSTEREASY. I would estimate that it is $\mathcal{O}(10)$ faster than PyCOOL since that is the usual factor by which Python is slower than C++, and slightly faster than CUDAEASY since my code achieves better memory usage and coalescence. Of course, each code has different objectives–I designed this code to be as fast as possible just for the simple case of an uncoupled single scalar field, while past published codes are more versatile.

C.3 Code architecture

In order to better understand how the code was designed, we need to understand the basics of CUDA. In this section I will do a brief review of the CUDA programming model, and afterwards I will explain the 2D and 3D code architectures.

C.3.1 CUDA programming model

Memory size and speed are inversely correlated. As capacity increases, any two points in the memory get physically further apart and thus reading data becomes slower. This long standing problem in computing engineering was solved by making different **levels of memory**. In the case of a computer it is usually divided in 5 levels. From the fastest to the slowest we have the L1, L2 and L3 CPU caches, RAM and finally SSD/HDD. When programming for a CPU (e.g. in C++) and we load something–opening a file or defining a new variable–we do not decide where that is stored, the compiler will do it automatically. Memory management in a CPU us usually a black box.

In the same way, GPUs have multiple levels of memory—register, constant/texture, shared and global. Programming in CUDA is different from other languages because there is no black box, the programmer is in charge of the memory management[2].

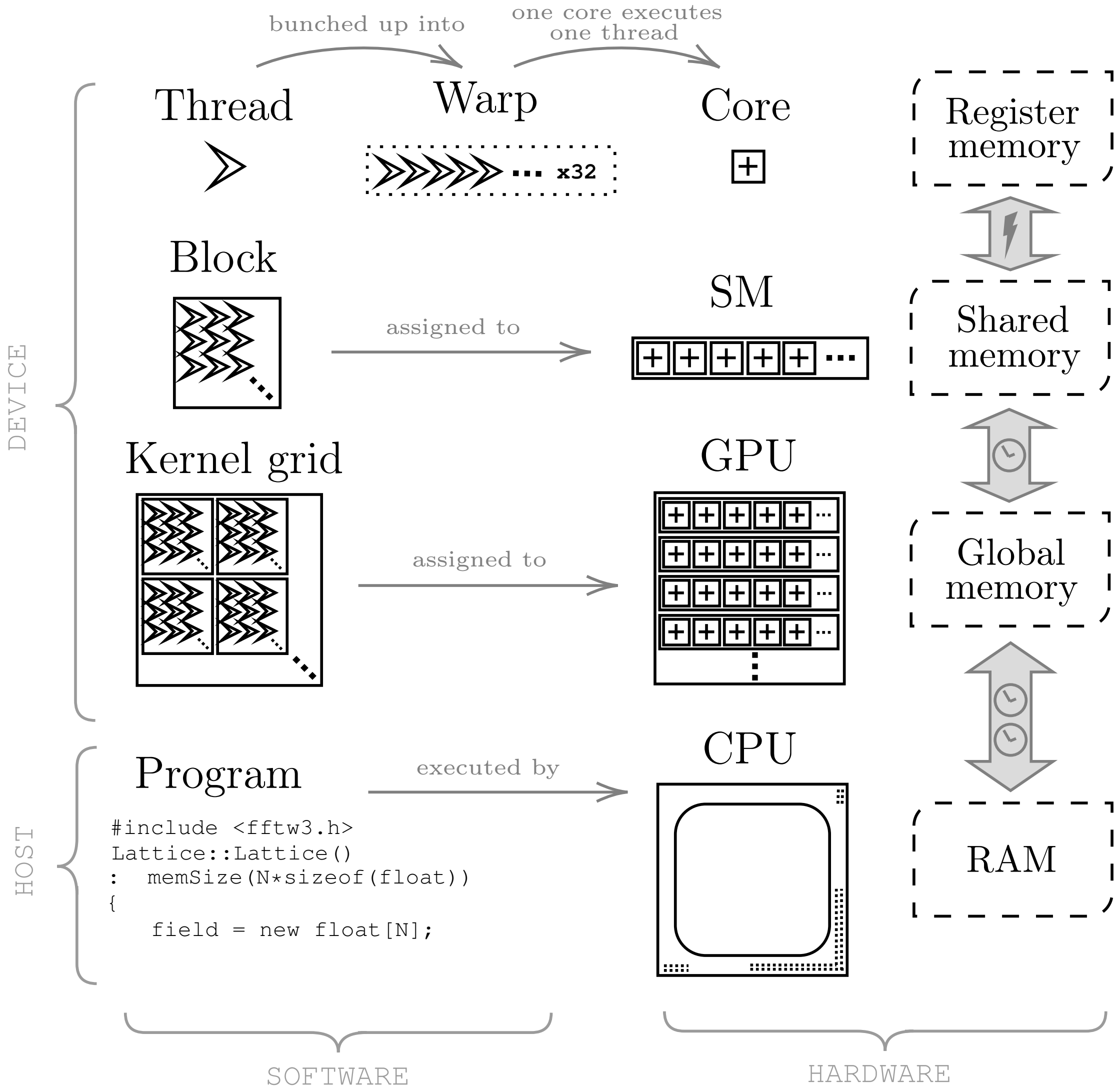

```
#include <fftw3.h>
Lattice::Lattice()
:  memSize(N*sizeof(float))
{
   field = new float[N];
```

A kernel is a function that will be executed in parallel in the GPU. For that purpose, it is subdivided in smaller units, called blocks and threads. Global memory can be accessed by all threads in a kernel, is the biggest ($\mathcal{O}$(GB)) but relatively slow. Shared memory is smaller ($\mathcal{O}$(MB)) but faster and can be accessed by all threads within a block. Register memory is the smallest ($\mathcal{O}$(KB)) and fastest, and is used by each individual thread. Each thread is executed by one core. GPUs have thousands of cores so kernels are usually called with thousands of threads. Threads from each

---

[2] We deal with this simple register/shared/global system when programming but the compiler still manages a lot on the back: virtual register memory may overflow from the hardware registers to the L1 cache, shared memory and L1 cache share the same hardware memory, global memory resides in both L2 cache and DRAM...

block are executed in groups of 32 called warps. Each thread within a warp must have the exact same instructions, only the data they act on is different.

When a warp wants to load data from global memory, bandwidth is maximized if each data point is physically next to one another. This is called a coalesced read. If that is not the case, it is called a strided read and the data will be read in serial, which is slower.

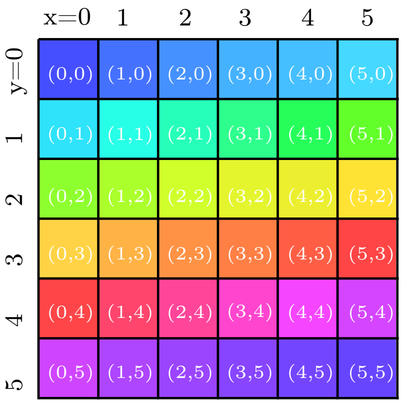

	x=0	1	2	3	4	5
y=0	(0,0)	(1,0)	(2,0)	(3,0)	(4,0)	(5,0)
1	(0,1)	(1,1)	(2,1)	(3,1)	(4,1)	(5,1)
2	(0,2)	(1,2)	(2,2)	(3,2)	(4,2)	(5,2)
3	(0,3)	(1,3)	(2,3)	(3,3)	(4,3)	(5,3)
4	(0,4)	(1,4)	(2,4)	(3,4)	(4,4)	(5,4)
5	(0,5)	(1,5)	(2,5)	(3,5)	(4,5)	(5,5)

Coalesced read of the $y = 0$ row

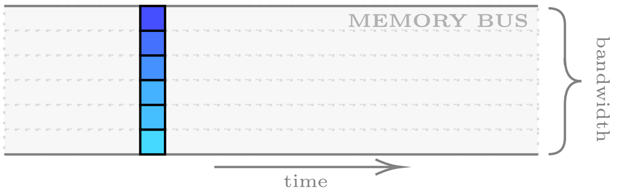

Strided read of the $x = 0$ column

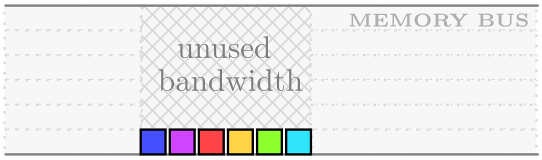

2D and 3D arrays are stored as 1D arrays in memory. Let me, for ease of visualization, use 6 instead of 32 in the diagrams. The above figure shows a 2D matrix, contiguous values in memory are represented by similar colors. We can see how reading any row (constant y) will coalesce while reading any column (constant x) will not.

Let us finish by giving a basic CUDA programming workflow. First, we identify which part of the code can be parallelized. Then, we divide it into equal chunks and assign each one to one block. Afterwards, we program the threads so that when bundled into warps memory reads and writes are coalesced. We avoid using `if-else` blocks that may cause threads within a warp to execute different instructions (i.e. to diverge). Once this structure is in place, we can more or less keep programming as we would usually do in C++ or other languages.

C.3.2 Periodic boundary conditions

A problem that all lattice simulations—parallelized or not—have to solve is how to efficiently implement periodic boundary conditions. When calculating the first neighbours of a field value at the border, one has to somehow loop around and take them from the opposite side of the matrix. There are three main ways to tackle this:

With conditionals. We can add a few `if()` conditions to every iteration over the field values to check whether we are in the border or not.

Programming each side separately. We can loop just over the inside of the matrix and program each side and corner separately.

Padding the matrix. We can make the matrix one elements wider on each side and update them after each iteration with the values on the opposite side.

I suppose that the creators of LATTICEEASY also tested this, since they chose the **fastest method**: programming each side separately. The consequences of choosing other methods are drastic. In my computer, for a small 2D simulation, the border method is 15% slower and the conditionals method is 60% slower.

C.3.3 2D tiling

In order to parallelize the field evolution it is standard to divide the 2D matrix into **tiles**. We can make the tile size a multiple of 32 and read/write in rows so that all data accesses within the tile are coalesced. However, for each tile there will be strips of neighbouring field values which are read but not updated, called **halos** [157].

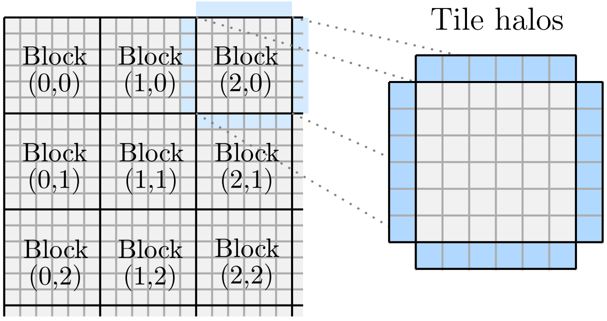

There are various ways to solve this problem:

Read the halos separately. If we were to do this, the reads for the top and bottom sides would be coalesced but not for the left nor right sides, so we can expect this to be slow.

Overlap the tiles. This is the solution CUDAEASY [160] opted for. Periodic boundary conditions are implemented with a border and tiles overlap by two elements. By doing this, the tile size is effectively two items smaller and thus outer threads only do memory loads and perform no calculations. Except for when the border is updated, all reads and writes are coalesced.

Use a mesh. The halos are stored in a separate array which I called mesh. This achieves 100% read/write coalescing and is more memory efficient than the other methods. This method has never been applied to cosmological lattice simulations, and although I came up with it by myself, it may have been used previously in other kinds of iterative stencil simulations.

When programming any lattice simulation we need to **write the evolved field values to a different matrix** than the one we are reading from. This is because we need to access contiguous field values to solve the differential equation, and if we write the evolved values on the same matrix we read we will not solve it correctly. With the mesh method, we do not need two copies of the lattice, just one lattice and two meshes. For a 64^2 tile size, this method uses 30% less memory than the others, which allows us to run bigger simulations on the same hardware. Another benefit of using a mesh is that it also solves the problem of implementing periodic boundary conditions.

As long as the tile side is a multiple of 32, the mesh can be indexed in many ways. In my case, I used a 3D array so that $x = [0, 32n)$ covers one side length, $y = [0, 4)$ indicates which side it corresponds to (0 for the left side, 1 for the right side etc.) and $z = [0, \text{n. of blocks})$ indicates which tile it corresponds to.

In a schematic way, this is what each block does each iteration:

1. The values of the field ϕ and its derivative $\dot{\phi}$ within the tile are loaded from `field` and `deriv` in global memory to shared memory.
2. The corresponding halos of ϕ are loaded from `mesh_in` in global memory to shared memory.
3. Staggered leapfrog is used to evolve the field and derivative values.
4. Evolved values are saved to `field`, `deriv` and `mesh_out`.
5. Pointers for `mesh_in` and `mesh_out` are swapped.

C.3.4 3D tiling

One could think that the 3D case would be tiled by many small cubes, but that would be a bad idea. In [157] it was proven that the most efficient way to parallelize iterative stencil simulations in 3D with CUDA was by tiling as usual on the xy plane and then sweeping through the z direction.

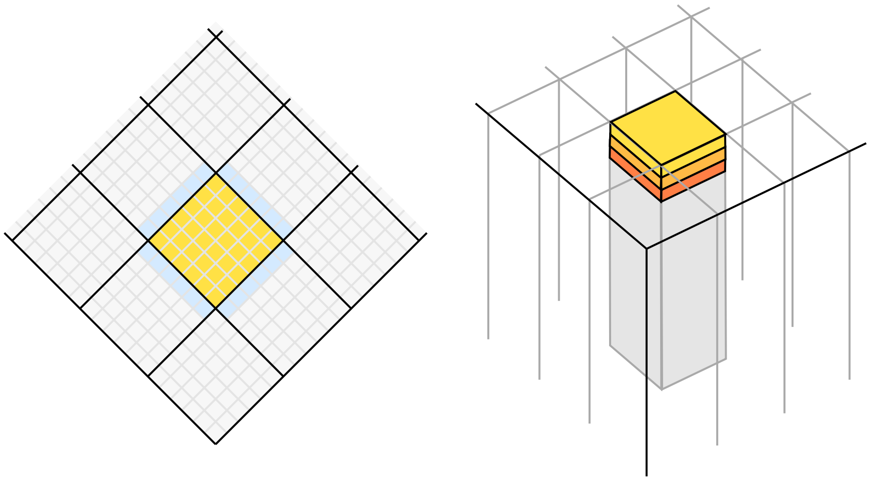

We can see an example of how that would work in the above figure. Each tile first loads three slices and solves the equation in the middle slice. Then it loads one new slice on the bottom, unloads the one on the top and the cycle keeps repeating until the whole z dimension of the matrix has been gone through.

For solving the halo problem, CUDAEASY opted for overlapping tiles as well in this case. I used the mesh method. In this case, the mesh is a 4D array (same as before + one more parameter for the z direction) and we need two more arrays for the top and bottom layers. For 32^2 tiles and a 960^3 lattice, this method uses 25% less memory, which is very important since after parallelizing the simulation size is mostly limited by the DRAM capacity.

One may also try to implement this sweeping scheme in the 2D case, as that would make the mesh smaller and thus more memory efficient. I found that, although that was the case, a naive implementation rendered the code 120% slower. Careful profiling of the global memory reads, as well as tuning the width/height of each individual read may turn the sweeping method into the most efficient 2D code architecture.

Bibliography

[1] A. Vilenkin, E.P.S. Shellard, *Cosmic Strings and Other Topological Defects.* Cambridge University Press (2000). [ISBN: 9780521654760]

[2] S. Weinberg, *Cosmology.* Oxford University Press (2008). [ISBN: 9780198526827]

[3] N. Beisert, *Quantum Field Theory.* ETH Zurich, Lecture Notes (2012). [URL]

[4] M. Bartelmann, *Lambda CDM and Early Universe Cosmology.* Summer School 2017: Joint Challenges for Cosmology and Colliders (2017). [URL]

[5] S. Dodelson, F. Schmidt, *Modern Cosmology.* Elsevier, 2nd Edition (2020). [ISBN: 9780128159484]

[6] D. Baumann, *Cosmology.* Cambridge University Press (2022). [ISBN: 9781108838078]

[7] A. Einstein, *The field equations of gravitation.* Königl. Preuss. Akad. Wiss. zu Berlin, **48**, 844 (1915). [Translation]

[8] G. Lemaître, *A Homogeneous Universe of Constant Mass and Growing Radius Accounting for the Radial Velocity of Extragalactic Nebulae.* G. Ann. Soc. Sci. Brux. A **47**, 49–59 (1927). [10.1007/s10714-013-1548-3]

[9] E. Hubble, *A Relation between Distance and Radial Velocity among Extra-Galactic Nebulae.* Proc. Natl. Acad. Sci. USA **15** (3) 168-173 (1929). [10.1073/pnas.15.3.168]

[10] J.H. Oort, *The force exerted by the stellar system in the direction perpendicular to the galactic plane and some related problems.* Bull. Astron. Inst. Netherlands, **6**, 249 (1932). [ads]

[11] F. Zwicky, *The red shift of extragalactic neubulae.* Helvetica Physica Acta (in German). **6**, 110–127 (1933). [ads]

[12] A.A. Penzias, R.W. Wilson, *A Measurement of Excess Antenna Temperature at 4080 Mc/s.* Astrophys. J. **142**, 419-421 (1964). [10.1086/148307]

[13] V.C. Rubin, W.K.J. Ford, *Rotation of the Andromeda Nebula from a Spectroscopic Survey of Emission Regions.* Astrophys. J. **159**, 379 (1970). [10.1086/150317]

[14] A.A. Starobinskiĭ, *Spectrum of relict gravitational radiation and the early state of the universe.* JETP Lett. **30**, 682 (1979). [ads]

[15] K. Sato, *First-order phase transition of a vacuum and the expansion of the Universe.* MNRAS **195** (3), 467-479 (1980). [10.1093/mnras/195.3.467]

[16] A.H. Guth, *Inflationary universe: A possible solution to the horizon and flatness problems.* Phys. Rev. D **23**, 347 (1981). [10.1103/PhysRevD.23.347]

[17] G.R. Blumenthal, S.M. Faber, J.R. Primack, M.J. Rees, *Formation of galaxies and large-scale structure with cold dark matter.* Nature, **311**, 517-525 (1984). [10.1038/311517a0]

[18] S.D.M. White, J.F. Navarro, A.E. Evrard, C.S. Frenk, *The baryon content of galaxy clusters: a challenge to cosmological orthodoxy.* Nature, **366** (6454), 429-433 (1993). [10.1038/366429a0]

[19] J.P. Ostriker, P.J. Steinhardt, *The observational case for a low-density Universe with a non-zero cosmological constant.* Nature, 377 (6550), 600-602 (1995). [10.1038/377600a0]

[20] A.G. Riess et al., *Observational Evidence from Supernovae for an Accelerating Universe and a Cosmological Constant.* Astron. J. **116**, 1009-1038 (1998). [astro-ph/9805201]

[21] S. Perlmutter et al., *Measurements of Omega and Lambda from 42 High-Redshift Supernovae.* Astrophys. J. **517**, 565-586 (1999). [astro-ph/9812133]

[22] G.F. Smoot et al., *Structure in the COBE differential microwave radiometer first-year maps.* Astrophys. J. Lett. **396** (1), 1-5 (1992). [ads]

[23] A.H. Jaffe, *Cosmology from Maxima-1, Boomerang and COBE/DMR CMB Observations.* Phys. Rev. Lett. **86** 3475-3479 (2001). [astro-ph/0007333]

[24] J.K. Yadav, J. S. Bagla, N. Khandai, *Fractal Dimension as a measure of the scale of Homogeneity.* Mon. Not. Roy. Astron. Soc. **405**, 2009 (2010). [1001.0617]

[25] M. Douspis, L. Salvati, N. Aghanim, *On the tension between Large Scale Structures and Cosmic Microwave Background.* EDSU2018 **037** (2018). [1901.05289]

[26] N. Aghanim, et al., *Planck 2018 results. VI. Cosmological parameters.* A&A **641**, A6 (2020). [1807.06209]

[27] E.D. Valentino et al., *In the Realm of the Hubble tension − a Review of Solutions.* Class. Quantum Grav. **38**, 153001 (2021). [2103.01183]

[28] N. Secrest et al., *A Test of the Cosmological Principle with Quasars.* Astrophys. J. Lett. **908** 51 (2020). [2009.14826]

[29] T.M. Siewert, M. Schmidt-Rubart, D. J. Schwarz, *The Cosmic Radio Dipole: Estimators and Frequency Dependence.* A&A 653, A9 (2021). [2010.08366]

[30] A.K. Singal, *Peculiar motion of Solar system from the Hubble diagram of supernovae Ia and its implications for cosmology.* MNRAS 515, 5969 (2022). [2106.11968]

[31] P.K. Aluri et al., *Is the Observable Universe Consistent with the Cosmological Principle?.* Clas. Quantum Grav. **40** (9), 094001 (2023). [2207.05765]

[32] T. Anton, T. Clifton, *Modelling the emergence of cosmic anisotropy from non-linear structures.* CQG (2023). [2302.05715]

[33] M. Milgrom, *A modification of the Newtonian dynamics as a possible alternative to the hidden mass hypothesis..* Astrophysical Journal, **270** 365-370 (1983). [10.1086/161130]

[34] G.F.R. Ellis, H. van Elst, *Cosmological models.* NATO Sci. Ser. C **541**, 1-116 (1999). [9812046v5]

[35] C. Alcock et al., *The MACHO Project: Microlensing Results from 5.7 Years of Large Magellanic Cloud Observations.* Astrophys. J. **542** 281 (2000). [10.1086/309512]

[36] R.H. Cyburt, *Primordial Nucleosynthesis for the New Cosmology: Determining Uncertainties and Examining Concordance.* Phys. Rev. D. **70**, 023505 (2004). [0401091]

[37] V. Springel et al., *Simulating the joint evolution of quasars, galaxies and their large-scale distribution.* Nature **435** 629-636 (2005). [0504097]

[38] D. Clowe et al., *A direct empirical proof of the existence of dark matter.* Astrophys. J. Lett. 648 109-113 (2006). [0608407v1]

[39] S.W. Allen, A.E. Evrard, A.B. Mantz, *Cosmological Parameters from Observations of Galaxy Clusters.* Annual Review of Astronomy and Astrophysics, **49**, 1, 409-470 (2011). [1103.4829]

[40] W. Heisenberg, *On the theory of ferromagnetism.* Zeit. Phys. 49 619-636 (orig. in German) (1928). [URL]

[41] Y. Nambu, G. Jona-Lasinio, *Dynamical Model of Elementary Particles Based on an Analogy with Superconductivity. II.* Phys. Rev. **124**, 246 (1961). [10.1103/PhysRev.124.246]

[42] J. Goldstone, *Field theories with Superconductor solutions.* Il Nuovo Cimento **19**, 154-164 (1961). [10.1007/BF02812722]

[43] S.L. Glashow, *Partial Symmetries of Weak Interactions.* Nucl. Phys. **22** 579-588 (1961). [10.1016/0029-5582(61)90469-2]

[44] G. A. Baker, *Certain General Order-Disorder Models in the Limit of Long-Range Interactions.* Phys. Rev. **126**, 2071 (1962). [10.1103/PhysRev.126.2071]

[45] D.A. Kirzhnits, A.D. Linde, *Macroscopic consequences of the Weinberg model.* Physics Letters B **42**, 4, 471-474 (1972). [10.1016/0370-2693(72)90109-8]

[46] G. 't Hooft, *Magnetic Monopoles in Unified Gauge Theories.* Nucl. Phys. B **79** 276-284 (1974). [10.1016/0550-3213(74)90486-6]

[47] N. Turok, *Global texture as the origin of cosmic structure.* Phys. Rev. Lett. **63**, 2625 (1989). [10.1103/PhysRevLett.63.2625]

[48] N. Turok, Y. Zhu, *Inflationary Textures.* PUPT-1674 (1996). [9612242v3]

[49] G. Dvali, A. Melfo, G. Senjanovic, *Nonrestoration of spontaneously broken P, CP and PQ at high temperature.* Phys.Rev. D54 7857-7866 (1996). [9601376v2]

[50] R. Durrer, *Cosmological Strucure Formation with Topological Defects.* 35th Rencontres de Moriond: Energy Densities in the Universe, 27-36 (2000). [0003363]

[51] T. Buchert, *Is there proof that backreaction of inhomogeneities is irrelevant in cosmology?.* Class. Quantum Grav. **32** 215021 (2015). [1505.07800v2]

[52] J.P. Ang, A. Prakash, *On the classification of topological defects and textures.* YITP-SB 18-30 (2018). [1810.12964]

[53] G. 't Hooft, *Symmetry Breaking through Bell-Jackiw Anomalies.* Phys. Rev. Lett. **37**, 8 (1976). [10.1103/PhysRevLett.37.8]

[54] R.D. Peccei, H.R. Quinn, *CP Conservation in the Presence of Pseudoparticles.* Phys. Rev. Lett. **38**, 1440 (1977). [10.1103/PhysRevLett.38.1440]

[55] S. Weinberg, *A New Light Boson?.* Phys. Rev. Lett. **40**, 223 (1978). [10.1103/PhysRevLett.40.223]

[56] F. Wilczek, *Problem of strong P and T invariance in the presence of instantons.* Phys. Rev. Lett. **40**, 279 (1978). [10.1103/PhysRevLett.40.279]

[57] J.E. Kim, *Weak-Interaction Singlet and Strong CP Invariance.* Phys. Rev. Lett. **43**, 103 (1979). [10.1103/PhysRevLett.43.103]

[58] M.A. Shifman, A.I. Vainshtein, V.I. Zakharov, *Can confinement ensure natural CP invariance of strong interactions?.* Nuclear Physics B, **166**, 3, 493-506 (1980). [10.1016/0550-3213(80)90209-6]

[59] A.R. Zhitnitskij, *On possible suppression of the axion-hadron interactions.* Yadernaya Fizika, 31(**2**), 497-504 (1980). [IAEA]

[60] M. Dine, W. Fischler, M. Srednicki, *A simple solution to the strong CP problem with a harmless axion.* Physics Letters B, **104** 3, 199-202 (1981). [10.1016/0370-2693(81)90590-6]

[61] J. Preskill, M.B. Wise, F. Wilczek, *Cosmology of the invisible axion.* Physics Letters B, **120**, 1-3, 127-132 (1983). [10.1016/0370-2693(83)90637-8]

[62] L. F. Abbott, P. Sikivie, *A cosmological bound on the invisible axion.* Physics Letters B, **120**, 1-3, 133-136 (1983). [10.1016/0370-2693(83)90638-X]

[63] W. Dine, W. Fischler, *The not-so-harmless axion.* Physics Letters B, **120**, 1-3, 137-141 (1983). [10.1016/0370-2693(83)90639-1]

[64] P. Sikivie, *Experimental Tests of the "Invisible" Axion.* Phys. Rev. Lett. **51**, 1415 (1983). [10.1103/PhysRevLett.51.1415]

[65] K. Freese, J.A. Frieman, A.V. Olinto, *Natural inflation with pseudo Nambu-Goldstone bosons.* Phys. Rev. Lett. **65**, 3233 (1990). [10.1103/PhysRevLett.65.3233]

[66] G. G. Raffelt, *Astrophysical methods to constrain axions and other novel particle phenomena.* Physics Reports, **198**, 1-2, 1-113 (1990). [10.1016/0370-1573(90)90054-6]

[67] A. Arvanitaki, *String Axiverse.* Phys. Rev. D **81**, 123530 (2010). [0905.4720]

[68] P.W. Graham, D.E. Kaplan, S. Rajendran, *Cosmological Relaxation of the Electroweak Scale.* Phys. Rev. Lett. 115, 221801 (2015). [1504.07551]

[69] M.C.D. Marsh et al., *A New Bound on Axion-Like Particles.* JCAP **12**, 036 (2017). [1703.07354]

[70] N. Bar, K. Blum, G. D'Amico, *Is there a supernova bound on axions?.* Phys. Rev. D **101**, 123025 (2020). [1907.05020]

[71] K. Choi, S.H. Im, C.S. Shin, *Recent Progress in the Physics of Axions and Axion-Like Particles.* Annual Review of Nuclear and Particle Science, **71**, 225-252 (2021). [2012.05029]

[72] C. O'Hare, *cajohare/axionlimits: Axionlimits.* (2023) [cajohare.github.io]

[73] CAST Collaboration, *First results from the CERN Axion Solar Telescope.* Phys. Rev. Lett. **94** 121301 (2005). [hep-ex/0411033]

[74] E. Armengaud et al., *Physics potential of the International Axion Observatory (IAXO).* JCAP **06** 047 (2019). [1904.09155]

[75] Y.B. Zeldovich, I.Y. Kobzarev, L.B. Okun, *Cosmological Consequences of the Spontaneous Breakdown of Discrete Symmetry.* Zh. Eksp. Teor. Fiz. **67** 3-11 (1974). [ads]

[76] T.W.B. Kibble, *Topology of cosmic domains and strings.* Journal of Physics A: Mathematical and General, **9**, 8, 1387-1398 (1976). [10.1088/0305-4470/9/8/029]

[77] T.W.B. Kibble, *Some implications of a cosmological phase transition..* Physics Reports, **67**, 1, 183-199 (1980). [10.1016/0370-1573(80)90091-5]

[78] G. Lazarides, Q. Shafi, *Axion models with no domain wall problem.* Physics Letters B, **115**, 1, 21-25 (1982). [10.1016/0370-2693(82)90506-8]

[79] A. Vilenkin, A.E. Everett, *Cosmic Strings and Domain Walls in Models with Goldstone and Pseudo-Goldstone Bosons.* Phys. Rev. Lett. **48**, 1867 (1982). [10.1103/PhysRevLett.48.1867]

[80] J. Ipser, P. Sikivie, *Gravitationally repulsive domain wall.* Phys. Rev. D **30**, 712 (1984). [10.1103/PhysRevD.30.712]

[81] A. Vilenkin, *Gravitational field of vacuum domain walls.* Physics Letters B, **133**, 3-4, 177-179 (1983). [10.1016/0370-2693(83)90554-3]

[82] A.K. Mohanty, F.W. Stecker, *Matter-antimatter domains: A possible solution to the CP domain wall problem in the early universe.* Physics Letters B, **143**, 4-6, 351-356 (1984). [10.1016/0370-2693(84)91481-3]

[83] C.T. Hill, D.N. Schramm, J.N. Fry, *Cosmological Structure Formation from Soft Topological Defects.* Comments on Nuclear and Particle Physics, **19**, 1, 25-39 (1989). [iNSPIRE]

[84] W.H. Press, B.S. Ryden, D.N. Spergel, *Dynamical Evolution of Domain Walls in an Expanding Universe.* Astrophysical Journal v.347, p.590 (1989). [10.1086/168151]

[85] W.H. Press, B.S. Ryden, D.N. Spergel, *The evolution of networks of domain walls and cosmic strings.* Astrophysical Journal, Part 1, **357**, 293-300. (1990). [ads]

[86] M. Nagasawa, J. Yokoyama, *Phase transitions triggered by quantum fluctuations in the inflationary universe.* Nuclear Physics B, **370**, 2, 472-490 (1992). [10.1016/0550-3213(92)90294-L]

[87] H. Kubotani, *The Domain Wall Network of Explicitly Broken O(N) Model.* Progress of Theoretical Physics, **87**, 2, 387-400 (1992). [10.1143/ptp/87.2.387]

[88] Z. Lalak, S. Thomas, *Domain Wall Formation In The Post-Inflationary Universe.* Phys. Lett. B **306** 10-18 (1993). [hep-ph/9303250]

[89] Z. Lalak, S. Lola, B.A. Ovrut, G.G. Ross, *Large scale structure from biased non-equilibrium phase transitions - percolation theory picture.* Nuclear Physics B, **434**, 3, 675-696 (1995). [10.1016/0550-3213(94)00557-U]

[90] D. Coulson, Z. Lalak, B. Ovrut, *Non-Equilibrium Phase Transitions and Domain Walls.* PASCOS/HOPKINS (1995). [hep-ph/9508226]

[91] Z. Lalak, B. Ovrut, S. Thomas, *Large-scale structure as a critical phenomenon.* Phys. Rev. D **51**, 5456 (1995). [10.1103/PhysRevD.51.5456]

[92] G. Dvali, G. Senjanovic, *Is there a domain wall problem?.* Phys. Rev. Lett. **74** 5178-5181 (1995). [hep-ph/9501387]

[93] D. Coulson, Z. Lalak, B. Ovrut, *Biased domain walls.* Phys. Rev. D **53**, 4237 (1996). [10.1103/PhysRevD.53.4237]

[94] C.J.A.P. Martins, E.P.S. Shellard, *String Evolution with Friction.* Phys. Rev. D, **53**, 575-579 (1996). [hep-ph/9507335]

[95] C.J.A.P. Martins, E.P.S. Shellard, *Quantitative String Evolution.* Phys. Rev. D, **54**, 2535-2556 (1996). [hep-ph/9602271]

[96] S.E. Larsson, S. Sarkar, P.L. White, *Evading the cosmological domain wall problem.* Phys. Rev. D, 55, 5129-5135 (1997). [hep-ph/9608319]

[97] P.P. Avelino, C.J.A.P. Martins, *Topological defects: fossils of an anisotropic era?.* Phys. Rev. D, **62**, 103510 (2000). [astro-ph/0003231]

[98] T. Garagounis, M. Hindmarsh, *Scaling in Numerical Simulations of Domain Walls.* Phys. Rev. D, **68**, 103506 (2003). [hep-ph/0212359]

[99] J.C.R.E. Oliveira, C.J.A.P. Martins, P.P. Avelino, *The Cosmological Evolution of Domain Wall Networks.* Phys. Rev. D, **71**, 083509 (2005). [hep-ph/0410356]

[100] P.P. Avelino, J.C.R.E. Oliveira, C.J.A.P. Martins, *Understanding Domain Wall Network Evolution.* Phys. Lett. B, **610**, 1-8 (2005). [hep-th/0503226]

[101] P.P. Avelino, C.J.A.P. Martins, J.C.R.E. Oliveira, *One-scale Model for Domain Wall Network Evolution.* Phys. Rev. D, **72**, 083506 (2005). [hep-ph/0507272]

[102] D. Stojkovic, K. Freese, G.D. Starkman, *Holes in the walls: primordial black holes as a solution to the cosmological domain wall problem.* Phys. Rev. D **72**, 045012 (2005). [hep-ph/0505026]

[103] A.M.M. Leite, C.J.A.P. Martins, *Scaling Properties of Domain Wall Networks.* Phys. Rev. D **84**, 103523 (2011). [abs/1110.3486]

[104] T. Moroi, K. Nakayama, *Domain Walls and Gravitational Waves after Thermal Inflation.* Phys. Lett. B, **703**, 160-166 (2011). [1105.6216v1]

[105] A.M.M. Leite, C.J.A.P. Martins, E.P.S. Shellard, *Accurate Calibration of the Velocity-dependent One-scale Model for Domain Walls.* Phys. Lett. B **718**, 740-744 (2013). [1206.6043]

[106] T. Hiramatsu, M. Kawasaki, K. Saikawa, T. Sekiguchi, *Axion cosmology with long-lived domain walls.* JCAP, **01**, 001 (2013). [1207.3166]

[107] J.R.C.C.C. Correia, I.S.C.R. Leite, C.J.A.P. Martins, *Effects of biases in domain wall network evolution..* Phys. Rev. D, **90**, 023521 (2014). [1407.3905]

[108] C.J.A.P. Martins, I.Y. Rybak, A. Avgoustidis, E.P.S. Shellard, *Extending the velocity-dependent one-scale model for domain walls.* Phys. Rev. D, **93**, 043534 (2016). [1602.01322]

[109] J.R.C.C.C. Correia, I.S.C.R. Leite, C.J.A.P. Martins, *Effects of biases in domain wall network evolution. II. Quantitative analysis.* Phys. Rev. D, 97, 083521 (2018). [1804.10761]

[110] R. Sato, F. Takahashi, M. Yamada, *Unified Origin of Axion and Monopole Dark Matter, and Solution to the Domain-wall Problem.* Phys. Rev. D **98**, 043535 (2018). [1805.10533]

[111] M. Reig, *On the high-scale instanton interference effect: axion models without domain wall problem.* JHEP, **08** 167 (2019). [1901.00203]

[112] M. Ibe, S. Kobayashi, M. Suzuki, T.T. Yanagida, *A Dynamical Solution to the Axion Domain Wall Problem.* Phys. Rev. D, **101**, 035029 (2020). [1909.01604]

[113] D. Gonzalez, N. Kitajima, F. Takahashi, W. Yin, *Stability of domain wall network with initial inflationary fluctuations, and its implications for cosmic birefringence.* Phys. Lett. B 843, 137990 (2023). [2211.06849]

[114] T. Krajewski, J.H. Kwapisz, Z. Lalak, M. Lewicki, *Stability of domain walls in models with asymmetric potentials.* Phys. Rev. D, **104**, 12, 123522 (2021). [2103.03225]

[115] N. Kitajima, J. Lee, F. Takahashi, W. Yin, *In preparation.*

[116] R.K. Sachs, A.M. Wolfe, *Perturbations of a Cosmological Model and Angular Variations of the Microwave Background.* Astrophysical Journal, **147**, 73 (1967). [10.1086/148982]

[117] S.M. Carroll, G.B. Field, R. Jackiw, *Limits on a Lorentz- and parity-violating modification of electrodynamics.* Phys. Rev. D **41**, 1231 (1990). [10.1103/PhysRevD.41.1231]

[118] S.M. Carroll, G.B. Field, *Einstein equivalence principle and the polarization of radio galaxies.* Phys. Rev. D **43**, 3789 (1991). [10.1103/PhysRevD.43.3789]

[119] D. Harari, P. Sikivie, *Effects of a Nambu-Goldstone boson on the polarization of radio galaxies and the cosmic microwave background.* Physics Letters B, **289**, 1-2, 67-72 (1992). [10.1016/0370-2693(92)91363-E]

[120] M. Kamionkowski, A. Kosowsky, A. Stebbins, *Statistics of Cosmic Microwave Background Polarization.* Phys. Rev. D **55** 7368-7388 (1997). [astro-ph/9611125]

[121] W. Hu, M. White, *A CMB Polarization Primer.* New Astron. **2** 323 (1997). [astro-ph/9706147]

[122] E. Bertschinger, *Cosmological Perturbation Theory and Structure Formation.* Cosmology 2000, **1**, 1-25 (2001). [astro-ph/0101009v1]

[123] W. Hu, S. Dodelson, *Cosmic Microwave Background Anisotropies.* Ann. Rev. Astron. Astrophys. **40**, 171-216 (2002). [astro-ph/0110414]

[124] B. Feng et al., *Searching for CPT Violation with Cosmic Microwave Background Data from WMAP and BOOMERANG.* Phys. Rev. Lett. **96** 221302 (2006). [astro-ph/0601095]

[125] F. Bernardeau, C. Pitrou, J-P. Uzan, *CMB spectra and bispectra calculations: making the flat-sky approximation rigorous.* JCAP **02** 015 (2011). [1012.2652]

[126] Z. Kermish et al., *The POLARBEAR Experiment.* Proc. SPIE **8452** (2012). [1210.7768]

[127] J.E. Austermann et al., *SPTpol: an instrument for CMB polarization measurements with the South Pole Telescope.* Proc. SPIE **8452** (2012). [1210.4970]

[128] The BICEP2 Collaboration, *BICEP2 II: Experiment and Three-Year Data Set.* ApJ **792**, 62 (2014). [1403.4302]

[129] M. Bucher, *Physics of the cosmic microwave background anisotropy.* Int. J. Mod. Phys. D **24** 02 (2015). [1501.04288]

[130] The CMB-S4 Collaboration, *CMB-S4 Science Book, First Edition.* (2016) [1610.02743]

[131] M.C. Guzzetti, N. Bartolo, M. Liguori, S. Matarrese, *Gravitational waves from inflation.* Riv. Nuovo Cim. **39** 9, 399-495 (2016). [1605.01615]

[132] The Simons Observatory Collaboration, *The Simons Observatory: Science goals and forecasts.* JCAP **1902** 056 (2019). [1808.07445]

[133] The NASA PICO Collaboration, *PICO: Probe of Inflation and Cosmic Origins.* (2019) [1902.10541]

[134] H. Sugai et al., *Updated design of the CMB polarization experiment satellite LiteBIRD.* Journal of Low Temperature Physics **199**, 1107 (2020). [2001.01724]

[135] H. Kurki-Suonio, *Cosmological Perturbation Theory I.* Lecture notes, University of Helsinki (2022). [URL]

[136] BICEP/Keck Collaboration, *BICEP / Keck XVII: Line of Sight Distortion Analysis: Estimates of Gravitational Lensing, Anisotropic Cosmic Birefringence, Patchy Reionization, and Systematic Errors.* ApJ **949** 43 (2023). [2210.08038]

[137] G. Goetz, D. Nötzold, *Characteristic Microwave-Background Distortions from Collapsing Spherical Domain Walls.* Phys. Rev. Lett. **65**, 3458 (1990). [10.1103/PhysRevLett.65.3458]

[138] W. Hu, D.N. Spergel, M. White, *Distinguishing Causal Seeds from Inflation.* Phys. Rev. D, **55**, 3288-3302 (1997). [astro-ph/9605193]

[139] N. Turok, U. Pen, U. Seljak, *The Scalar, Vector and Tensor Contributions to CMB anisotropies from Cosmic Defects.* Phys. Rev. D, **58**, 023506 (1998). [astro-ph/9706250]

[140] L. Sousa, P.P. Avelino, *Cosmic microwave background anisotropies generated by domain wall networks.* Phys. Rev. D **92**, 083520 (2015). [1507.01064]

[141] A. Lazanu, C.J.A.P. Martins, E.P.S. Shellard, *Contribution of domain wall networks to the CMB power spectrum.* Phys. Lett. B, **747**, 426-432 (2015). [1505.03673]

[142] M.A. Fedderke, P.W. Graham, S. Rajendran, *Axion Dark Matter Detection with CMB Polarization.* Phys. Rev. D **100**, 015040 (2019). [1903.02666]

[143] L. Pogosian, M. Shimon, M. Mewes, B. Keating, *Future CMB constraints on cosmic birefringence and implications for fundamental physics.* Phys. Rev. D **100**, 023507 (2019). [1904.07855]

[144] P. Agrawal, A. Hook, J. Huang, *A CMB Millikan Experiment with Cosmic Axiverse Strings.* JHEP **07** 138 (2020). [1912.02823]

[145] T. Fujita, Y. Minami, K. Murai, H. Nakatsuka, *Probing Axion-like Particles via CMB Polarization.* Phys. Rev. D **103**, 063508 (2021). [2008.02473]

[146] T. Fujita, K. Murai, H. Nakatsuka, S. Tsujikawa, *Detection of isotropic cosmic birefringence and its implications for axion-like particles including dark energy.* Phys. Rev. D **103**, 043509 (2021). [2011.11894]

[147] F. Takahashi, W. Yin, *Kilobyte Cosmic Birefringence from ALP Domain Walls.* JCAP **04** 007 (2021). [2012.11576]

[148] S. Nakagawa, F. Takahashi, M. Yamada, *Cosmic Birefringence Triggered by Dark Matter Domination.* Phys. Rev. Lett. **127**, 181103 (2021). [2103.08153]

[149] M. Jain, A.J. Long, M.A. Amin, *CMB birefringence from ultra-light axion string networks.* JCAP **05** 055 (2021). [2103.10962]

[150] G. Choi, W. Lin, L. Visinelli, T.T. Yanagida, *Cosmic Birefringence and Electroweak Axion Dark Energy.* Phys. Rev. D **104** 10, L101302 (2021). [2106.12602]

[151] W.W. Yin, L. Dai, S. Ferraro, *Probing cosmic strings by reconstructing polarization rotation of the cosmic microwave background.* JCAP 06 033 (2022). [2111.12741]

[152] P. Diego-Palazuelos et al., *Cosmic Birefringence from Planck Data Release 4.* Phys.Rev.Lett. **128** 9, 091302 (2022). [2201.07682]

[153] S. Gasparotto, I. Obata, *Cosmic Birefringence from Monodromic Axion Dark Energy.* JCAP **08** 025 (2022). [2203.09409]

[154] M. Jain, R. Hagimoto, A.J. Long, M.A. Amin, *Searching for axion-like particles through CMB birefringence from string-wall networks.* JCAP **10** 090 (2022). [2208.08391]

[155] K. Murai, F. Naokawa, T. Namikawa, E. Komatsu, *Isotropic cosmic birefringence from early dark energy.* Phys.Rev.D **107** 4 (2023). [2209.07804]

[156] W.W. Yin, L. Dai, S. Ferraro, *Testing charge quantization with axion string-induced cosmic birefringence.* (2023) [2305.02318]

[157] M. Patra, M. Karttunen, *Stencils with isotropic discretization error for differential operators.* Numerical Methods for Partial Differential Equations, **22** 4, 936-953 (2005). [10.1002/num.20129]

[158] G. Felder, I. Tkachev, *LATTICEEASY: A Program for Lattice Simulations of Scalar Fields in an Expanding Universe.* Comput. Phys. Commun. **178**, 929-932 (2008). [0011159]

[159] P. Micikevicius, *3D finite difference computation on GPUs using CUDA.* GPGPU-2 **8** (2009). [e-print]

[160] J. Sainio, *CUDAEASY - a GPU Accelerated Cosmological Lattice Program.* Comput. Phys. Commun. **181**, 906-912 (2010). [0911.5692]

[161] J. Sainio, *PyCOOL - a Cosmological Object-Oriented Lattice code written in Python.* JCAP **04** 038 (2012). [1201.5029]

[162] J.R.C.C.C. Correia, C.J.A.P. Martins, *General purpose graphics-processing-unit implementation of cosmological domain wall network evolution.* Phys. Rev. E **96** 043310 (2017). [1710.10420]

[163] D.G. Figueroa, A. Florio, F. Torrenti, W. Valkenburg, *CosmoLattice.* Comput. Phys. Commun. 283 108586 (2023). [2102.01031]

[164] OpenCL, *Reference Pages.* 2.1 (2017). [URL]

[165] NVIDIA, *CUDA C++ Programming Guide.* v12.1 (2023). [URL]

[166] Open MPI, *Documentation.* v4.1.5 (2023). [URL]